AGH University of Kraków

Field of science of engineering and technology

Scientific discipline of automation, electronics, electrical engineering and space technology

Ph.D. Thesis

Static and dynamic characterization of magnetic tunnel junctions with perpendicular anisotropy

Author:
Piotr Rzeszut

Supervisor:
Prof. Witold Skowroński, D.Sc.

AGH University of Kraków
Department of Computer Science, Electronics and Telecommunications
Institute of Electronics
Kraków 2023

Akademia Górniczo-Hutnicza im. Stanisława Staszica w Krakowie

Dziedzina nauk inżynieryjno-technicznych

Dyscyplina naukowa:

automatyka, elektronika, elektrotechnika i technologie kosmiczne

Rozprawa doktorska

Statyczna i dynamiczna charakteryzacja magnetycznych złącz tunelowych z anizotropią prostopadłą

Autor:

Piotr Rzeszut

Promotor:

dr hab. inz. Witold Skowroński, prof. AGH

Akademia Górniczo-Hutnicza im. Stanisława Staszica w Krakowie

Wydział informatyki, Elektroniki i Telekomunikacji

Instytut Elektroniki

Kraków 2023

Static and dynamic characterization of magnetic tunnel junctions with perpendicular anisotropy

Piotr Rzeszut

AGH University of Kraków

Copyright © 2023 Piotr Rzeszut

AGH UNIVERSITY OF KRAKÓW
SCIENTIFIC DISCIPLINE OF AUTOMATION, ELECTRONICS, ELECTRICAL ENGINEERING AND SPACE TECHNOLOGY

Declaration

I hereby declare that the work in this Thesis is my own original work, except where indicated in the text.

June 2023

STATIC AND DYNAMIC CHARACTERIZATION OF MAGNETIC TUNNEL JUNCTIONS WITH PERPENDICULAR ANISOTROPY

PIOTR RZESZUT

Abstract

The goal of this PhD thesis is research on magnetic tunnel junctions with perpendicular and mixed anisotropy in both static (direct current) and dynamic (radio-frequency regime). The research was targeted to provide practical applications, ready for industrial manufacturing. Introduced solutions include multi-state magnetic random access memory cell and a design of artificial neural network based on serially connected magnetic tunnel junctions.

The work beings with basic description of fundamental effects contributing to magnetic tunnel junction behaviour. A review on artificial neural networks is also included. In the next part a paper on design and operation of multi-bit magnetic RAM cell is presented. Then a research paper describing the use of such multi-state cells in an artificial neural network is introduced, covering also results of simulation of such computing solution. Last but not least the most recent research results on synchronization of electrically connected magnetic tunnel junction oscillators (both taking into account mutual synchronization as well as when external signal is introduced) are discussed. Such synchronization effects might also find use in different types of neural networks.

Before the conclusion of the work all the measurement and fabrication techniques are described, being the most important and time-consuming part of the research.

STATYCZNA I DYNAMICZNA CHARAKTERYZACJA

MAGNETYCZNYCH ZŁĄCZ TUNELOWYCH
Z ANIZOTROPIĄ PROSTOPADŁĄ

PIOTR RZESZUT

Streszczenie

Celem niniejszej rozprawy doktorskiej było badanie magnetycznych złącz tunelowych z anizotropią prostopadłą oraz mieszaną w zakresie statycznym (prądu stałego) oraz dynamicznym (zakresy wielkich częstotliwości). Badania skoncentrowane były wokół praktycznego zastosowania ich wyników w rozwiązaniach praktycznych, możliwych do wytwarzania na skalę przemysłową. Zaproponowano m.in. innowacyjną wielostanową komórkę magnetycznej pamięci RAM oraz projekt sztucznej sieci neuronowej opartej o szeregowo połączone złącza tunelowe.

Pracę rozpoczyna opis wybranych podstaw zjawisk odpowiedzialnych za działanie magnetycznych złącz tunelowych, oraz przegląd najważniejszych zagadnień związanych ze sztucznymi sieciami neuronowymi. Następnie zaprezentowana jest publikacja opisująca konstrukcję i charakterystyki wielostanowej komórki magnetycznej pamięci RAM. W kolejnej części przestawiona jest praca opisująca wykorzystanie wielostanowych komórek w konstrukcji sztucznej sieci neuronowej oraz rezultaty symulacji tak skonstruowanego rozwiązania. Najnowsze prezentowane rezultaty dotyczą zjawisk synchronizacji elektrycznie połączonych oscylatorów opartych o magnetyczne złącza tunelowe, badano zarówno synchronizacje wzajemne jak i do wygenerowanych sztucznie sygnałów zewnętrznych. Synchronizacje takie mogą również znaleźć zastosowanie w konstrukcji sieci neuronowych.

Przed podsumowaniem pracy przedstawione zostały najważniejsze techniki fabrykacji złącz oraz prowadzenia pomiarów, które ze względu na stopień skomplikowania stanowiły istotną i czasochłonną część tych badań.

First and foremost, I would like to express my sincere gratitude to my supervisor Prof. Witold Skowroński for his patient guidance throughout my Ph.D. course and invaluable advices. I am also deeply grateful to Prof. Tomasz Stobiecki for sharing his knowledge and experience.

Special thanks are extended to my colleagues: PhD Sławomir Ziętek, MSc Jakub Mojsiejuk, PhD Jakub Sorocki, PhD Jakub Chęciński, PhD Antoni Żywczak, PhD Ireneusz Brzozowski, PhD Monika Cecot, MSc Krzysztof Grochot and PhD Stanisław Łazarski for their help and teamwork.

I would like to thank PhD Jerzy Wrona from Singulus Technologies AG for MTJ multilayer deposition for memory applications. I would like to express gratitude to partners from AIST Tsukuba: Tsunegi Sumito, Kubota Hitoshi, Yuasa Shinji for their help during experiments on synchronization of MTJ-based oscillators and for providing multilayer structures for the experiments. The nano-fabrication processes were performed at Academic Centre for Materials and Nanotechnology (ACMiN) of AGH University of Science and Technology.

Various parts of this work were supported by: Polish Ministry of Science and Higher Education "Diamond Grant" program grant No. 0048/DIA/2017/46, Polish National Center for Research and Development grant No. LIDER/467/L-6/14/NCBR/2015 and National Science Centre grant No. 2016/23/B/ST3/01430.

I dedicate this work to all the people, who helped me to find the right path in my life, from the very beginning up to the moment.

Piotr Rzeszut

Contents

List of papers 10

1. Introduction 11

1.1. Significance of the research 11

1.2. Scientific goals and organization of the Thesis 12

2. Magnetic Tunnel Junctions and its static and dynamic behaviour 14

2.1. Magnetic tunnel junction 15

2.2. Spin Transfer Torque and Current Induced Magnetization Switching 17

2.3. Technologies competetive to MRAM 19

2.4. Magnetization dynamics of MTJs 20

3. Multistate MRAM memory cells 22

3.1. Multi-bit MRAM storage cells utilizing serially connected perpendicular magnetic tunnel junctions. 24

4. Artificial Neural Networks 29

4.1. Comparision of Artificial Neural Networks Architectures 29

4.2. ANN Learning 31

4.3. Voltage feed-forward ANN 32

5. Neuromorphic computing architecture based on MTJs 33

5.1. Multi-state MRAM cells for hardware neuromorphic computing. 35

6. Synchronization of STO oscillations 46

6.1. Towards mutual synchronization of serially connected Spin Torque Oscillators based on magnetic tunnel junctions 48

7. Measurement and fabrication techniques 55

7.1. Fabrication 55

7.2. Measurement setups 60

7.2.1. DC measurement setup 60

7.2.2. RF measurement setup 61

7.3. Software 64
7.3.1. LabVIEW software 64
7.3.2. Python software 65
8. Summary 67
Bibliography 78
Author's Achievements 79

List of papers

This Thesis is based on and incorporates the following publications:

Chapter 3:
- P. Rzeszut, W. Skowroński, S. Ziętek, J. Wrona, and T. Stobiecki, "Multi-bit MRAM storage cells utilizing serially connected perpendicular magnetic tunnel junctions," *Journal of Applied Physics*, vol. 125, no. 22, p. 223907, 2019.

Chapter 5:
- P. Rzeszut, J. Chęciński, I. Brzozowski, S. Ziętek, W. Skowroński, and T. Stobiecki, "Multi-state MRAM cells for hardware neuromorphic computing," *Scientific Reports*, vol. 12, no. 1, pp. 1–11, 2022.

Chapter 6:
- P. Rzeszut, J. Mojsiejuk, W. Skowroński, S. Tsunegi, H. Kubota, and S. Yuasa, "Towards mutual synchronization of serially connected Spin Torque Oscillators based on magnetic tunnel junctions," *arXiv preprint arXiv:2306.11608*, 2023.

1. Introduction

1.1. Significance of the research

Spin electronics is a very significant topic in the realm of modern technology. Spintronics emerged as a promising alternative to conventional charge-based electronics, which limitations might be overcome by the use of spin of the electrons for data storage, processing and much more. This might potentially bring a solution to greatly decrease energy consumption[4, 5] of various electronic devices, mitigate issues with heat dissipation and much more. For the reason spin-based solutions are widely investigated as an alternative for conventional CMOS circuits[6].

Spintronics rely on some well-established findings, such as effects discovered as early as 1988[7, 8] but also takes advantage of novel physical phenomena, such as spin transfer and spin orbit torques, two-dimensional materials and many more. Spintronics already made its way into commercial devices, where it can be seen as a mature and well-known technology in some applications. For example spintronic devices (nowadays mainly magnetic tunnel junctions) are widely used in readout heads of magnetic hard drives (HDD), where sensitivity and high bandwidth of the spin-devices allowed for increase of data density and operation speeds in such memories. Other important application of spin electronics is magnetic random access memories (MRAM), where magnetic tunnel junctions (MTJ) allows for a non-volatile storage of data in a form of solid state memory, where speeds of operation reach order of magnitude of conventional random access memories (RAM) while providing data retention similar to HDDs. What is more, MRAM devices are immune to all types of radiation, what allows them to be used as a storage for aircraft, spacecraft and other machines, that must work reliably in harsh conditions.

Characteristics of MTJs makes them also a very good fit for various schemes of neuromorphic computing[9, 2], where traditional digital circuits prove to be energy-inefficient[10]. By using spintronic devices calculations might be performed by means of analogue signals, where MTJ-based memristors allow for flexible current flow control. On the other hand a stochastic nature of some processes related to magnetization might mimic response of the real neuron to pulse-like signals[11] (spiking neural networks), and also oscillations that might be both generated and selectively detected by special types of MTJ can be used to encode and process various types of data. Finally, MTJs of low thermal stability may be used in a probabilistic-bit circuits that already

proved to be useful in solving some optimization problems such as integer factorization[12].

Considering how well-known spintronics devices are, some may think, that there is not much room for a novel research in the topic. However this is not true, as there is much to discover and try in this field, considering new applications, device types as well as better understanding of all the phenomena having impact on electrical characteristics and fabrication challenges. Some of these aspects were evaluated by the author of the thesis and the work is believed to extend the knowledge in the field as well as lead foundations to completely new applications of spin electronics. Here the fact, that MTJs are well-known in the business gives opportunities to quickly transfer the scientific knowledge to industry, as integration processes with existing technologies (mostly CMOS) are established and ready to be manufactured[13, 14].

Finally, considering all the opportunities that are provided by spintronic devices, the research topic is significant, as it may lead to a revolution in information storage and processing technologies. In the work both characteristics of MTJs as well as their application in practical circuits are examined and presented. Proposed applications include data storage as well as support for information processing by means of artificial neural networks.

1.2. Scientific goals and organization of the Thesis

The goal of the thesis was to examine both static and dynamic characteristics of magnetic tunnel junctions as well as propose practical application of such devices. It is very important to find industrial applications for the results of the research as this is as valuable as the knowledge itself. What is more such applications and possible future cooperation with commercial companies usually lead to interesting opportunities and boost of the future research.

The Thesis is organized into 8 chapters followed by bibliography and list of important author's achievements. Three of the chapters include scientific papers published (chapters 3 and 5) or submitted for publication, and presented as an arXiv manuscript (chapter 6). Each of the three chapters include also a brief introduction explaining research motivation as well as topics that interconnect the research.

- In chapter 1, a brief motivation for the research is presented as well as the description of the thesis structure.
- In chapter 2 theory of operation of MTJ in presented both in static and dynamic (oscillation) regimes.
- In chapter 4 concept of artificial neural networks, some of the types of such circuits as well as selected possible learning algorithms are presented.
- In chapter 3 a research paper describing multi-state magnetic random access memory (MRAM) cells is included and presented.

– In chapter 5 a research paper describing use of multi-state MRAM cells for hardware neuromorphic computing is included and presented.

– In chapter 6 a manuscript describing synchronization to an external high-frequency (RF) signal as well as mutual synchronization of electrically connected spin torque oscillators is included and presented.

– In chapter 7 a detailed description of fabrication and measurement techniques used during preparation of the thesis is presented. This includes details of nanolithography process, measurement setups as well different types of software that has been used and prepared to gather all the necessary data.

– In chapter 8 a brief summary of the work is presented as well as some prospects for future research.

2. Magnetic Tunnel Junctions and its static and dynamic behaviour

The effects laying at the base of all the spintronics were observed as early as 1857[15] where Thomson experimentally observed the different in the electrical resistance of a ferromagnetic conductor depending on the difference relative angle between magnetization vector and charge current. This effect was later named as the anisotropic magnetoresistance (AMR)[16] introducing a whole family of magnetoresistance effects. Although the effect is very mature, it is nowadays still used in practice in magnetic field sensing device[17]. Later a gigantic magnetoresistance (GMR) effect taking place between two ferromagnetic films separated by a thin non-magnetic conductive layer was discovered[8]. Due to a GMR effect the resistance of such multi-layer structure lowest when magnetization of both ferromagnetic elements are parallel, and highest for opposite magnetization vectors. Further research on the topic lead to replacing a non-magnetic layer with a thin insulator barrier, effectively forming a magnetic tunnel junction (MTJ)[18] which exhibit a tunelling magnetoresistance (TMR) effect. First MTJ operating in room temperatures was presented in in 1995 [19] and since the time a great progress in its parameters, fabrication and applications was made. From all the effects mentioned the TMR effect has the highest magnitude, and therefore emerges to have many practical applications, compared to other ones.

Nowadays MTJ exhibit tunnelling magnetoresistance ratio over 630 % [20] and are being used in various applications such as non-volatile memories [21, 1, 22], oscillators [23, 24], magnetic field sensors [25], read-heads in hard drives [22] and neuromorphic computing devices [26, 2, 27]. With such a wide range of usage of MTJs, research in this field is interesting and might provide solutions for further commercial applications, as usually MTJs are compatible with CMOS processes [28] used to manufacture modern integrated circuits.

This chapter describes basics of construction and operation of MTJs and physical phenomena: tunnel magnetoresistance (TMR), spin transfer torque (STT), current induced magnetization switching (CIMS) and spin torque oscillator (STO).

2.1. Magnetic tunnel junction

Typical MTJ is a type of electronic device that consists of two ferromagnetic (FM) layers separated by a thin insulating barrier that allows for tunneling of electrons. As this tunneling process depends on spin-polarized electrons it is effectively controlled by relative orientation of magnetization of FM layers [29]. If the magnetization of the two layers is parallel - the state is called a parallel (P) and the resistance is lowest (R_P), while for opposite magnetization vectors the state is anti-parallel (AP) and the resistance is highest (R_{AP}).

Some materials, like Fe or Co exhibit non-symmetrical density of states for electrons with spin up and spin down. Also this asymmetry is tightly coupled to the magnetization of the material (layer) that is taken under consideration. As during tunnelling between FM layers separated by an thin insulating layer electrons prefer not to change their spin polarization a simple two-current-path model might be used to explain TMR phenomena. Taking the mentioned asymmetry in density of states at conduction level into account it might be assumed that electrons with majority spins face low resistance, while electrons with minority spins face higher resistance during tunnelling. If the layers are in P state (Fig. 2.1a) then electrons that are the majority electrons for the first FM layer are also majority electrons for the second FM layer so they face low resistance during the tunnelling, while minority carriers face high resistance - so the result is one low-resistance path and one high-resistance path. For the opposite situation of AP state (Fig. 2.1b) the majority electrons from first FM layer become minority electrons in the second layer, and vice versa - therefore result is two paths with mixed resistance, which is higher than low resistance path from P case. This explains resistance changes of the MTJ multi-layer system as a function of relative layer magnetization.

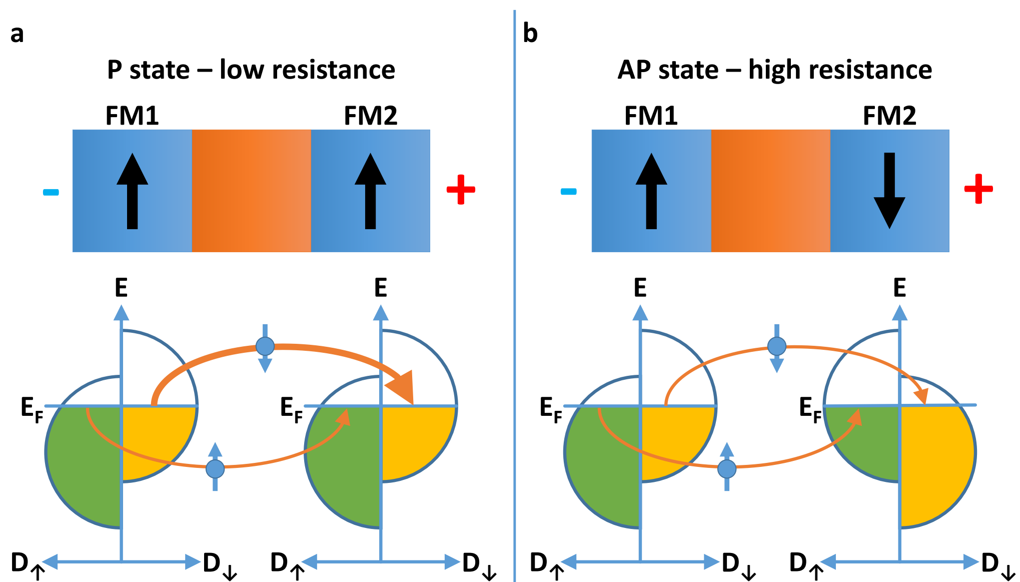

Figure 2.1: Explanation of the TMR effect in MTJ, as presented in [30].

To quantify the effect a tunneling magnetoresistance factor, TMR is defined as:

$$TMR = \frac{R_{AP} - R_P}{R_P} \tag{2.1}$$

According to simple model [18] TMR can also be expressed as a function of spin-polarisation of FM layers (P_{FMx}), which is the fraction of electrons that are becoming spin-polarized in each FM layer:

$$TMR = \frac{2 \cdot P_{FM1} \cdot P_{FM2}}{1 - P_{FM1} \cdot P_{FM2}}. \tag{2.2}$$

The spin polarization is a measure of degree of alignment spin of particles (in case of spin electronics - electrons) to a given direction. In a simplified case, when again only two possible spin values are considered and only electrons at E_f are considered it might be expressed as [31]:

$$P = \frac{N_{\uparrow}(E_f) - N_{\downarrow}(E_f)}{N_{\uparrow}(E_f) + N_{\downarrow}(E_f)}. \tag{2.3}$$

Generally a spin polarization is much more complex, and depends on many factors, such as material structure and composition, temperature or applied voltage.

The orientation of magnetization might be parallel to the plane of the device (in-plane - IP) or perpendicular to the plane (out-of-plane - PMA). This is controlled by minimal energy of the system, which for thin films consists of Zeeman, demagnetization and anisotropy energy. Usually the effective magnetic anisotropy energy (K_{eff}) is defining the direction of magnetization, and it might be calculated using following simplified formula [32]:

$$K_{eff} = K_b - \frac{1}{2}\mu_0 M_s^2 + \frac{K_i}{t}, \tag{2.4}$$

where K_b is the bulk crystalline anisotropy, μ_0 - magnetic permeability of the free space, M_s - magnetization saturation, K_i - interfacial anisotropy energy and t - layer thickness. For negative K_{eff} anisotropy is IP, and for positive - PMA is observed. Usually K_i is positive, and $K_b \ll \mu_0 M_s^2$. This means that by reducing thickness of the layer a PMA might be achieved, but this leads to significant decrease of the volume of the material, thus reducing layer's capability to spin-polarize electrons. The effective volume, however, might be increased without increasing thickness of the layer by using a multilayer structure, with interchanging thin ferromagnetic and non-magnetic (for example Pd or Pt) layers alternating [33, 34]. Another way to achieve a PMA is by the use of precisely engineered geometry of the free layer, which can be formed as an elongated cylinder[35] to achieve this goal. PMA in context of MRAM memories is often used because it reduces current needed for switching (writing) the cell [36], while in context of spin torque oscillators (STO) this might enable ferromagnetic layers' magnetization to be perpendicular to each other thus improving oscillation conditions.

Additional important part of the real MTJ is a method of engineering energies needed to switch both ferromagnetic layers. Usually one of them is by design coupled to a synthetic antiferromagnet (SAF) [37], what results in significant increase of the energy needed to alter the magnetization of the layer, therefore this layer is called pinned or a reference layer (RL). Other layer usually has significantly lower energy needed to change its magnetization, and therefore is called a free layer (FL).

2.2. Spin Transfer Torque and Current Induced Magnetization Switching

Initially, the magnetization state of MTJ was controlled with an external magnetic field however, necessity of applying magnetic field in some applications is not practical. In 1996 Slonczewski and Beger[38] theoretically predicted the existence of the effect opposite to the spin polarization phenomena - when the spin polarized current is passed by a ferromagnet with a magnetization non-collinear with the polarization of the spin, it exerts a torque on the local magnetic moment, that is called spin transfer torque (STT). The STT effect is responsible for oscillations observed in MTJs as well as ability to switch magnetization of an FL of MTJ without external magnetic field - the latter effect is called current induced magnetization switching (CIMS). Two major configurations for STT effect might be analysed in a simplified way. First, if the electrons are polarized on RL and are entering FL which magnetisation is non-collinear the current (Fig. 2.2a) will cause FL magnetization to deflect more and more in the direction of RL magnetization. Second, if the layers are polarized initially in a same direction (Fig. 2.2b) to observe STT electrons need to travel in the opposite direction (i.e. from FL to RL). In such case a number of electrons might change their spin polarization, and because of the pinning of RL the more energy-efficient path for them would be being back-scattered onto FL, and as they now will have polarization preferring opposite magnetization - a STT would cause FL magnetization to deflect more and more in opposite direction as referenced to RL. For both of the cases, if the STT effect is strong enough (practically it is related to current density) and the MTJ has suitable parameters a CIMS occurs.

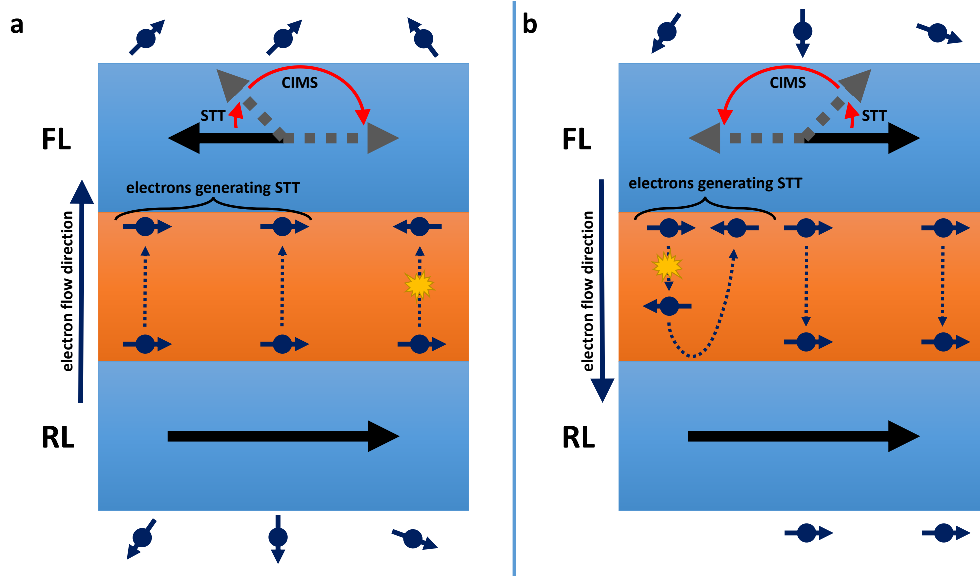

Figure 2.2: Explanation of the STT effect in MTJ, as presented in [30].

For the above case if the spin-polarized current density is high enough, so a transferred energy is enough to overcome energy barrier between P and AP state a permanent magnetization switching is observed. This phenomenon is called current induced magnetization switching (CIMS) and is a basic method of writing contemporary STT-MRAM memories. To calculate critical current needed for CIMS to occur in a given MTJ a following formula can be used [36]:

$$I_C^{PMA} \approx \frac{A\alpha M_S V}{g(\theta)p} \left(-H - H_{dip} \underset{(-)}{+} H_{K\perp} \underset{(+)}{-} M_S\right) \mu_0 \tag{2.5}$$

In the above equation 2.5 M_S, V and α are the saturation magnetization, volume and Gilbert damping constant for FL, respectively, θ is the relative angle between magnetizations of FL and RL, and the g factor depends on this angle, p is the magnitude of the angular dependence, A is a phenomenological factor dependent on transport model used, and it's unit is Wb^{-1}. H is the external magnetic field applied parallel to the easy axis of magnetization, H_{dip} is the dipole field from the RL acting on the FL. $H_{K\|}$ and $H_{K\perp}$ are the uniaxial IP anisotropy or PMA fields, respectively. $\theta = 180°$ and operators in brackets are true for AP to P switching, and $\theta = 0°$ and operators without brackets are true for switching from P to AP.

Another important parameter of an MTJ is its thermal stability Δ [39]. Higher the parameter is - harder it is to change relative magnetization of the free layer referenced to the fixed layer. This ensures longer data retention, but at the same time - makes it harder for the MTJ to switch. On the other hand lower Δ makes element unstable and prone to spontaneous switching. Engineering of the parameter by manipulating magnetic couplings inside MTJs, its composition and geometric parameters allows to obtain multitude range of behaviours, depending on desired application. For example for oscillators the Δ would be preferred to be lower, while for memory applications an equilibrium have to be settled, between increasing data retention while still allowing for energy

efficient and reliable write operations. Changing the diameter of the MTJ as well as thickness of a free layer or the MgO layer[39] might allow for a wide range of adjustment of $|Delta$ parameter. The thermal stability is also a contributing factor to switching time of the device, which is crucial parameter of each memory. Generally switching is a dynamic process, where in the intermediate state some oscillations are observed[40]. Bigger the Δ - bigger the magnetization oscillation dampening and thus switching time might be shorter, but from the other point of view bigger dampening means that higher energy would be needed to cause initial destabilization of the element, so a higher current density. Such increased current density usually shortens the switching time and makes the process more robust, until the limitation of maximum current density that does not damage the element is reached. Such relationships make the process of tuning MTJ to fit desired purpose even more challenging and complex.

2.3. Technologies competetive to MRAM

There are numerous techniques alternative to use of MTJ (as MRAM) for data storage and possibly neuromophic computing. They are worth mentioning but the MTJ technology proves to be most well-established in industry, as there are already numerous practical solutions available involving spin devices connected with CMOS circuits. Below are some of the examples of both classical and emerging MRAM volatile and non-volatile competitors:

– Static RAM (SRAM) - each bit is stored in a circuit of four transistors as long as they are powered, so there is a constant power consumption. Such solutions are the fastest of all the memory types. Contents of the memory might be damaged by radiation. The memory is volatile.

– Dynamic RAM (DRAM) - each bit is stored in a miniature capacitor-like structure in a form of an electrical charge. Such memories need to have this charge periodically refreshed, and also a refresh is needed after a readout operation, so there is a constant power consumption too. Contents of the memory might be damaged by radiation. The memory is volatile.

– FLASH - each bit is stored in a specially designed floating-gate of the MOS transistor in a form of well-trapped electrical charge. Due to the energy required to change the charge in the floating gate, each write cycle the insulating layer of floating gate degrades, however endurance of modern FLASH, together with clever algorithms used to spread data across whole array makes it a perfect long-term storage medium. Contents of the memory might be damaged by radiation. The memory is non-volatile.

– Redox RAM (ReRAM)[41] - base on chemical changes (oxidation and reduction - redox) induced by current flowing in the storage material, effectively causing changes of the

resistance. Due to nature of the process such element is subject to relatively rapid degradation, thus only limited write endurance might be achieved. The memory is immune to radiation. The memory is non-volatile.

– Ferroelectric RAM (FRAM)[42] - base on incorporating a ferroelectric material in a structure similar to cllasic Dynamic RAM (DRAM), where changes of polarization of crystalline material is used to store non-volatile data. Such memory has reasonable write endurance, but a drawback is need to refresh data after readout (readout is destructive) as well as very limited data density in sich technology. The memory is non-volatile.

– Phase Change RAM (PCRAM)[43] - base on materials, that under influence of temperature generated by flow of electric current in heating elements might change structure from crystalline to amorphous and vice-versa (depending on heat profile in time that is applied). Such memories are slow, not immune to operating temperature variations and also prone to degradation. The memory is non-volatile.

2.4. Magnetization dynamics of MTJs

As it was earlier mentioned, the behaviour of magnetization of FL in the MTJ is a dynamic process involving oscillation. The following Landau-Lifshitz-Gilbert-Slonczewski (LLGS) equation is used to describe the dynamics of magnetization [38, 44, 45, 46, 47]:

$$\frac{\mathrm{d}\mathbf{m}}{\mathrm{dt}} = \frac{-\gamma_0}{1+\alpha_{\mathrm{G}}^2}[\mathbf{m}\times\mathbf{H}_{\mathrm{eff}} + \alpha_{\mathrm{G}}\mathbf{m}\times\mathbf{m}\times\mathbf{H}_{\mathrm{eff}}] + \frac{-\gamma_0}{1+\alpha_{\mathrm{G}}^2}[a_j\varepsilon\beta(\mathbf{m}\times\mathbf{p}) + a_j\varepsilon(\mathbf{m}\times\mathbf{m}\times\mathbf{p})] \quad (2.6)$$

where $\mathbf{m} = \frac{\mathbf{M}}{M_s}$ is a normalised magnetisation vector, (M_{s} - magnetisation saturation), $\mathbf{H}_{\mathrm{eff}}$ - effective magnetic field, β - secondary parameter that describes the torque (usually set to 0 or equal to the damping parameter α_{G}), $\mathbf{p}$ - polarisation vector, and γ_0 - gyromagnetic factor. The variable a_j is defined in terms of current density j:

$$a_j = \frac{\hbar j}{e\mu_0 M_{\mathrm{s}} t_{\mathrm{FM}}} \quad (2.7)$$

where $\hbar$ is the reduced Planck constant and e is the electron charge. The variable ε depends on λ, the parameter of the spacer layer derived by Slonczewski, and η, the efficiency of the spin current polarisation ($0 \leq \eta \leq 1$):

$$\varepsilon = \frac{\eta\lambda^2}{\lambda^2 + 1 + (\lambda^2 - 1)\mathbf{m}\cdot\mathbf{p}} \quad (2.8)$$

Usually, λ is 1, which consequently removes the dependence of torque magnitudes on $\mathbf{m}\cdot\mathbf{p}$.

Depending on numerous parameters, like but not limited to: Δ, geometry, current density and input waveform the oscillations might be dampened after a time or being sustained. While the first is usually required for memory applications, the latter allows for the MTJ operating as a spin

torque oscillator (STO). To theoretically explain all of these phenomena the LLGS equation might be solved numerically [48, 49] to derive solution for behaviour of magnetization of the MTJ. This theory is nowadays used to explain dynamics of STOs[?], that have also been intensively studied since the first oscillation effects in the class of the devices were observed[50]. STOs usually have quite wide full-width-half-maximum (FWHM), therefore usage as a precise oscillators replacing quartz resonators is not feasible. However various different applications might be proposed, such as ultra-fast magnetic field sensors[51], or as part of various neuromophic computing schemes[52].

Another class of spintronic devices that use dynamic response of the MTJ is a spin diode (SD)[53]. The SD effect is opposite to the STO, where the first one converts DC input into RF signal, while the latter with a correctly matched (resonant) frequency of the RF signal produces a DC output - acting as a selective detector/rectifier. The effect might be used to characterize STT effect during research[54, 55], as well as more practical applications might be found, such as energy harvesting[56] or neuromorphic computing[57].

3. Multistate MRAM memory cells

Magnetic Random Access Memories (MRAM) are nowadays well-established type of non-volatile storage devices. Despite commercial devices being already well established on a market, ways to improve their density as well as find new applications and modes of operation are still interesting research topics.

As a starting point for the research a typical Spin Transfer Torque MRAM (STT-MRAM) cell was taken into consideration. It was noted, that for such a cell usually transistor required to switch its state is considerably larger[58] than a cell itself, due to the fact that it have to withstand considerably large current needed to switch the connected cell. This lead to the conclusion that it would be beneficial in terms of data density to have multiple cells connected to a single transistor and effectively increase capacity per area of such memories.

It was noted, that such solution should involve a device, that effectively would be able to store multiple bits, while being a two-port part connected to a single gate-transistor. Theoretically a few possible schemes of connecting individual MTJs were analyzed. Initially a parallel connection was rejected due to the fact, that if one of the connected devices would have lower resistance (i.e. be in low-resistance state) the majority current would take its path, thus disallowing for other elements to be switched. Such observation also makes any mixed connection impractical.

While analysing serial head-to-head connection it was noted, that in such connection while one element would get switched to low-resistance state the other one would become high-resistance, so overall device resistance change would be minimal. Completely other behaviour was excepted from head-to-tail connection. For such a situation, with powering the device with voltage source, it was predicted, that (considering low-to-high resistance switching) as one of the element switches to high-resistance state, the overall current would drop, thus preventing other elements from switching. To switch other elements it was excepted that a voltage would need to be further increased - such behaviour will reassemble ratcheting mechanism.

It is worth noting, that serial connections of MTJs are widely used in sensor devices[59, 60, 61, 62]. For such applications the serial connection increases sensitivity of such sensor while also reducing a noise level of the output signal. This however is not related to the application presented in the paper, as for sensor applications a linear response and no hysteresis are excepted, while for memory applications opposite have to be used.

The latter arrangement was prepared experimentally and extensively tested. Experiments revealed that such a connection behaves as excepted - allowing for being stable in multiple resistance states, while maximum current required for switching was not higher than switching current for a single element. During experiments up to seven serially connected MTJs were tested, what reassembled a 3-bit STT-MRAM cell.

The details of that research were described in the following research paper, together with precise characterization of a single MTJ element used. Also observations made during the research established a direction of further research, aiming towards neuromorphic computing.

Journal of Applied Physics ARTICLE scitation.org/journal/jap

Multi-bit MRAM storage cells utilizing serially connected perpendicular magnetic tunnel junctions

Cite as: J. Appl. Phys. **125**, 223907 (2019); doi: 10.1063/1.5097748
Submitted: 28 March 2019 · Accepted: 24 May 2019 ·
Published Online: 14 June 2019

Piotr Rzeszut,[1,a)] Witold Skowroński,[1] Sławomir Ziętek,[1] Jerzy Wrona,[2] and Tomasz Stobiecki[1,3]

AFFILIATIONS

[1]Department of Electronics, AGH University of Science and Technology, Al. Mickiewicza 30, 30-059 Kraków, Poland
[2]Singulus Technologies, Kahl am Main 63796, Germany
[3]Faculty of Physics and Applied Computer Science, AGH University of Science and Technology, Al. Mickiewicza 30, 30-059 Kraków, Poland

[a)]**Electronic mail:** piotrva@agh.edu.pl

ABSTRACT

Serial connection of multiple memory cells using perpendicular magnetic tunnel junctions (pMTJs) is proposed as a way to increase magnetic random access memory (MRAM) storage density. A multibit storage element is designed using pMTJs fabricated on a single wafer stack, with serial connections realized using top-to-bottom vias. The tunneling magnetoresistance effect above 130%, current induced magnetization switching in zero external magnetic field, and stability diagram analysis of single, two-bit, and three-bit cells are presented together with thermal stability. The proposed design is easy to manufacture and can lead to an increased capacity of future MRAM devices.

Published under license by AIP Publishing. https://doi.org/10.1063/1.5097748

I. INTRODUCTION

Spin transfer torque magnetoresistive random access memories (STT-MRAMs) have numerous advantages over existing storage technologies, including theoretically unlimited endurance, high read and write speeds, and ionizing-cosmic-radiation resistance.[1,2] However, state-of-the-art memories have limited capacity due to the fact that the current density needed to switch a cell (typically made of a single magnetic tunnel junction) requires relatively large transistors.[3,4] Such an obstacle can be overcome using the architecture that incorporates a multibit cell driven by a single transistor.

To date, very few practical implementations of multibit MRAM cells have been presented.[5,6] This is mainly due to the fact that efforts were made to produce a single storage element capable of being stable in more than two states or to produce multiple storage elements on top of each other.[7–9] Both of these approaches are very challenging to manufacture.

In this work, an alternative approach is proposed—perpendicular magnetic tunnel junctions (pMTJs)[10–12] are connected electrically in series and a multistate behavior is observed that leads to a multibit storage capability. Theoretical explanation as well as experimental results (including the working three-bit cell) is presented. In addition, such an approach can be implemented to design and fabricate an artificial synapse for a neuromorphic computing scheme.[9,13–17]

II. PRINCIPLES OF OPERATION

The discussed pMTJs consist of a top free layer (FL), a MgO tunnel barrier, and a bottom reference layer (RL), which is magnetically pinned to the synthetic ferromagnet (SyF).[18] In the proposed serial connection of pMTJs in a storage cell, the top contact of the first element is connected to the bottom contact of the next element (head-to-tail), as shown in the inset of Fig. 1. This results in the charge current flowing through all the cells involved in the same direction. Connections can be made using metallization and vias or any other suitable techniques.

The behavior of the presented arrangement of storage elements can be predicted by analyzing characteristics of two pMTJs connected (Fig. 1). If both elements are in the parallel (P) state, the lowest resistance is observed (1). When a positive voltage is applied [which corresponds to the current flow that favors antiparallel (AP) state], the current increases, until it reaches a critical value, which

Published under license by AIP Publishing.

Journal of Applied Physics ARTICLE scitation.org/journal/jap

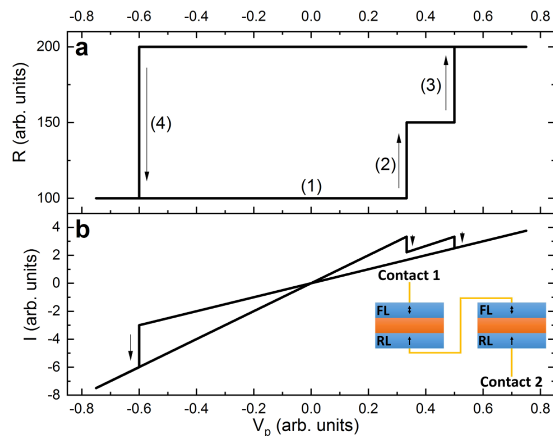

FIG. 1. Theoretically predicted (a) resistance and (b) current vs voltage applied to a storage cell consisting of two serially connected pMTJs. Inset: schematic of serial connection of two pMTJs.

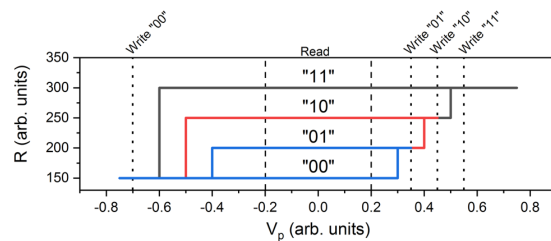

FIG. 2. Theoretically predicted resistance vs voltage applied to the proposed two-bit cell. Possible mapping between resistance and binary value as well as proposed voltages to write and read the cell is presented on the plot. Different colors represent the behavior of the cell after different writing voltages application.

results in the current induced magnetization switching (CIMS) (2). As one of the elements switches to the AP state, with constant voltage applied, the current decreases. This prevents the remaining element of the cell from switching, as the current drops below the critical value. By further increasing the voltage, the critical current is reached again, and the second pMTJ switches to the AP state (3).

By reversing the current polarization, the switching to the P state is achieved. In this case, as soon as the critical current is reached, one of the elements switches to the P state (4). With constant voltage applied, the current rises above the critical value, causing the other element to switch to the P state.

The above mechanism works also for more than two elements, and similar reasoning can be carried out. For the serial pMTJs connection utilizing the presented mechanism, $N + 1$ stable resistance states would be observed for N elements connected, resulting in storage ability of $\log_2 (N + 1)$ bits. This is because there is no possibility to individually determine states of all incorporated storage elements; as ideally, they are characterized by the same resistance—only the number of elements in P and AP states may be determined, based on the two-point resistance measurement.

The storage cell capable of storing two bits of data would, therefore, consist of three serially connected storage elements. The predicted resistance vs voltage characteristics of such a storage cell are presented in Fig. 2. Voltages for writing different states, as well as reading the cell, can be defined based on the characteristics obtained for a single pMTJ. Note that in the proposed cell configuration, writing smaller bit value (smaller resistance) than the existing state requires clearing the state to “00” (the lowest resistance) and writing a new value.

A similar solution was suggested by Raymenants *et al.*;[6] however, with a different arrangement of subsequent elements, which are connected in opposite directions (head-to-head and tail-to-tail). Such a multilevel cell, though, needs application of variable external magnetic fields to have an ability to be written with any desired state, what is not the case for our design, where the read–write process is much simpler. On the other hand, our solution has by design a limited number of stable states to $N + 1$.

A similar mechanism was also suggested by Zhang *et al.*,[13] with elements fabricated on top of each other; however, due to experimental difficulties, only two working elements connected in series were fabricated.

In our work, these drawbacks of other designs are eliminated, and the presented arrangement is ready to be manufactured using an unmodified fabrication process.

III. EXPERIMENT

Multilayer of the following structure: buffer/Co(0.5)–Pt(0.2) based SyF/W(0.25)/CoFeB(1)/MgO(0.89)/CoFeB(1.3)/W(0.3)/CoFeB(0.5)/MgO(0.75)/capping layers (thickness in nanometers) patterned into pillars of around 130 nm diameter were used as the pMTJ basic cell. The details of the deposition and fabrication processes are presented in Refs. 19 and 20. Elements were equipped with $100 \times 100\,\mu m^2$ Al(20)/Au(30) contact pads that enable both individual pMTJ characterization as well as measurement of the elements connected in series forming a multibit cell. The schematics of the multilayer stack, a fabricated pMTJ pillar, and a micrograph of a two-bit (three pMTJs in series) cell are presented in Fig. 3. In order to determine the ability of a single element to act as a memory device, two types of characterization were performed: a stability diagram[19] and thermal stability[21] measurements.

The stability diagram was determined as follows: pMTJ resistance (R) vs voltage pulse amplitude (V_p) measurements were repeated with different external magnetic field (H) applied. The voltage pulse length was set to 10 ms. Each point on the stability diagram corresponds to the transition from the P to AP state or the AP to P state, depending on the initial magnetization configuration. The thermal stability was determined from the R vs H measurement repeated around hundred times with a magnetic field changing in 1 s long magnetic field steps of 80 A/m.

J. Appl. Phys. **125**, 223907 (2019); doi: 10.1063/1.5097748 **125**, 223907-2
Published under license by AIP Publishing.

Journal of Applied Physics ARTICLE scitation.org/journal/jap

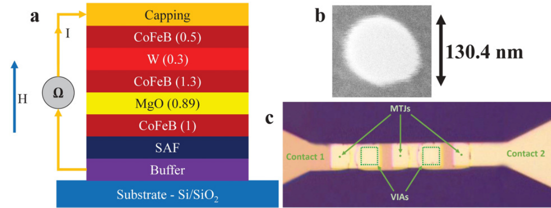

FIG. 3. (a) pMTJ layer structure, "SAF" denotes synthetic antiferromagnet, *H* denotes external magnetic field direction, *I* denotes current direction, Ω denotes the sourcemeter or the cell driving circuit. (b) Scanning electron microscope image of a single pMTJ. (c) Micrograph of three serially connected pMTJs.

IV. RESULTS AND DISCUSSION

A. Single pMTJ characterization

An example of the $R(V_p)$ loop and the stability diagram are presented in Fig. 4. The TMR ratio of 135% and the resistance area (RA) product of $21.6\,\Omega\mu\text{m}^2$ were measured. These values, however, are influenced by series resistance of vias and contacts, which could not be eliminated due to two-wire measurement; in fact, the TMR ratio of the element is higher.[20] In the absence of an external magnetic field, the P to AP transition occurs for the voltage of around 0.25 V (corresponding to the critical current density of $2.00\,\text{MA/cm}^2$), whereas the AP to P switching is measured for $V_p = -0.15$ V (corresponding to $J_{crit} = -0.54\,\text{MA/cm}^2$). Multiple $R(H)$ measurements, performed on the same pMTJ, allowed one to obtain the switching probability vs H using the analysis described

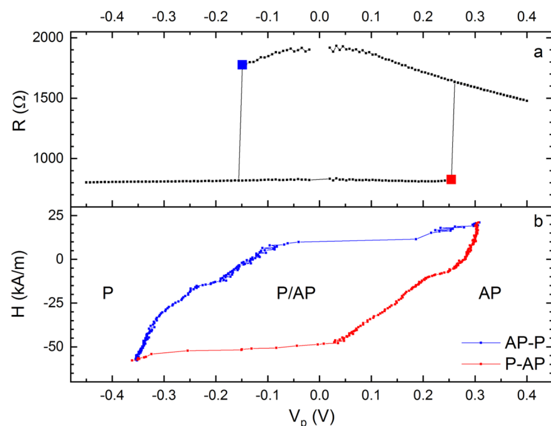

FIG. 4. (a) Representative *R-V* loop of a single pMTJ, with switching voltages from P to AP (red) and from AP to P (blue) marked using big squares, measured without external magnetic field. (b) A stability diagram with marked regions where P, AP, or both of the states are stable.

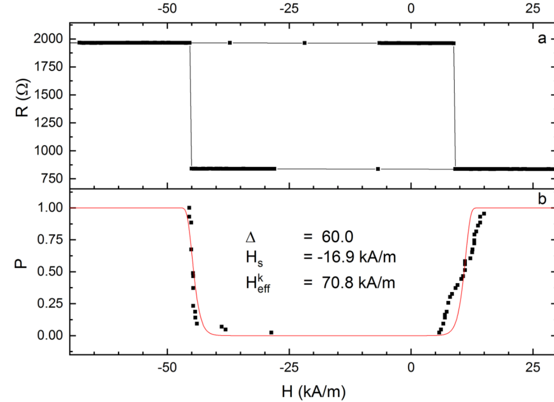

FIG. 5. (a) Representative *R-H* loop of a single pMTJ. (b) Calculated switching probability (black points) and theoretical fit based on Eq. (1).

in Ref. 21 with the following equation:

$$P(\tau) = 1 - \exp\left[-\frac{\tau}{\tau_0}\exp\left\{-\Delta\left(1 - \frac{|H - H_s|}{H_k^{eff}}\right)\right\}\right]. \quad (1)$$

In Eq. (1), τ denotes the magnetic field step duration (in this study, $\tau = 1$ s), τ_0 denotes the inverse of the attempt frequency (in this work it is assumed to be 1 ns), Δ denotes the thermal stability, H_s denotes shift field, and H_k^{eff} denotes the effective magnetic anisotropy field.

The best fit of Eq. (1) to the experimental switching probability resulted in $\Delta = 60$, which together with a capability of the pMTJ of being stable in both P and AP states in the absence of an external magnetic field proves that the cell is suitable to be used as a memory device (Fig. 5).

B. Two-bit storage cell

Next, we move on to the two-bit cell consisting of three pMTJs connected in series. $R(V_p)$ measurement of such a system is presented in Fig. 6(a)—initially, the two-bit cell is in the low resistance state. The application of the positive voltage of around 0.37 V (corresponding to a single pMTJ switching from P to AP state) results in the transition to higher resistance state, which is denoted as "01." Further increase of voltage to around 0.67 V causes a second pMTJ transition to a higher resistance state—thus "10" state is written. Finally, after the application of 0.80 V, all three pMTJs are in the AP state, which is denoted as the "11" state. A negative voltage of -1.15 V switches all pMTJs back to the P state. The behavior described in Sec. II was confirmed—four stable states can be defined and binary numbers can be assigned to them:

- All elements in the AP state—11.
- One element in P state and two in the AP state—10.
- Two elements in AP state and one in the P state—01.
- All elements in the P state—00.

Published under license by AIP Publishing.

Journal of Applied Physics ARTICLE scitation.org/journal/jap

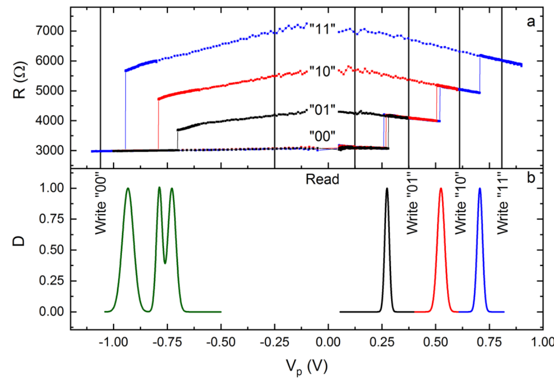

FIG. 6. (a) CIMS measurement of the two-bit memory cell. The proposed binary coding is also presented. (b) Switching voltages distribution, with regions for writing, and safe readout presented.

By repeating *R-V* measurement of the two-bit cell around hundred times and calculating switching voltage distributions, writing voltages of particular states, as well as a region safe for reading the storage cell, can be defined [Fig. 6(b)].

The principle of operation, involving the current decreasing below the critical current after one element switching into the AP state, was confirmed (Fig. 7). Due to the nonideal manufacturing process, critical currents of all incorporated elements are nonequal, but this has no adverse effect on the process (Fig. 7, inset).

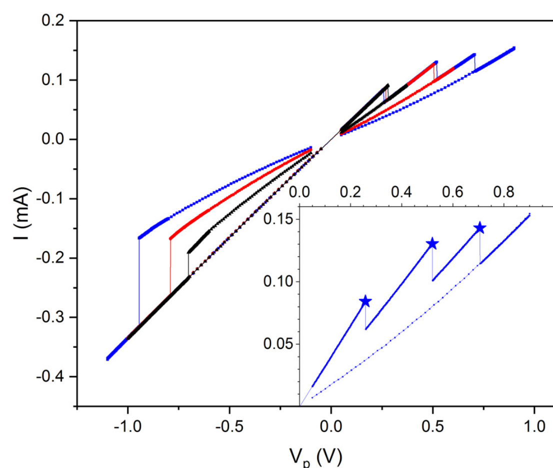

FIG. 7. Current changes during *R-V* measurement for the storage cell constructed of three storage elements. Inset: a close up of current in the CIMS measurement for writing the "11" cycle. Critical currents causing subsequent elements to switch to the AP state are marked with stars.

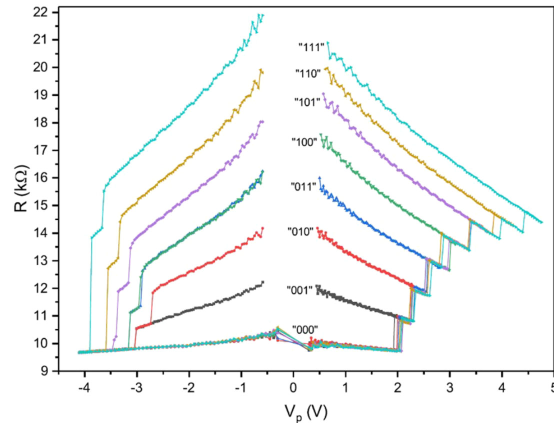

FIG. 8. *R-V* measurement of the three-bit cell consisting of seven pMTJs connected in series. The proposed binary coding is presented.

C. Three-bit storage cell

Finally, the proof-of-concept of the three-bit cell consisting of seven pMTJs connected in series is presented. As predicted, the cell exhibited eight stable states (Fig. 8). Due to the nonideal fabrication process, it was noted that regions for writing voltages of some of the states are very narrow because of variation of the switching voltage (related with the switching current distribution). The switching back to the "000" state was not ideal in the case, which may originate from a resistive behavior of the cell.[22] Nonetheless, the proposed architecture is valid for a multiple pMTJ that forms the multibit memory cell.

V. SUMMARY

In summary, we showed that a multibit memory cell can be successfully implemented using serially connected pMTJs. The state-of-the-art multilayer structure characterized by TMR of 135% and RA of 21.6 $\Omega\mu m^2$ was used to design two- and three-bit MRAM cells. The developed method of fabrication and driving multibit nonvolatile storage elements is a significant improvement in MRAM technology, as it allows one to store more data using the same area of the memory. This may be achieved by driving a multibit storage cell using a single transistor rated for the same current, as a single storage element (the critical current remains the same for any number of serially connected elements). Also, the fabrication process does not require significant changes compared to single storage element fabrication. The presented three-bit cell design requires around $26 \times 54\,\mu m^2$, most of which is occupied by vias and interconnections. The state-of-the-art CMOS technology enables fabrication of vias of around 100 nm, which could result in a cell size of around $1\,\mu m^2$. This method, however, exhibits some capacity limitations, mainly due to the variation of parameters of pMTJs, such as switching voltage, TMR ratio, or resistance of the individual element involved in a cell. It is noted that

Published under license by AIP Publishing.

Journal of Applied Physics ARTICLE scitation.org/journal/jap

contemporary STT-based MRAM operates at a nanosecond-long scale[23] and, therefore, the operation of the multibit cell at this time scale requires further study. In addition, the proposed solution may be utilized in the neuromorphic computing scheme as a multistate nonvolatile memory block.

ACKNOWLEDGMENTS

This work is supported by the Polish Ministry of Science and Higher Education Diamond Grant (No. 0048/DIA/2017/46) and the Polish National Centre for Research and Development (Grant No. LIDER/467/L-6/14/NCBR/2015).

T.S. acknowledges the SPINORBITRONICS project through the National Science Centre Poland under Grant No. 2016/23/B/ST3/01430.

The nanofabrication process was performed at the Academic Centre for Materials and Nanotechnology (ACMiN) of AGH University of Science and Technology.

REFERENCES

[1]A. D. Kent and D. C. Worledge, "A new spin on magnetic memories," Nat. Nanotechnol. **10**, 187 (2015).
[2]B. Dieny, R. Sousa, J. Herault, C. Papusoi, G. Prenat, U. Ebels, D. Houssameddine, B. Rodmacq, S. Auffret, L. Buda-Prejbeanu *et al.*, "Spin-transfer effect and its use in spintronic components," Int. J. Nanotechnol. **7**, 591–614 (2010).
[3]T. Kawahara, R. Takemura, K. Miura, J. Hayakawa, S. Ikeda, Y. Lee, R. Sasaki, Y. Goto, K. Ito, T. Meguro *et al.*, "2Mb spin-transfer torque RAM (SPRAM) with bit-by-bit bidirectional current write and parallelizing-direction current read," in *2007 IEEE International Solid-State Circuits Conference, ISSCC 2007, Digest of Technical Papers* (IEEE, 2007), pp. 480–617.
[4]S.-W. Chung, T. Kishi, J. Park, M. Yoshikawa, K. Park, T. Nagase, K. Sunouchi, H. Kanaya, G. Kim, K. Noma *et al.*, "4Gbit density STT-MRAM using perpendicular MTJ realized with compact cell structure," in *2016 IEEE International Electron Devices Meeting (IEDM)* (IEEE, 2016), pp. 27.1.1–27.1.4.
[5]W.-C. Jeong, B.-I. Lee, and S.-K. Joo, "Three level, six state multilevel magnetoresistive RAM (MRAM)," J. Appl. Phys. **85**, 4782–4784 (1999).
[6]E. Raymenants, A. Vaysset, D. Wan, M. Manfrini, O. Zografos, O. Bultynck, J. Doevenspeck, M. Heyns, I. P. Radu, and T. Devolder, "Chain of magnetic tunnel junctions as a spintronic memristor," J. Appl. Phys. **124**, 152116 (2018).
[7]K. Ju, and O. Allegranza, "Multibit cells schemes for toggle MRAM applications," IEEE Trans. Magn. **42**, 2730–2732 (2006).
[8]T. Ishigaki, T. Kawahara, R. Takemura, K. Ono, K. Ito, H. Matsuoka, and H. Ohno, "A multi-level-cell spin-transfer torque memory with series-stacked magnetotunnel junctions," in *2010 Symposium on VLSI Technology* (IEEE, 2010), pp. 47–48.
[9]S. Lequeux, J. Sampaio, V. Cros, K. Yakushiji, A. Fukushima, R. Matsumoto, H. Kubota, S. Yuasa, and J. Grollier, "A magnetic synapse: Multilevel spin-torque memristor with perpendicular anisotropy," Sci. Rep. **6**, 31510 (2016).
[10]T. Kishi, H. Yoda, T. Kai, T. Nagase, E. Kitagawa, M. Yoshikawa, K. Nishiyama, T. Daibou, M. Nagamine, M. Amano *et al.*, "Lower-current and fast switching of a perpendicular TMR for high speed and high density spin-transfer-torque MRAM," in *2008 IEEE International Electron Devices Meeting* (IEEE, 2008), pp. 1–4.
[11]S. Ikeda, K. Miura, H. Yamamoto, K. Mizunuma, H. Gan, M. Endo, S. Kanai, J. Hayakawa, F. Matsukura, and H. Ohno, "A perpendicular-anisotropy CoFeB–MgO magnetic tunnel junction," Nat. Mater. **9**, 721 (2010).
[12]H. Kubota, S. Ishibashi, T. Saruya, T. Nozaki, A. Fukushima, K. Yakushiji, K. Ando, Y. Suzuki, and S. Yuasa, "Enhancement of perpendicular magnetic anisotropy in FeB free layers using a thin MgO cap layer," J. Appl. Phys. **111**, 07C723 (2012).
[13]D. Zhang, L. Zeng, K. Cao, M. Wang, S. Peng, Y. Zhang, Y. Zhang, J.-O. Klein, Y. Wang, and W. Zhao, "All spin artificial neural networks based on compound spintronic synapse and neuron," IEEE Trans. Biomed. Circuits Syst. **10**, 828–836 (2016).
[14]J. Torrejon, M. Riou, F. A. Araujo, S. Tsunegi, G. Khalsa, D. Querlioz, P. Bortolotti, V. Cros, K. Yakushiji, A. Fukushima *et al.*, "Neuromorphic computing with nanoscale spintronic oscillators," Nature **547**, 428 (2017).
[15]C. Sung, H. Hwang, and I. K. Yoo, "Perspective: A review on memristive hardware for neuromorphic computation," J. Appl. Phys. **124**, 151903 (2018).
[16]O. Sulymenko, O. Prokopenko, I. Lisenkov, J. Åkerman, V. Tyberkevych, A. N. Slavin, and R. Khymyn, "Ultra-fast logic devices using artificial "neurons" based on antiferromagnetic pulse generators," J. Appl. Phys. **124**, 152115 (2018).
[17]S. Fukami and H. Ohno, "Perspective: Spintronic synapse for artificial neural network," J. Appl. Phys. **124**, 151904 (2018).
[18]D. Worledge, G. Hu, D. W. Abraham, J. Sun, P. Trouilloud, J. Nowak, S. Brown, M. Gaidis, E. O'Sullivan, and R. Robertazzi, "Spin torque switching of perpendicular Ta/CoFeB/MgO-based magnetic tunnel junctions," Appl. Phys. Lett. **98**, 022501 (2011).
[19]W. Skowroński, M. Czapkiewicz, S. Ziętek, J. Chęciński, M. Frankowski, P. Rzeszut, and J. Wrona, "Understanding stability diagram of perpendicular magnetic tunnel junctions," Sci. Rep. **7**, 10172 (2017).
[20]W. Skowroński, S. Łazarski, P. Rzeszut, S. Ziętek, J. Chęciński, and J. Wrona, "Influence of a composite free layer structure on thermal stability of perpendicular magnetic tunnel junction," J. Appl. Phys. **124**, 063903 (2018).
[21]H. Sato, M. Yamanouchi, K. Miura, S. Ikeda, R. Koizumi, F. Matsukura, and H. Ohno, "CoFeB thickness dependence of thermal stability factor in CoFeB/MgO perpendicular magnetic tunnel junctions," IEEE Magn. Lett. **3**, 3000204 (2012).
[22]Y. Zhang, W. Cai, W. Kang, J. Yang, E. Deng, Y.-G. Zhang, W. Zhao, and D. Ravelosona, "Demonstration of multi-state memory device combining resistive and magnetic switching behaviors," IEEE Electron Device Lett. **39**, 684–687 (2018).
[23]T. Andre, S. M. Alam, D. Gogl, J. Barkatullah, J. Qi, H. Lin, X. Zhang, W. Meadows, F. Neumeyer, G. Viot *et al.*, "ST-MRAM fundamentals, challenges, and outlook," in *2017 IEEE International Memory Workshop (IMW)* (IEEE, 2017), pp. 1–4.

Published under license by AIP Publishing.

4. Artificial Neural Networks

Artificial Neural Networks (ANN) [63, 64] are emerging solutions to perform computational tasks in different way than classical algorithms. ANNs are based as a concept of mimicking a structure and operation of a brain of biological organisms. A representative neuron cell has a number of dendrites (input paths) and one axon (output path), which conduct electro-chemical signals in and out. An output signal is produced only when input signals are sufficient and its level depends on levels and number of input signals. The operation of a brain is mainly defined by existing interconnections between neurons as well as effectiveness of signal conduction from axon to dendrites of other neurons. Additionally such a contact is called a synapse and this term is used to describe a connection between neurons. Usually the results produced by ANN are not $100\,\%$ accurate, but for a given types of computational tasks, such as image recognition, sound analysis, deep learning, forecasting [65, 66, 67, 68, 69] it is allowed to have a result with a limited level of confidence, as traditional algorithms solving such problems are also not fully precise. The advantage of the ANN over traditional solutions are usually speed of operation as well as lower power consumption.

Usually ANN consists of [70]:

- Input layer, that brings input signals into the network and adjusts their level and format to match operation of the ANN.
- Hidden layer(s), where each neuron is connected to all or a subset of outputs of neurons from previous layer. Each connection (synapse) may introduce a weight applied to toe signal.
- Output layer, that presents the result and converts its format to a desired format.

For a single hidden layer an ANN is simply called a (basic) neural network, while with a multiple hidden layers a term of deep neural network is used.

4.1. Comparision of Artificial Neural Networks Architectures

Generally there is no strict definition or a recommended construction of an artificial neural network, as there are many variations on this topic. As a first criteria we might consider the

fact on how the calculations are performed. As any computational tasks, ANN operations might be performed using software on digital machines, sometimes equipped with some dedicated co-processing units such as digital Application Specific Integrated Circuits (ASIC) and/or Flexible Programmable Gate Arrays (FPGA) which can provide dedicated and re-configurable digital hardware accelerating such calculations[71, 72, 73, 74]. Such approaches, however, are not efficient in terms of energy consumption and speed of operation, due to big overhead originated from a lot of add-multiply operations needed to be performed. Such solutions are far from optimal: when using classic microprocessor architectures operations must be performed one by one and therefore reducing speed, while if dedicated digital architecture is created a footprint (as well as power consumption) of such device increases, as multiplication hardware occupies large area in integrated circuits.

In contrast to above various types of non-digital hardware implementations might be in use. This, in contrast to ASICs and FPGAs, will utilize dedicated hardware to perform operations in a way different than using component to perform mathematical operations on some digital numbers.

An interesting example of ANN which can be placed between digital and pure hardware implementations is binary neural network [75]. In such network each synapse can take only one of two states (0 or 1) and operations might be realized by quite simple arrangements of logic gates, which might be also implemented in FPGAs and simple ASICs.

Other family of ANN are spiking neural networks [76, 77], where information is propagated not as a constant voltage (or current flow) but rather as pulses, where information might be passed as their duty cycle, frequency or amplitude or combination of all of these. Such an approach tends to be more energy efficient [78] and in fact is a closest mimicking of how real neurons work. Such networks often relate to a probability of an building element (called p-bit) to change its state depending on applied signal intensity, or an ability of the element to change its parameters in a continuous manner, depending on actual and previous signals received.

An interesting family of ANN is a configuration where information is encoded by a signal frequency, usually in radio frequency (RF) regime. As frequency-modulated signals are more immune to noise and also utilize different properties of elements used in synapses, enabling for completely novel approaches in the field. Some of such solutions involve spin torque oscillators [52, 79] for performing various types of neuromoprhic computing. Some previous research[80] used electrically connected spintronic nano-oscillators working in regime of a few hundreds of MHz to recognize some simple spoken words, that indicated a successful match by synchronization of devices and thus increase of the output power. Different types than STO of spintronic oscillators, like spin-hall oscillators[81] are also successfully used to construct neuromorphic computing devices. Other interesting solutions use opposite behaviour of spintronic devices - a spin diode (SD) effect[57]. For such solutions usually input frequencies are fed separately to SD devices connected in series and tuned to various frequencies. At the output of

serial connections a DC signal represents the result of operation of such a neuron.

Also a concept of reservoir computing[82] is worth mentioning, as it might be a lead to some interesting solutions. Such kind of neural network uses a fixed-dynamics of so called reservoir, that processes input information in a way that might be not well-defined and not trained (like ripples on surface of water tank, created by input disturbance, oscillations of some coupled elements, ...). Then the only part of such network that is trained is an output layer, that receives signals form the reservoir and formats them into useful output. Such concept was also recently demonstrated using STOs[83], that formed a reservoir, which was the main part of the circuit calculating data parity. In the research STOs were forced into synchronization in order to improve their oscillation quality by reducing thermal fluctuations.

4.2. ANN Learning

Just as there are many methods of designing of ANNs, there is also a wide range of ways to "program" the network to perform desired operation. It is often impractical to calculate parameters of the ANN using a mathematical model and therefore other methods are being used, such as but not limited to:

– Backpropagation

– Gradient descent

– Genetic algorithms

Backpropagation is the most widely used method for training ANNs. It involves two phases: forward propagation and backward propagation. During forward propagation, input data is fed into the network, and its output is computed layer by layer. The computed output is then compared to the desired output, and the error is calculated. In the backward propagation phase, the error is propagated back through the network, and the weights and biases are adjusted to minimize the error using gradient descent or related optimization techniques.

Gradient descent is an optimization algorithm used to update the weights and biases of a neural network during training. It works by calculating the gradient of the network's error function with respect to the weights and biases. The weights and biases are then adjusted in the opposite direction of the gradient to minimize the error. There are variations of gradient descent, such as stochastic gradient descent, which updates the weights and biases after processing each individual training example, and batch gradient descent, which updates them after processing a batch of training examples.

Genetic algorithms might also be used to train ANNs in a way that is close to how real neural networks learn. They introduce a fitness of the solution - the measure of how accurate the system

works. Than a starting point is selected and a fitness is evaluated. In a following step a population is generated, where each variant (specimen) has network coefficients randomly varied from starting point. Than a fitness of each specimen is evaluated and a best one is selected as a new starting point. The process is repeated until fitness of the solution reaches excepted value.

4.3. Voltage feed-forward ANN

The simplest approach on ANN is to encode information inside network as well as input and output data as analogue voltages. Also as the network allows for the data from in one direction, without loops, it is called feed-forward ANN (Fig. 4.1). Such implementation was evaluated in this work, where each synapse is based on MTJs.

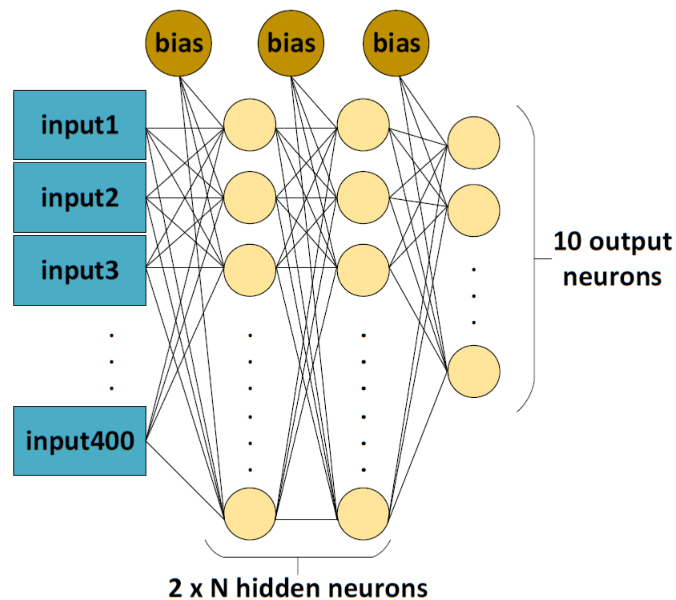

Figure 4.1: A schematic of representative feed-forward ANN with 400 inputs, 2 hidden layers of N neurons each and 10 output neurons, as presented in [2].

For such a network a single neuron might be described using following simplified formula:

$$S_{OUT} = f\left(\sum_{n=1}^{m} S_{INn} * k_n\right), \tag{4.1}$$

where S_{OUT} is the output signal of the neuron, f - neuron transfer/decision function, m - number of neuron synapses (dendrites), S_{INn} - the n-th neuron input signal and k_n - the n-th neuron input weight. Such an approach is one of the most common in neural networks, and as can bee seen the most resource consuming part is generating a weighted sum of the input signals. This leads to big effort being put to use dedicated and energy-efficient hardware resources to accomplish the task.

5. Neuromorphic computing architecture based on MTJs

The previously conducted research lead to construction of multi-state MRAM cells, however the opportunity to use constructed elements for applications other than data storage were investigated. One of such identified possibilities was neuromorphic computing. It was identified that one of the issues in hardware implementations of ANNs is lack of capable memristive device, that would allow to adjust synapse gain in voltage feed-forward neural networks. This gap was a potential application of the multi-state MRAM cells.

As at this stage of research, and also considering available resources practically implementing a fully-operational neural network was not sufficient a decision was made to prepare an extensive simulation of such circuitry. This involved preparation and verification of an advanced behavioral model of the MTJ to be used as a building block for ANN. Such a model was then used to simulate serially connected MTJs and positively verified against experimental data.

A circuit to be used in such network was designed to realize voltage feed-forward ANN. At first an electrical circuit was designed to use a multi-state MRAM cells as a memristive devices (memristors) in a single neuron. This involved using a structure similar to differential voltage summing amplifier, where memristors were used as a part of voltage dividers, thus defining weight of each input. Adding a transition function generator (for the design it was a sigmoid function) a single neuron was obtained. Finally all the components were designed at transistor level and then in a standard CMOS technology of UMC $180\,\mathrm{nm}$.

The electrical and switching parameters of the designed CMOS layout were extracted and combined with model of the multi-state MRAM cells. All the data allowed for a full simulation of the designed neural network. The network under simulation was programmed according to solution obtained during purely-software run (i.e. without simulation of electrical circuits). Then real simulations were run, during which the network recognized handwritten digits. Results were compared while using different numbers of MTJs connected per single memristive cell. Also an energy consumption of such device per operation was obtained during simulations.

A final conclusion was made, that such ANN is capable of performing operations with error rate close to ideal case (software calculations were taken as a baseline) and with energy consumption lower than similar solutions that were proposed prior to publishing of the research. What is more, as currently there are commercially available MTJ-CMOS circuits and fabrication

process is well developed such an architecture might be easily implemented. Such promising results pointed a direction towards examining MTJs as a potential building blocks for other types of neural networks. Particularly interesting area was the usage of interconnected MTJ-based oscillators working in RF regime, therefore research was done towards synchronization of such connected oscillators.

www.nature.com/scientificreports

scientific reports

OPEN

Multi-state MRAM cells for hardware neuromorphic computing

Piotr Rzeszut[1]✉, Jakub Chęciński[1], Ireneusz Brzozowski[1], Sławomir Ziętek[1], Witold Skowroński[1] & Tomasz Stobiecki[1,2]

Magnetic tunnel junctions (MTJ) have been successfully applied in various sensing application and digital information storage technologies. Currently, a number of new potential applications of MTJs are being actively studied, including high-frequency electronics, energy harvesting or random number generators. Recently, MTJs have been also proposed in designs of new platforms for unconventional or bio-inspired computing. In the current work, we present a complete hardware implementation design of a neural computing device that incorporates serially connected MTJs forming a multi-state memory cell can be used in a hardware implementation of a neural computing device. The main purpose of the multi-cell is the formation of quantized weights in the network, which can be programmed using the proposed electronic circuit. Multi-cells are connected to a CMOS-based summing amplifier and a sigmoid function generator, forming an artificial neuron. The operation of the designed network is tested using a recognition of hand-written digits in 20 × 20 pixels matrix and shows detection ratio comparable to the software algorithm, using weights stored in a multi-cell consisting of four MTJs or more. Moreover, the presented solution has better energy efficiency in terms of energy consumed per single image processing, as compared to a similar design.

Unconventional computing architectures such as artificial neural networks (ANN) have superior properties over conventional CMOS-based circuits in solving a number of computational problems, e.g., image or voice recognition, navigation, optimization and prediction[1–5]. As a concept, neural networks have been proved to be fast, flexible and energy-efficient. However, their digital implementation uses large amount of resources[6], which leads to high area needed to implement them. An alternative solution, opposite to the digital implementation, is to use analog-based circuits, where signals are represented as continuous voltage values rather than quantized bits[7–10]. In such implementations, a key component is a programmable resistive element, such as memristor[11], which can act as a weight in an artificial neuron. While using a solely digital implementation of a neural network may lead to high resource and energy consumption, using mixed digital and analog electronic circuits may enable more compact and energy-efficient solutions. In a number of the proposed analog ANN implementations, neuron behavior was mimicked by a resistive RAM (RRAM) element[12], which changed its resistance due to the conductor/insulator transition[7]. However, cells based on resistive or phase-change technology suffer from limited durability and may degrade over time and subsequent programming cycles[13]. On the contrary, spintronic elements such as memristors, nano-oscillators[14] or probabilistic bits[15], based on magnetic tunnel junctions (MTJs), which rely on magnetization switching or dynamics, do not have such endurance issues, are compatible with the CMOS technology and have been already shown to exhibit superior biomimetic properties[16]. In addition, recent theoretical works have predicted that neural networks are able to work efficiently not only with weights represented by real numbers, but also with binary or quantized values[17–19].

Recently, we have proposed a design of multi-state spin transfer torque magnetic random access memory (STT-MRAM) cells[20,21], which may be used in neuromorphic computing schemes as synapses[22–27] or as a standard multi-state memory unit. In this paper, we present a fully functional hardware implementation design of a neural network, which needs no additional components for operation, except for input and output devices. The design of a single synapse is based on multi-bit STT-MRAM cells forming quantized weights, interconnected with a minimal set of transistors forming amplifiers in the conventional CMOS technology. The entire network is made of neurons arranged in four layers. The operation principle of the proposed neural network is validated using handwritten digits recognition task utilizing MNIST[28] database. We show that the multi-cell consisting

[1]Institute of Electronics, AGH University of Science and Technology, Al. Mickiewicza 30, 30-059 Kraków, Poland. [2]Faculty of Physics and Applied Computer Science, AGH University of Science and Technology, Al. Mickiewicza 30, 30-059 Kraków, Poland. ✉email: piotrva@agh.edu.pl

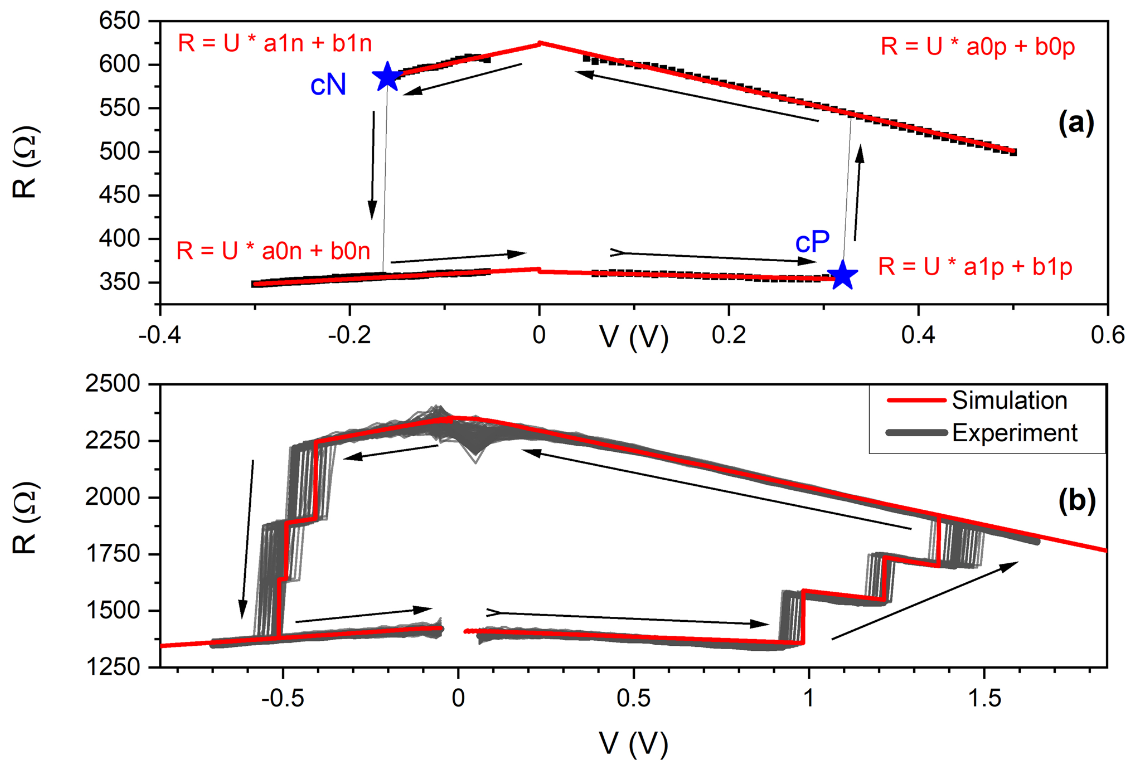

Figure 1. (**a**) Experimental $R(V)$ dependence (solid points) and the model consisting of four lines and two critical points (stars) presenting a single MTJ behaviour. (**b**) A representative simulation result of three serially-connected MTJs (solid line) together with a series of example measurements (gray-scale lines) of a two-bit multicell. Parameters of a single MTJ were used to model the multi-cell characteristics. Arrows indicate voltage sweep direction.

of four MTJs is sufficient for the network to achieve a recognition error rate below 3%, while providing better energy efficiency per operation than circuit presented by Zhang et. al.[29].

Experimental

Mulltibit-cell based artificial synapse. A key element of the design of the ANN is a spintronic memristor, which involves serially connected MTJs. Each of the MTJs may be characterized by a $R(V)$ curve (Fig. 1a), where two stable resistance states can be observed, as well as critical voltages (cN and cP), for which the switching occurs. By serially connecting N of such MTJs[20], a multi-state resistive element is obtained (Fig. 1b), for which $N + 1$ resistance states are observed.

The concept of the multi-cell was experimentally confirmed using up to seven MTJs connected in series. For the simulation of the network, we introduce a model of the multi-cell based on the following protocol. A typical $R(V)$ loop of an MTJ may be approximated using four linear functions (resistance vs. bias voltage dependence in each MTJ state) and two threshold points (switching voltages) as presented in Fig. 1a. In addition, in the case of a real MTJ the following parameters are related to each other: $a1n = -a1p = a1$, $b1n = b1p = b1$, $a0n = -a0p = a0$ and $b0n = b0p = b0$. Moreover, a current resistance state (high or low resistance) has to be included. Using such a model of the $R(V)$ curve allows also to calculate other transport curves, including $V(I)$. The proposed model corresponds to all MTJs that were investigated during the study. Parameters obtained from the experimental part, and further used in the simulation, are presented in Tab. 1. MTJs with perpendicular magnetic anisotropy were patterned as pillars 100 nm in diameter and interconnected using metalization layers and vias (Fig. 2).

The model was used to simulate serially connected MTJs and a representative comparison between simulation and experiment is presented in Fig. 1b. Moreover, simulations of up to seven MTJs were carried out, where, additionally, a spread of parameters was taken into account. This allowed for defining distribution of stable resistance states as well as voltages used for writing. The results of such simulation as well as representative experimental data are presented in Fig. 3.

Electronic neuron. After the analysis of the multi-cell, which may be used as a programmable resistor for performing weighted sum operation for many input voltages, we turn to the artificial neuron design. A sche-

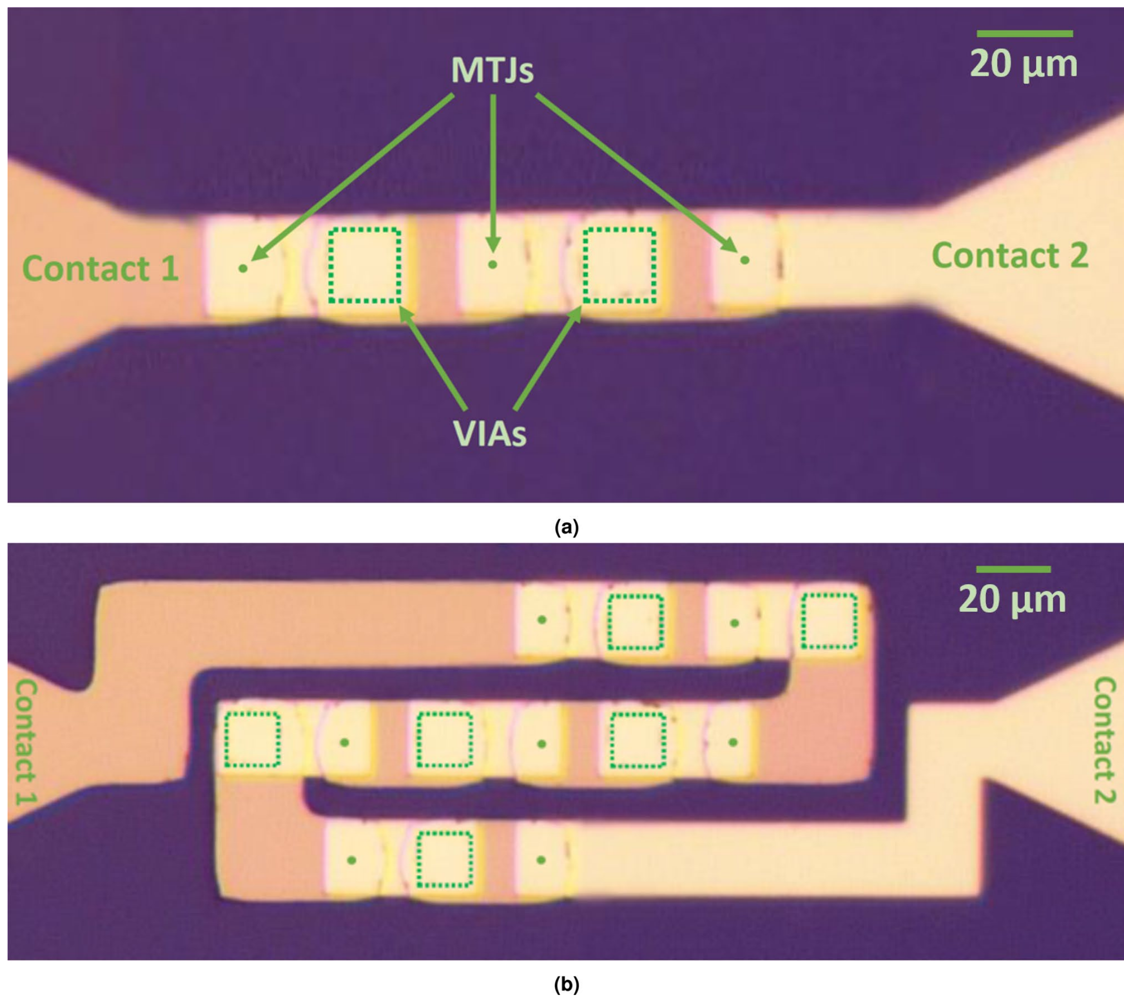

Figure 2. Microimage of the experimental setup: (**a**) three and (**b**) seven serially connected MTJs (dots) with vias (squares) marked.

Param.	Unit	μ	σ
a1	A^{-1}	−310	3
b1	Ω	665	12
a0	A^{-1}	−30	3
b0	Ω	360	12
cN	A	−3.1e−4	1.5e−5
cP	A	8.0e−4	1.5e−5
TMR	%	84	–

Table 1. Expected values and standard deviation of parameters obtained from experiment.

matic diagram of the proposed neuron is presented in Fig. 4. The circuit is powered by a bipolar power supply, where inputs and output (V_{INm}, V_{OUT}) are provided as bipolar analog signals. To enable positive and negative weights, each of the signal inputs uses a pair of programmable MTJ multi-cells (M_{mP} and M_{mN}). In the case when the multi-cell resistances meet the condition $M_{mP} < M_{mN}$, a positive weight is achieved, whereas for the case of $M_{mP} > M_{mN}$ a negative weight value is obtained. An alternative design with multiple MTJs connected in series with a separate select transistors has been proposed recently in Ref.[30]. For equal multi-cell resistances, a

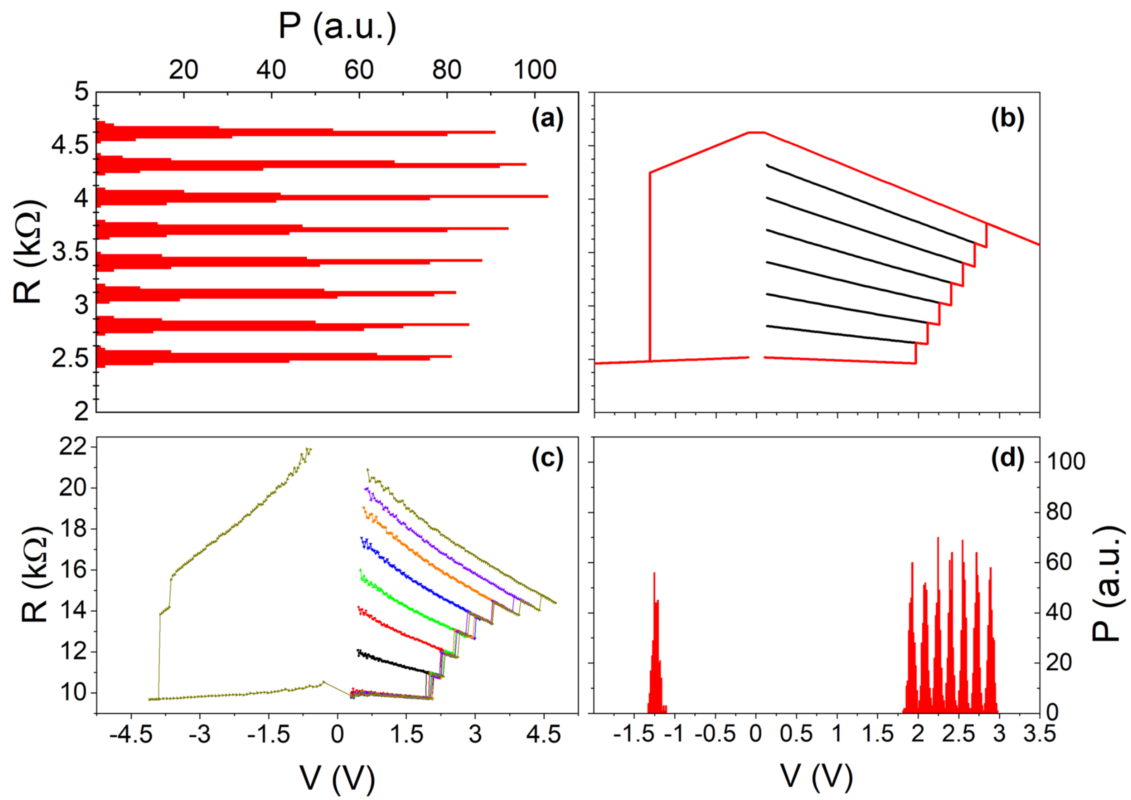

Figure 3. Simulation and experimental results for seven serially connected MTJs with a given parameter spread. (**a**) Spread of readout resistances for the simulation. (**b**) Representative write-read-erase curves. Red line represents full write-read-erase cycle, while black ones represent write-read cycles while programming subsequent values. (**c**) Experimental data for seven serially connected MTJs. MTJs in this case come from another batch, characterized by higher RA product of around 20Ø*mega* µm^2, which results in approximately three times higher resistance of the multicell and slightly higher switching voltages. (**d**) Spread of all write voltages for the simulation.

zero weight is obtained, which is equivalent to the situation when an input is disconnected from the synapse. The resistive summing circuit architecture is being used in order to implement an addition operation while reducing the footprint of the synapse. A differential amplifier converts differential voltage to a single bipolar signal, which is transformed using a non-linear sigmoid function. This voltage may be used as the input of the next synapse, or as the output of the network. Additionally, to provide a constant bias, a standard input with constant voltage may be used, where the level of this constant bias is determined in the same way as weights for other functional inputs.

Neural network circuit. The electrical circuit implementing the proposed neural network was designed in a standard CMOS technology—UMC 180 nm. To program the demanded resistance of seven serially connected MTJs, a voltage of about 3.25 V is needed, so input/output (I/O) 3.3 V transistors were used to design a circuit for MTJs programming purpose, while for other circuits, a standard 1.8 V transistors were used. An individual neuron circuit is composed of three parts. At the input, two resistive networks consisting of memristors implement a multiplication of input voltages by coefficients and summing of these products (Fig. 4a). Next, the obtained voltages are subtracted and amplified to the demanded value in a differential amplifier (Fig. 4b). Voltage followers are used to separate stages of the circuit and eliminate unwanted loading (Fig. 4d). Finally, the third part is a sigmoid function block, which implements the activation function (Fig. 4c). It is based on an inverter and has negative transfer characteristic, thus appropriate polarizations of signals are required.

The differential voltage V_d generated by the divider network (Fig. 4a) connected to a pair of voltage followers (Fig. 4d) can be expressed as:

$$V_d = -\frac{1}{G_{sum}}\left(\sum_{i=1}^{m} V_{INi}(G_{iP} - G_{iN})\right),$$

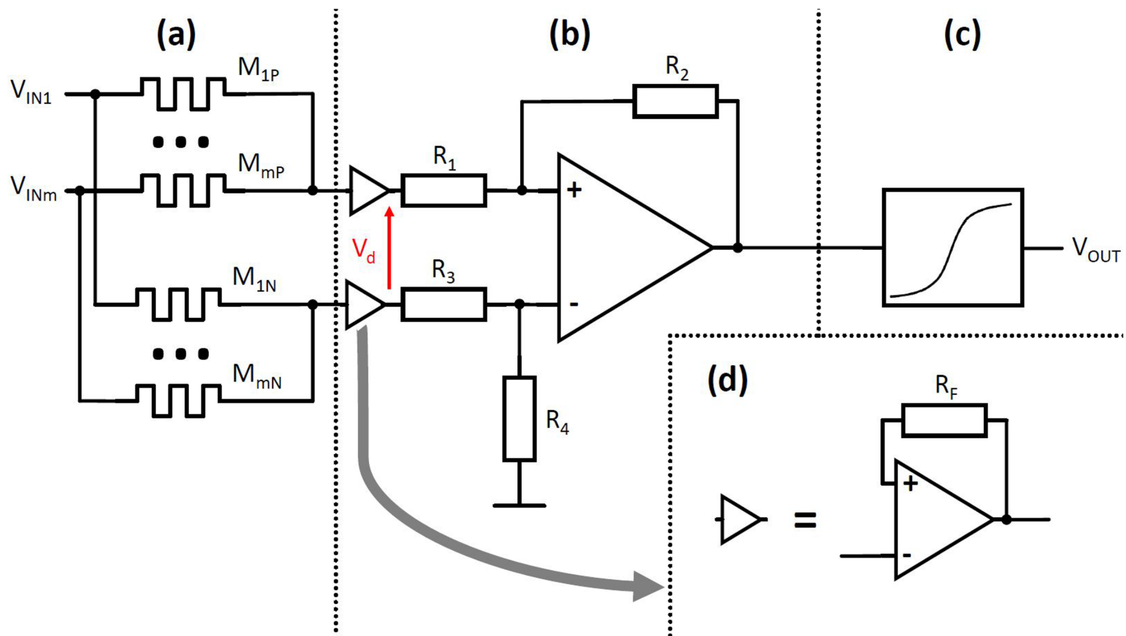

Figure 4. The proposed neuron design with multi-cells. The circuit consists of (**a**) a set of memristors serving as a quantized weight, (**b**) a differential amplifier with voltage followers (**d**) at input and (**c**) a sigmoid function block.

where:

$$G_{iX} = \frac{1}{M_{iX}}$$

$$G_{sum} = m * G_{ave} = m * \frac{G_{min} + G_{max}}{2}$$

It can be assumed that sums of all memristors' conductances in both positive and negative branch are nearly equal, and can be well approximated by the average of minimum (G_{min}) and maximum (G_{max}) conductances of memristors used, multiplied by the number of inputs (m) in the neuron.

Results

To evaluate the performance of the multi-bit MTJ cell-based ANN, a set of classification tasks using the MNIST dataset of handwritten digits (Fig.5a) was prepared. The conceptual architecture used for the network is shown in Fig. 5b and consists of the input layer, two hidden layers containing N neurons each and the output layer. A benchmark software network was trained using the standard scaled conjugate gradient method and cross-entropy error metrics, with *tanh* activation function for every layer except the last one, where the *softmax* function was used. Then, its performance was evaluated on a testing subset that has been drawn randomly from the input data and has not participated in training. This procedure was repeated 50 times in total, with training and testing subsets being redrawn each time, leading to an average error estimate for each network size.

Having established the performance of the benchmark software network, the evaluation of our MTJ-based design was performed. The original float-accuracy weights between different neurons were replaced by their discrete versions corresponding to our multi-state MTJ synapses. The new weights were calculated using simulated conductance data (as described in Sec. "Multibit-cell based artificial synapse") and rescaled by tuning amplifier gains to match the desired value range for the neurons. Then, the performance of the network was re-evaluated on the testing data subset. The results are presented in Fig. 5c. It can be seen that, as long as the number of MTJs used per multi-state cell exceeds three, the performance of the MTJ-based solution is comparable to the original software version, with differences being only incremental in character. Due to a relatively shallow structure of our network, the total number of individual MTJ elements necessary to perform the calculation is thus remarkably low and ranges from around 200 to around 700, depending on the assumed tolerance for error. This is one order of magnitude lower than the number previously reported for quantized neural networks based on MTJs with comparable performance[19].

The neural network shown in Fig. 5b, using 7 MTJs per memristor, was also described and simulated electrically in Hspice for the same data as computer simulations mentioned above, assuming 7 MTJs per memristor. Input voltages (with maximum amplitude of 0.2 V) corresponding to hand written MNIST digits were changed

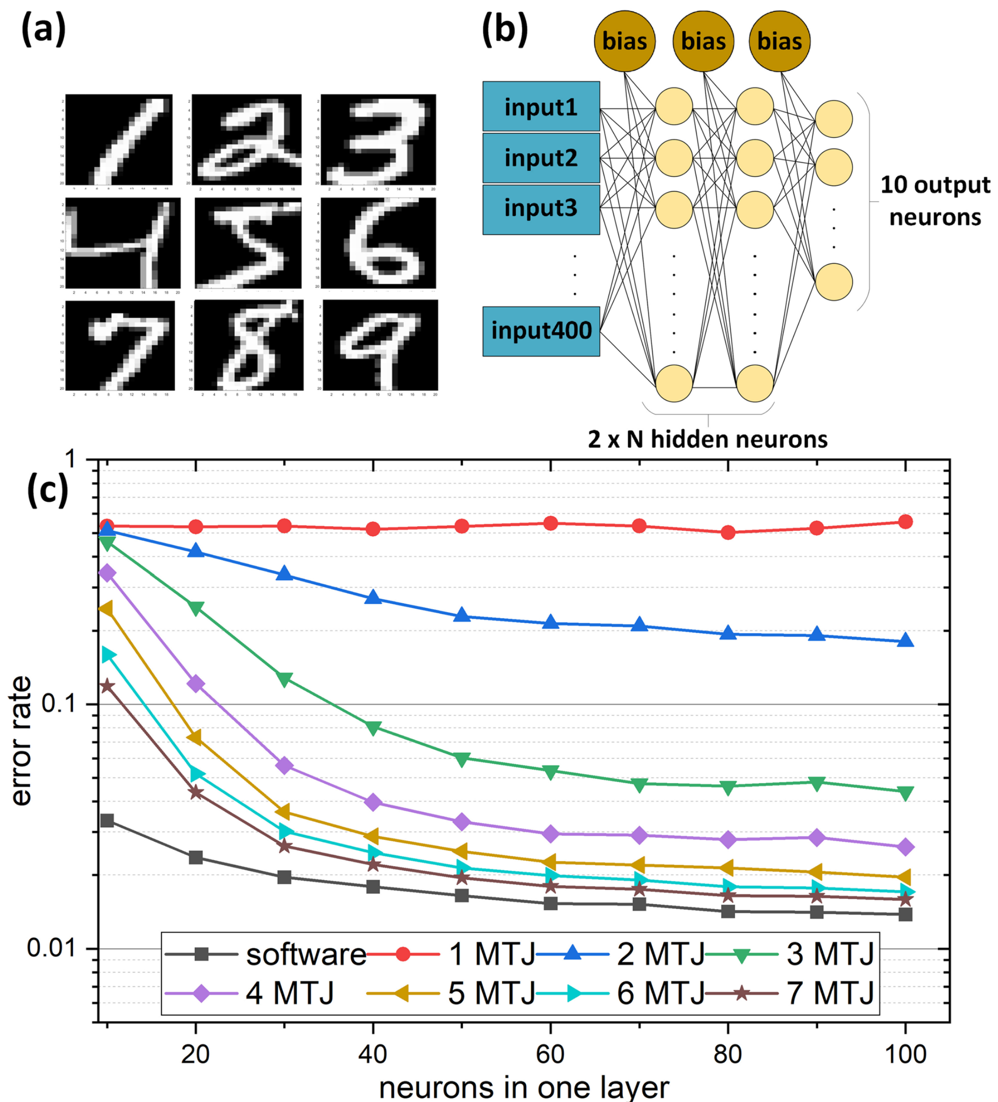

Figure 5. Simulated neural network based on multi-bit MRAM cells. Handwritten digits from MNIST database (**a**) are recognized by a standard neural network with architecture shown in (**b**), where black lines represent network weights and yellow circles represent individual neurons. After training, weights calculated by software are replaced by discretized values corresponding to 1–7 serial MTJs MRAM cells, which affects the network performance (**c**).

to a next image every 4 µs. The circuit gave the same results as theoretical calculations—for a given subset of cases the same error rate was achieved. The circuit had a latency of approximately 1 µs and to process one picture, only 37.4 pJ of energy were needed. It is therefore a significant improvement compared to the work by Zhang et. al.[29], where processing of a 10 by 10 pixel area (4 times smaller area than our 20 by 20 pixel images) consumed 194 pJ. The power consumption of our network could be further decreased, and speed could be increased at the expense of the output voltage. Also, the total resistance of each synapse might be increased by connecting additional resistances as well as by careful optimization in the MTJ structure such as using devices with higher RA product[31] and by further miniaturization of the MTJ pillar size below 100 nm in diameter[32]. However, it could also lead to deterioration of the reliability of the ANN.

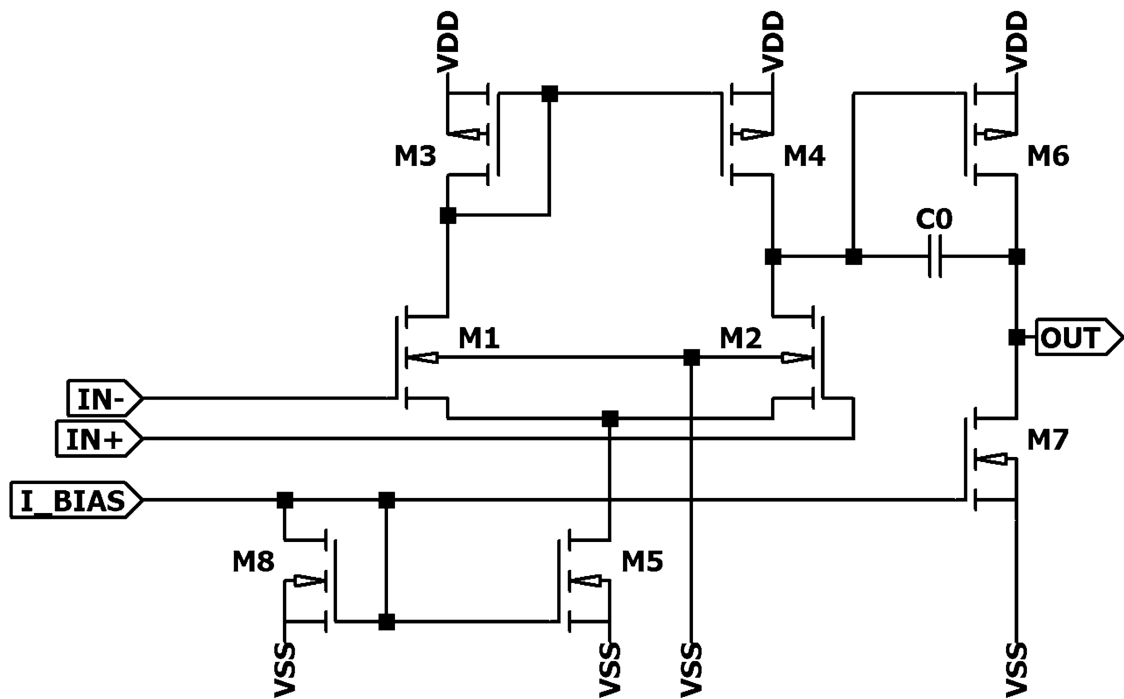

Figure 6. Operational amplifier circuit used in the design.

Discussion

The presented architecture of full hardware artificial neural network proves to be an effective way of performing neuromorphic computing. Compared to other solutions, it utilizes standard MTJs that are compatible with STT-MRAM technology, which has been recently developed for mass production. Additionally, MTJs in such application are very stable over time and they exhibit high endurance in terms of reprogramming, comparing to low-energy barrier MTJs used in probabilistic computing. To validate the circuit, the artificial CMOS-based neuron was designed, consisting of multi-cell based synapses, differential amplifiers and sigmoid function generator. It was shown that the quantized-weight approach enables the development of a functional artificial neural network, capable of solving recognition problems with accuracy level similar to the benchmark software model. Moreover, the electronic simulations additionally proved low latency of the operation of the order of µs as well as low energy consumption per recognized picture.

Methods

Circuit details. The operational amplifier, presented in Fig. 6 was designed as a two stage circuit consisting of a differential pair M1, M2 with a current mirror load M3, M4 biased by M5 with a current of 1 µA. The output stage M6, M7 provided appropriate amplification and output current. The total current consumed by the operational amplifier is about 12 µA and amplification with an open loop of around 74 dB. Dimensions of transistors were chosen in such a way to obtain the smallest area possible while meeting the required electrical parameters (width of M1 and M2 is 0.7 µm, M3 and M4 is 0.45 µm, M5 and M8 is 0.96 µm, M6 is 7.48 µm, and M7 is 7 µm, capacitance of C0 is 100fF).

The final stage of the neuron is a circuit, which performs activation functions and has negative hyperbolic tangent transfer characteristic, presented in Fig. 7b. It is designed as a modified inverter, which has voltage-to-voltage transfer in contrast to other solutions, such as resistive-type sigmoid[33]. Transistors M2 and M3 work as resistors, moving operating point of transistors M0 and M1 to the linear region. Finally, the circuit implements the transfer characteristic shown in Fig. 7a. Minimum length of channels were used (180 nm, except for M3,

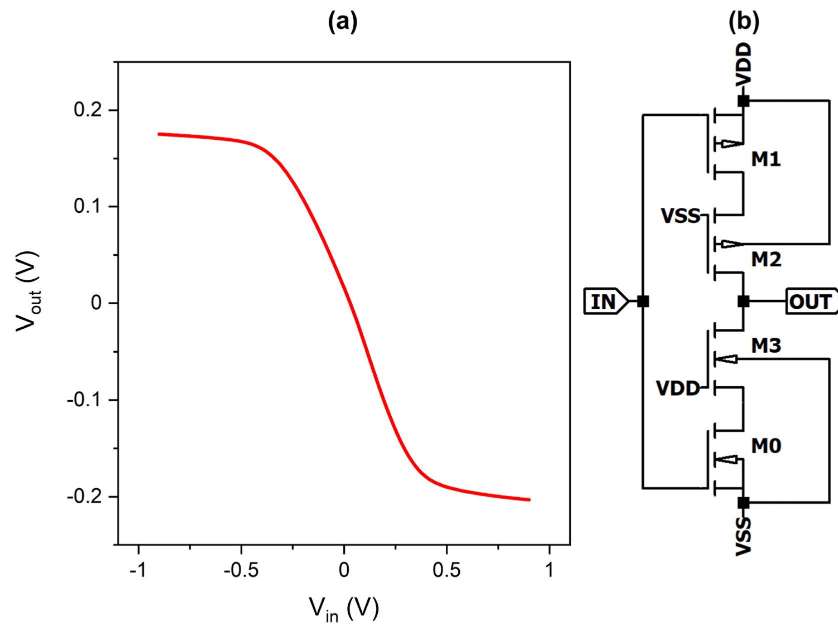

Figure 7. (**a**) A transfer function of a sigmoid-generating inverter implemented by (**b**) the proposed inverter circuit.

which uses 750nm), while their width was chosen to obtain required characteristics and output current necessary to drive the next stage. Therefore, the width of M0 and M3 is 60 μm, M1 is 228 μm, and M2 is 56 μm.

Using Cadence Virtuoso, layouts for amplifier and sigmoid were designed. Dimensions of each circuits are 17.1 × 17.4 μm for op-amp and 17.5 × 32 μm for sigmoid. Netlists with parasitic elements were extracted for further simulations performed in Hspice.

Programming of the synapse. The important part of the design involved a circuit for memristors programming. The overview of the programming circuit is presented in Fig. 8. The switches are controlled from the digital circuit in such a way that the memristor to be programmed is connected with one terminal to the programming voltage input and the other terminal to the ground. After the selected elements are connected, the required voltage value is applied to the programming input in order to program the chosen memristors. Those elements that are not programmed with a given voltage are disconnected from the programming input. In the next cycle, another set of memristors is connected for programming and another voltage is applied. In such solution, all memristors may be programmed in a number of cycles corresponding to the number of stable quantized states of used memristors (e.g., for 7 MTJs per memristor the programming may be completed in only 8 cycles; if the programming voltage spread is too high, additional cycles might be introduced or adaptive programing scheme can be used, however state-of-the-art MTJ industrial fabrication technology can meet requirements with accepted write voltage distribution[34]). The purpose of the digital control circuits to connect the desired components to the programming voltage and ground lines or to switch to normal operation. The state of the switches is stored in serially connected flip-flops. Therefore, additional AND gates controlled by the "enable" signal are used to disconnect all memristors while entering information about elements for programming. Then, after setting the appropriate programming voltage, the enable signal goes high for the duration of programming. The flip-flop and the AND gate are placed as close to the switches as possible, to save connection length. Digital components placed close to the sensitive analog circuit do not have influence on them, because during the operation of the ANN the digital circuitry is inactive, remaining in a static state (no clock signal) while providing the connection of memristors to the analog circuit.

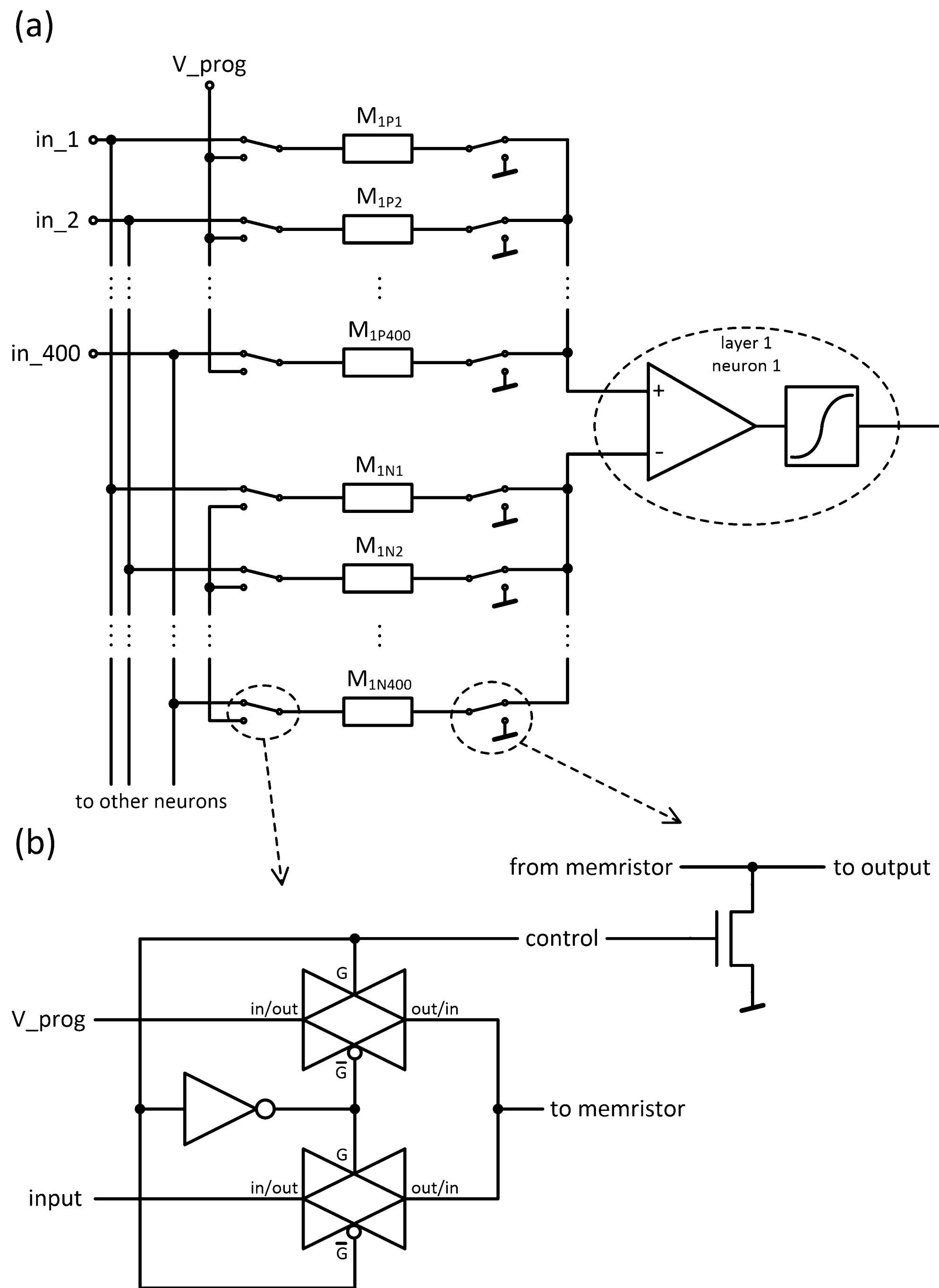

Figure 8. (**a**) Schematic of connection of programming switches and (**b**) the design of the programming switches.

Received: 3 November 2021; Accepted: 18 April 2022
Published online: 03 May 2022

References

1. Fu, J., Zheng, H. & Mei, T. Look closer to see better: Recurrent attention convolutional neural network for fine-grained image recognition. In *Proceedings of the IEEE conference on computer vision and pattern recognition*, 4438–4446 (2017).
2. Venayagamoorthy, G. K., Moonasar, V. & Sandrasegaran, K. Voice recognition using neural networks. In *Proceedings of the 1998 South African Symposium on Communications and Signal Processing-COMSIG'98 (Cat. No. 98EX214)*, 29–32 (IEEE, 1998).
3. Zhang, Y., Li, S. & Guo, H. A type of biased consensus-based distributed neural network for path planning. *Nonlinear Dyn.* **89**, 1803–1815 (2017).
4. Muralitharan, K., Sakthivel, R. & Vishnuvarthan, R. Neural network based optimization approach for energy demand prediction in smart grid. *Neurocomputing* **273**, 199–208 (2018).
5. Abhishek, K., Singh, M., Ghosh, S. & Anand, A. Weather forecasting model using artificial neural network. *Proc. Technol.* **4**, 311–318 (2012).
6. Nurvitadhi, E. *et al.* Accelerating binarized neural networks: Comparison of FPGA, CPU, GPU, and ASIC. In *2016 International Conference on Field-Programmable Technology (FPT)*, 77–84 (IEEE, 2016).
7. Yao, P. *et al.* Fully hardware-implemented memristor convolutional neural network. *Nature* **577**, 641–646 (2020).
8. Yao, P. *et al.* Face classification using electronic synapses. *Nat. Commun.* **8**, 1–8 (2017).
9. Yu, S. Neuro-inspired computing with emerging nonvolatile memorys. *Proc. IEEE* **106**, 260–285 (2018).
10. Ambrogio, S. *et al.* Equivalent-accuracy accelerated neural-network training using analogue memory. *Nature* **558**, 60–67 (2018).
11. Strukov, D. B., Snider, G. S., Stewart, D. R. & Williams, R. S. The missing memristor found. *Nature* **453**, 80–83 (2008).
12. Burr, G. W. et al. Neuromorphic computing using non-volatile memory. *Adv. Phys. X* **2**, 89–124. https://doi.org/10.1080/23746149.2016.1259585 (2017).
13. Wu, Q. *et al.* Improvement of durability and switching speed by incorporating nanocrystals in the HfOx based resistive random access memory devices. *Appl. Phys. Lett.* **113**, 023105 (2018).
14. Grollier, J., Querlioz, D. & Stiles, M. D. Spintronic nanodevices for bioinspired computing. *Proc. IEEE* **104**, 2024–2039. https://doi.org/10.1109/JPROC.2016.2597152 (2016).
15. Borders, W. A. *et al.* Integer factorization using stochastic magnetic tunnel junctions. *Nature* **573**, 390–393. https://doi.org/10.1038/s41586-019-1557-9 (2019).
16. Romera, M. *et al.* Vowel recognition with four coupled spin-torque nano-oscillators. *Nature* **563**, 230–234. https://doi.org/10.1038/s41586-018-0632-y (2018).
17. Moons, B., Goetschalckx, K., Van Berckelaer, N. & Verhelst, M. Minimum energy quantized neural networks. In *2017 51st Asilomar Conference on Signals, Systems, and Computers*, 1921–1925 (IEEE, 2017).
18. Hubara, I., Courbariaux, M., Soudry, D., El-Yaniv, R. & Bengio, Y. Quantized neural networks: Training neural networks with low precision weights and activations. *J. Mach. Learn. Res.* **18**, 6869–6898 (2017).
19. Toledo, T. G., Perach, B., Soudry, D. & Kvatinsky, S. MTJ-Based Hardware Synapse Design for Quantized Deep Neural Networks. *arXiv preprint*arXiv:1912.12636 *(2019).*
20. Rzeszut, P., Skowroński, W., Ziętek, S., Wrona, J. & Stobiecki, T. Multi-bit MRAM storage cells utilizing serially connected perpendicular magnetic tunnel junctions. *J. Appl. Phys.* **125**, 223907 (2019).
21. Raymenants, E. *et al.* Chain of magnetic tunnel junctions as a spintronic memristor. *J. Appl. Phys.* **124**, 152116 (2018).
22. Zhang, D. *et al.* All spin artificial neural networks based on compound spintronic synapse and neuron. *IEEE Trans. Biomed. Circuits Syst.* **10**, 828–836 (2016).
23. Torrejon, J. *et al.* Neuromorphic computing with nanoscale spintronic oscillators. *Nature* **547**, 428 (2017).
24. Lequeux, S. *et al.* A magnetic synapse: Multilevel spin-torque memristor with perpendicular anisotropy. *Sci. Rep.* **6**, 31510 (2016).
25. Sung, C., Hwang, H. & Yoo, I. K. Perspective: A review on memristive hardware for neuromorphic computation. *J. Appl. Phys.* **124**, 151903 (2018).
26. Sulymenko, O. *et al.* Ultra-fast logic devices using artificial "neurons" based on antiferromagnetic pulse generators. *J. Appl. Phys.* **124**, 152115 (2018).
27. Fukami, S. & Ohno, H. Perspective: Spintronic synapse for artificial neural network. *J. Appl. Phys.* **124**, 151904 (2018).
28. Deng, L. The mnist database of handwritten digit images for machine learning research [best of the web]. *IEEE Signal Process. Mag.* **29**, 141–142 (2012).
29. Zhang, D., Hou, Y., Zeng, L. & Zhao, W. Hardware acceleration implementation of sparse coding algorithm with spintronic devices. *IEEE Trans. Nanotechnol.* **18**, 518–531 (2019).
30. Amirany, A., Moaiyeri, M. H. & Jafari, K. Nonvolatile associative memory design based on spintronic synapses and cntfet neurons. *IEEE Trans. Emerg. Top. Comput.* 1–1. https://doi.org/10.1109/TETC.2020.3026179 (2020).
31. Mihajlović, G. *et al.* Origin of the resistance-area-product dependence of spin-transfer-torque switching in perpendicular magnetic random-access memory cells. *Phys. Rev. Appl.* **13**, 024004 (2020).
32. Watanabe, K., Jinnai, B., Fukami, S., Sato, H. & Ohno, H. Shape anisotropy revisited in single-digit nanometer magnetic tunnel junctions. *Nat. Commun.* **9**, 1–6 (2018).
33. Khodabandehloo, G., Mirhassani, M. & Ahmadi, M. Analog implementation of a novel resistive-type sigmoidal neuron. *IEEE Trans. Very Large Scale Integr. VLSI Syst.* **20**, 750–754. https://doi.org/10.1109/TVLSI.2011.2109404 (2012).
34. Alzate, J. et al. 2 mb array-level demonstration of stt-mram process and performance towards l4 cache applications. In *2019 IEEE International Electron Devices Meeting (IEDM)*, 2–4 (IEEE, 2019).

Acknowledgements

We would like to thank Dr J. Wrona from Singulus Technologies AG for MTJ multilayer deposition. Scientific work funded from budgetary funds for science in 2017-2018, as a research project under the "Diamond Grant" program (Grant No. 0048/DIA/2017/46). W.S. acknowledges support by the Polish National Center for Research and Development grant No.LIDER/467/L-6/14/NCBR/2015. T.S. acknowledges the SPINORBITRONICS grant No. 2016/23/B/ST3/01430. The nano-fabrication process was performed at Academic Centre for Materials and Nanotechnology (ACMiN) of AGH University of Science and Technology. Numerical calculations were supported by PL-GRID infrastructure. Research project partly supported by program "Excellence initiative – research university" for the AGH University of Science and Technology.

Author contributions

P.R. conducted nanofabrication and electrical characterization of the samples and proposed general network structure, J.Ch. conducted software simulations of the network and network training. I.B. designed and simulated

CMOS-based circuit, S.Z. and W.S. provided expertise in terms of MTJs and neural networks, T.S. provided literature digest and major suggestions on manuscript text. All authors reviewed the manuscript.

Competing interests

The authors declare no competing interests.

Additional information

Correspondence and requests for materials should be addressed to P.R.

Reprints and permissions information is available at www.nature.com/reprints.

Publisher's note Springer Nature remains neutral with regard to jurisdictional claims in published maps and institutional affiliations.

Open Access This article is licensed under a Creative Commons Attribution 4.0 International License, which permits use, sharing, adaptation, distribution and reproduction in any medium or format, as long as you give appropriate credit to the original author(s) and the source, provide a link to the Creative Commons licence, and indicate if changes were made. The images or other third party material in this article are included in the article's Creative Commons licence, unless indicated otherwise in a credit line to the material. If material is not included in the article's Creative Commons licence and your intended use is not permitted by statutory regulation or exceeds the permitted use, you will need to obtain permission directly from the copyright holder. To view a copy of this licence, visit http://creativecommons.org/licenses/by/4.0/.

© The Author(s) 2022

6. Synchronization of STO oscillations

Previous research confirmed that interconnected MTJs might be efficiently used a building blocks in ANNs by providing means to define synapses' weights. As types of ANN different than voltage feed-forward were also proven to be effective a step forward this direction was decided to be made. It was noted that merging solutions use wide range of oscillators working in RF regime, therefore some experimental and simulation work was done on topic of synchronization of MTJ-based spin torque oscillators.

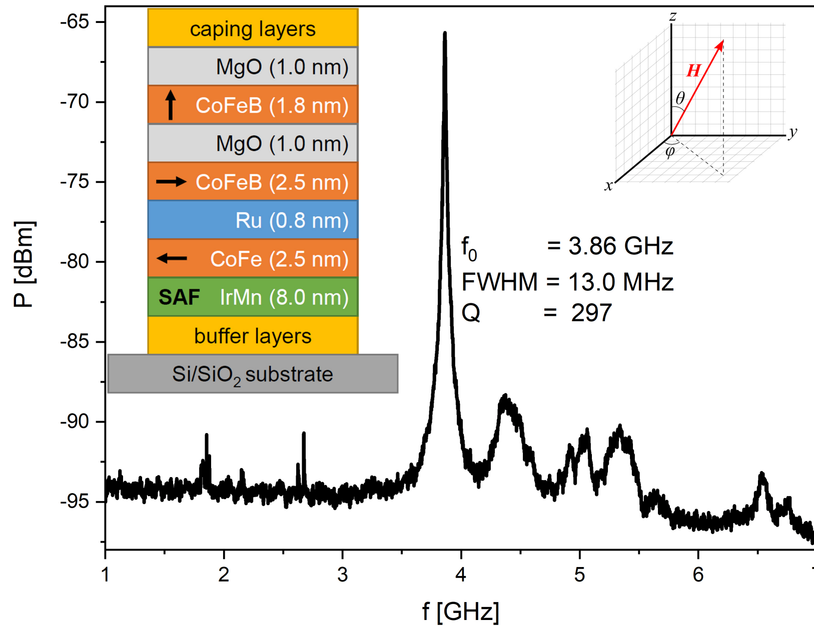

Figure 6.1: A representative signal generated by an STO for conditions of $H = 71.6\,\mathrm{kA/m}$ (at spherical angles of $\theta = 31^\circ$ relative to the normal surface vector and in-plane $\phi = 0^\circ$ measured from the positive x axis), $I = 1.88\,\mathrm{mA}$. Inset left: important layers of the STO, RL with in-plane magnetic anisotropy, FL with out-of-plane anisotropy, marked with black arrows, RL pinned with synthetic antyferromagnet (SAF). Inset right: coordinate system.

The MTJs used for the experiments were fabricated with a different multi-layer stack than these used for multi-state MRAM cells. For the efficient oscillation a configuration with bottom (reference) layer with in-plane anisotropy and top (free) layer with out-of-plane anisotropy was selected, as such construction allows for generation of higher spin torque. A representative oscillations generated by such element are presented in Fig. 6.1, together with important parts

of the layer structure as an inset. Such an oscillator has a very limited power as well as low Q factor. In order to improve these parameters synchronization to externally provided signal[84, 85] or to signal from other STOs[56] might be used.

Initially experiments were conducted to check if the Spin Torque Oscillators (STO) are possible to get synchronized to an external RF signal generated using an RF generator. An obvious solution to use directly same frequency proved to be difficult in actual measurement, as overall separation between the RF generator and measurement equipment in the best setup that was available to use was too low. This resulted in signal from the generator saturating input of the spectrum analyser and leading to inability to observe output of the STO under test.

As a solution, during a visit to AIST Japan in Tsukuba, a measurement technique was proposed to use a generator frequency exactly two times higher then desired oscillation frequency. With such approach a different synchronization scheme is taking part, but an output of the MTJ can be clearly observed, as it is separated from the signal from RF generator in frequency regime. Resulting observation was that MTJ is able to get synchronized to such a signal and this finds reflection in observable decrease of Full Width Half Maximum (FWHM) of the signal (from average value of $12.5\,\mathrm{MHz}$ for a free-running oscillations to less than $2.5\,\mathrm{MHz}$ when in synchronization) as well as a frequency shift from a free-running frequency. It is to note that synchronization conditions were very narrow.

The last experiment involved observing two serially connected (head-to-tail) STOs oscillation while varying external magnetic field. As it was previously stated, conditions for synchronization were not wide, so it was excepted, that the effect would be hard to notice. Also synchronization mechanism for two interconnected MTJs is excepted to be different, so a wide range of external parameters were tested: magnetic field vector orientation related to sample surface, current density and direction. This experimental part was one of the hardest, as in order to get any conclusive results, large amount of data had to been collected and then precisely examined. Finally it was discovered, that indeed a synchronization (and also desynchronization for other conditions) might be observed.

All the results were also compared against numerical simulations, carried out in cooperation with co-authors of the paper. This confirmed, that the theoretical model and tool-set (CMTJ) prepared by them is accurate enough to simulate interconnected MTJs acting as STOs in RF regime. To conclude the research it is important to note, that synchronization and desynchronization effects observed, both can have an application in future devices, such as reservoir computing, neural networks and other emerging computing schemes[86, 87]. This leads to need of further investigation of the phenomena to the point, where it can be easily reproduced and controlled in more precise way. The ideas include, but are not limited to having current lines above individual interconnected STOs to finely tune their behaviour using Oersted field or to inject other RF signals into the system.

Towards mutual synchronization of serially connected Spin Torque Oscillators based on magnetic tunnel junctions

Piotr Rzeszut[a],* Jakub Mojsiejuk[a],† Witold Skowroński[a],‡ Sumito Tsunegi[b], Hitoshi Kubota[b], and Shinji Yuasa[b]
a) AGH University of Science and Technology, Institute of Electronics,
Al. Mickiewicza 30, 30-059 Kraków, Poland
b) National Institute of Advanced Industrial Science and Technology,
Spintronics Research Center,
Tsukuba, Ibaraki 305-8568, Japan

(Dated: June 22, 2023)

arXiv:2306.11608v2 [physics.app-ph] 21 Jun 2023

Multiple neuromorphic applications require the tuning of two or more devices to a common signal. Various types of neuromorphic computation can be realized using spintronic oscillators, where the DC current induces magnetization precession, which turns into an AC voltage generator. However, in spintronics, synchronization of two oscillators using a DC signal is still a challenging problem because it requires a certain degree of similarity between devices that are to be synchronized, which may be difficult to achieve due to device parameter distribution during the fabrication process. In this work, we present experimental results on the mechanisms of synchronization of spin-torque oscillators. Devices are based on magnetic tunnel junction with a perpendicularly magnetized free layer and take advantage of a uniform magnetization precession in the presence of the magnetic field and a DC bias. By using an external microwave source, we show the optimal condition for the synchronization of the magnetic tunnel junctions. Finally, we present results on the in-series connection of two junctions and discuss the possible path towards improving oscillation power and linewidth. In addition, using numerical simulations of the coupled oscillators model, we aim to reproduce the conditions of the experiments and determine the tolerance for achieving synchronization.

I. INTRODUCTION

In recent years, neuromorphic computing concepts have gained rapid traction in multiple disciplines [1], with a promising mix of low-power and low-latency hardware-embedded algorithms. Exciting works using so-called vortex nanooscillators such as those by Romera et al.[2, 3], Torrejon et al.[4] or Tsenugi et al.[5] have also put neuromorphic concepts on the spintronics roadmap. Similar concepts of neuromorphic vowel recognition have been accomplished by spin-Hall oscillators based on nanoconstriction arrays [6]. More recently, both experimental and theoretical explorations [7] indicate that spin Hall nano oscillators can be used to construct phase-binarised Ising machines and solve some optimization problems at a potentially lower power consumption than quantum computers. Indeed, prevailing approaches have involved some type of nanooscillator where the synchronization mechanism is achieved by a combination of dipole coupling and injection locking. However, there have been some attempts to achieve coupling based on electric effects rather than magnetic ones, as explored in the work by Taniguchi [8]. Recently, Sharma et al. [9] have achieved a synchronized oscillation of up to four serially or parallel connected in-plane magnetized magnetic tunnel junctions (MTJs). Experimentally, the magnetic isolation of two devices is achieved simply by placing them further apart, so that the dipole interaction between them can be neglected (the dipole interaction decreases with distance as d^3). This usually requires an inter-device spacing of the order of μm. In this work we present an experimental study of the spin torque oscillators (STOs) realized by a magnetic tunnel junction with mixed magnetic anisotropies. To maximize the spin transfer torque acting on the free layer, an MTJ with an in-plane magnetized reference layer and a perpendicularly magnetized free layer is used. At optimal magnetic field orientation and DC bias conditions, this MTJ operates as an STO at radio frequencies with an average Q factor of 400. Using an external reference signal, we show the locking range of the STO to the half of the reference frequency, and present a study of the power dependence of in that locking range. The results of the synchronization with two MTJs connected in-series is also shown. The experiments are reproduced with numerical simulations based on coupled MTJs excited via the spin-transfer torque (STT). The Bayesian optimization allowed us to determine the magnetic parameters of the MTJ. Finally, we include a parametric study as a function of the coupling coefficient and magnetic parameters.

* piotrva@agh.edu.pl
† mojsieju@agh.edu.pl
‡ skowron@agh.edu.pl

II. EXPERIMENTAL

A. Fabrication of MTJs

The MTJ multilayer structure is the following: *Si* /SiO_2 / *CMP* / (4) *Ru* / (6) *IrMn* / (2.5) *CoFe* / (0.8) *Ru* / (2.5) *CoFeB* / (1) *MgO* / (1.8) *CoFeB* / (1) *MgO* / (3) *Ru* / (5) *Ta* / (2) *Ru* / (3) *Pt* (thickness in nm). The bottom CoFeB reference layer is in-plane magnetized and is coupled to the CoFe layer, pinned to the IrMn antiferromagnet. The top CoFeB layer is characterized by a perpendicular magnetic anisotropy owing to the significant double MgO interface anisotropy contribution. The thickness of the MgO tunnel barrier corresponds to

the RA product of 3.6 Ω µm^2.

Mixed-match three-step lithography using electron and optical lithography is performed including ion beam etching and the lift-off process to fabricate serially connected MTJs with the necessary measurement contacts (Fig. 1). The nominal dimensions of all MTJs are 130 nm in diameter, which are encapsulated in Al2O3. The resistance of a single MTJ is around67 Ω. Detailed magnetic characterization and fabrication process is described in our earlier work [10].

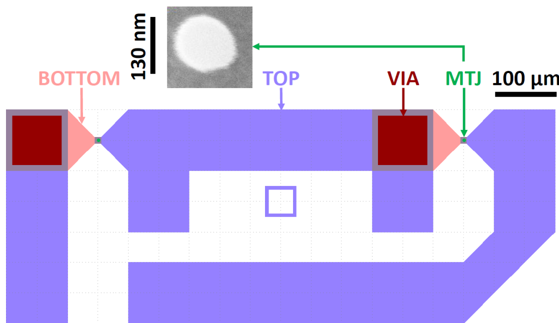

FIG. 1: Lithography mask of a single device consisting of two serially (head-to-tail) connected MTJs. Pink colour denotes a bottom electrode, red the via, violet represents the top electrode. MTJs are not visible at this scale and are fabricated on thin intersections of top and bottom electrode.

B. Measurement setup

Schematic of the measurement setup used in the experiment is presented in Fig. 2. The setup consists of an radio-frequency (RF) generator (Agilent E8257D) connected to the first symmetric port of the RP power splitter (Mini-Circuits ZN2PD2-14W-S+). The second symmetric port of the splitter is connected to the RF power amplifier (Mini-Circuits ZVA-213-S +) powered by a 12V DC power supply. The amplified signal is fed into an RF spectrum analyzer (Agilent N9030A). The combined (main) port of the power splitter is connected to an RF port of a bias tee (Mini-Circuits ZX86-12G-S+). An DC port of the bias tee is connected to the sourcemeter (Keysight B2912A). RF port of the bias tee connects to an RF probe (Picoprobe) that allows for the connection of the sample. When the RF generator was not in use it was replaced with the 50 Ω RF terminator.

The measurement system was completed with a magnetic field generator set-up, consisting of fixed electromagnet (GMW model 3472-70) powered with a current source (Kepco power supply BOP 50-20MG) and a gaussmeter (Lakeshore DSP-475) for magnetic field readout during electromagnet calibration. To change the orientation of the magnetic field vector relative to the sample plane, a dedicated rotating probe station (manufactured by Measline Ltd.) driven by a specially designed linear stepper motor driver system is used, described in [11].

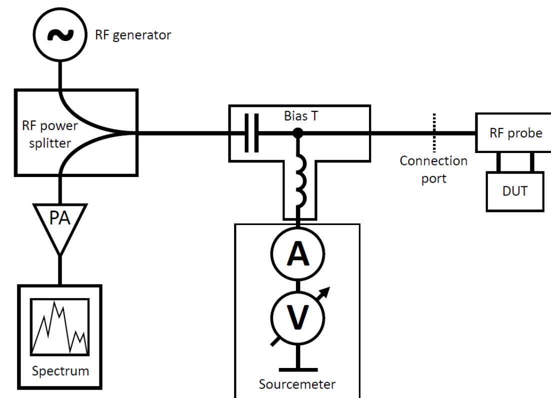

FIG. 2: Measurement setup used for injection locking experiment, utilizing directional coupler, RF generator, spectrum analyser, bias T and sourcemeter.

III. RESULTS

A. Synchronization of a single element to an external $2f$ signal

Following the procedure described in [12] we attempt to synchronize the STO with an external RF signal via the injection locking mechanism. To determine how it affects the signal parameters, we devised a setup (Fig. 2) consisting of two MTJ connected via a bias-T to a sourcemeter (which provides constant current bias) and to the RF setup: directional coupler, spectrum analyzer, and RF signal generator. As it is generally difficult to obtain an ideal impedance matching across connection between the MTJ and probe, as well as the impedance of the MTJ itself usually is different from 50 Ω. This makes observation of direct synchronization to the $1f$ signal difficult due to the significant reflection of the signal from the generator. Therefore, synchronization to the $2f$ signal might be used to investigate the synchronization of the MTJ to an external excitation and the full width at half maximum (FWHM) parameter can be used as a synchronization indicator.

The connected element was powered with a voltage of -250 mV and subjected to a magnetic field of -120.16 kA/m at spherical angles of $\theta = 25^\circ$ relative to the normal surface vector and in-plane $\phi = 110^\circ$ measured from the positive x axis. This resulted in a free oscillation frequency of around 4.075 GHz. Then the signal from the RF generator f_{gen} changed in the frequency range from 7.9 GHz to 8.3 GHz. The center frequency of the oscillation of STO is presented as red dots overlayed on spectra in Fig. 3 and for a range of f_{gen} values it follows the $f_{gen}/2$ frequency, which indicates that element is synchronized with the provided external $2f$ RF signal.

We calculated the FWHM for each measured point, shown in Fig. 3b). In the locking region, the FWHM significantly drops, from the average of 12.5 MHz to less than 2.5 MHz. This drop in the FWHM of the signal is another indication of

3

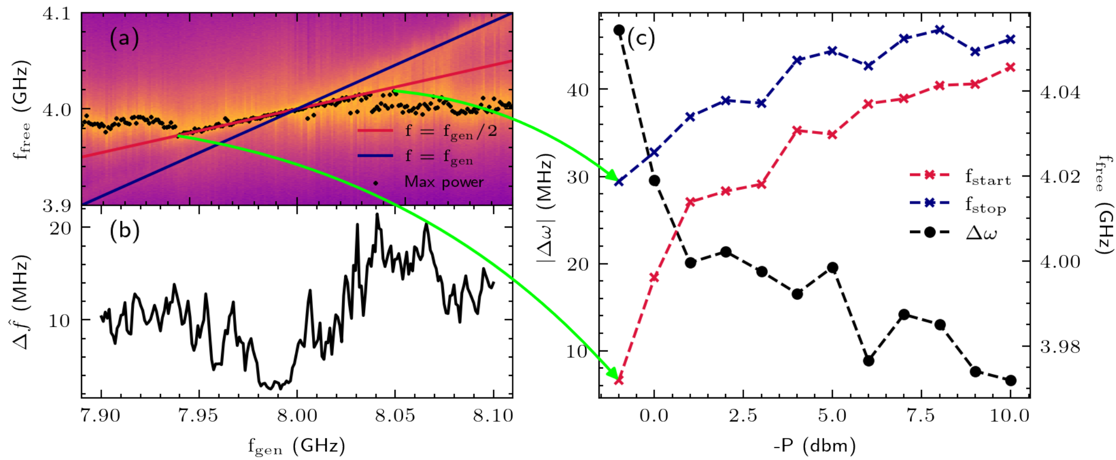

FIG. 3: (a) Power vs. frequency for different f_{gen} values. Black dots represent maximum power points, the red line denotes $f_{gen}/2$ and the dark blue one f_{gen}. (b) FWHM of the signal generated by the STO versus f_{gen}. The synchronization region is accompanied by a decrease in FWHM by a factor of 5. c) locking range $\Delta\omega$ as a function of generator power P. Note that the x-axis is in $-P$ units. As the generator power increases, the locking range increases too.

the synchronization process.

It is worth noting, that for a synchronization to occur, the experimental conditions must be very precisely controlled: the sample must me aligned precisely with an external magnetic field; the value of this magnetic field as well as DC bias require careful experimental tuning with successive approximation to achieve stable free oscillations.

B. Power levels in synchronization to an external $2f$ signal

The next step was to identify the power of the external generator, which is necessary to achieve the synchronization of the two signals. To do so, we need to take into account that power levels set on the equipment and observed during measurements are affected by the measurement setup and electrical connections. Using a vector network analyzer, the transmittance in the path from the RF signal generator to the connection port (see Fig. 2) was determined to be -10.692 dB at the representative frequency of 4.00 GHz. A similar measurement determined that the transmittance on the path from the connection port to the spectrum analyzer is 15.833 dB at the same frequency.

The final path of the signal from the connection port to the sample is realized using an RF probe with flexible RF wires. At this point there is an impedance mismatch between the 50 Ω system and the undetermined impedance of the sample. Therefore, VNA was calibrated with an open, short and reference 50 Ω impedance (Picoprobe Calibration Substrate CS-8) connected to the RF probe and then a measurement was taken with a representative sample connected to the system. This allowed, after some standard and simple calculations, to apply correction to all the measured power levels.

Synchronization, indicated by a decrease in FWHM, was determined to occur at injected power level delivered to the element of around -18.740 dBm, while the true power generated by the element peaks at -29.565 dBm.

If we wanted to employ a similar method of synchronization by using another MTJ in place of the generator, then we would find that the output signal level of the first MTJ injected into the second is below the signal level required for injection locking of the second MTJ. However, what we show below, is that the mechanism of the synchronization to $1f$ is likely more efficient than the one for $2f$.

C. Mutual synchronization of two serially connected STO

We now turn to examining two serially connected STOs, knowing that a decrease in FWHM is a good indicator of the synchronization effect. First, we collected auto-oscillation data for each element separately (indicated as left L and right R in Fig. 4), and then measured them when connected in series with a tail-to-head type connection. In all measurements, the current flowing through the elements was kept at the same value: $I_{DC} = -2.90$ mA. For each situation FWHM we calculated and compared separate elements and their serial connection, as presented in Fig.4a). Both MTJs oscillate at similar conditions, especially at the magnetic fields below 1.6 kA/m, therefore to determine the synchronization conditions, one needs to analyze the oscillation linewidth.

It can be observed that the oscillation pattern is more complex for a serial connection than for a single element. This effect might be attributed to synchronization of the devices to

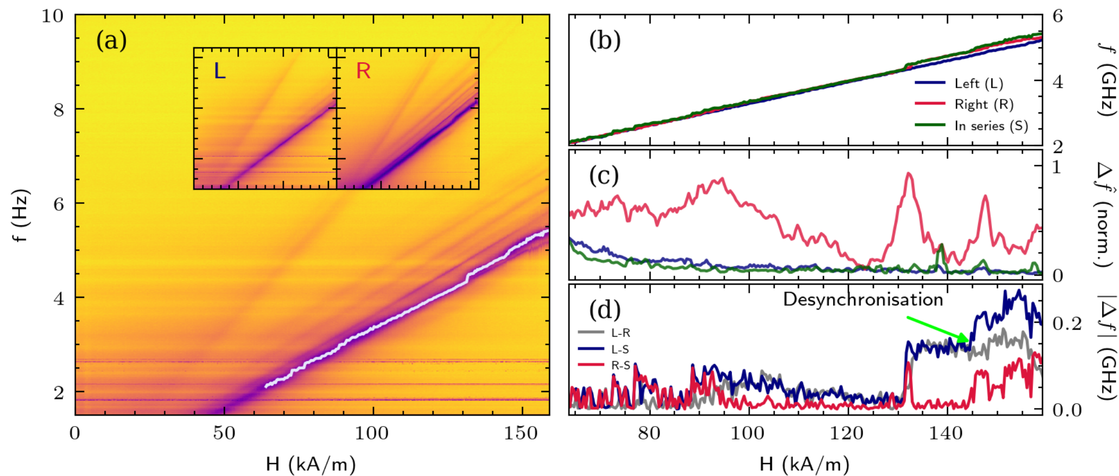

FIG. 4: Electrical synchronization and desynchronization of two serially connected MTJs. (a) In-series signal with insets illustrating separate left (*L*) and right (*R*) MTJ. The lavender-colored line designates the common resonance mode. (b) Main resonance of L, R and in-series systems. (c) FWHM of the resonance spectra and (d) the synchronization and desynchronization ranges of *L* and *R* relative to the in-series (*S*) signal.

each other, as we see a slight decrease in the FWHM value for some narrow conditions. The synchronization mechanism for serially connected MTJs is different from the previously presented synchronization with the $2f$ signal, as in this case we used the $1f$ frequency directly, and the change in FWHM is rather subtle as we are working in a regime of much lower powers than signal from the generator.

Fig. 4 d) reveals more information on the differences between the in series oscillation (S) and individual resonance modes of the L or R elements measured when they were not connected serially. Each line represents an absolute difference between two resonance modes from Fig.4b). Starting from about 95 kA/m we see that the line (L-R) follows the line (L-S), which means that the in-series oscillator aligns itself with one of the individual modes R measured outside the in-series connection, because (R-S) lingers near 0 during that period. This situation continues, even in the region when at approximately 132 kA/m the R and L signals begin to stray further apart from each other. In between, we observe a brief moment of nonforced synchronization in the region 125kA/m, where all signals naturally oscillate with the same frequency, also indicated by a drop in the FWHM visible in Fig.4c). Finally, beyond the 145 kA/m mark, the (L-R) line does not align with either (R-S) or (L-S). Such a pseudo-desynchronization from the R signal means that the in-series system begins to oscillate at its individual mode, different from the one enforced by R as at the lower field values. In order to get deeper insight into the mechanisms of synchronization, we performed a numerical simulations of the serially connected MTJs.

IV. NUMERICAL SIMULATIONS

For numerical simulations, we use the Landau-Lifschitz-Gilbert-Slonczewski (LLGS) macrospin equation [13–16], as implemented in the CMTJ library [17]:

$$\frac{\mathrm{d}\mathbf{m}}{\mathrm{dt}} = -\gamma_0 \mathbf{m} \times \mathbf{H}_{\mathrm{eff}} + \alpha_{\mathrm{G}} \mathbf{m} \times \frac{\mathrm{d}\mathbf{m}}{\mathrm{dt}} + f(\lambda, \eta, \mathbf{p}) \quad (1)$$

where $\mathbf{m} = \frac{\mathbf{M}}{M_s}$ is a normalized magnetization vector, with M_s as magnetization saturation, α_G as dimensionless Gilbert damping parameter, and γ_0 is the gyromagnetic factor. For our simulations, we include the spin-torque form $f(\lambda, \eta, \mathbf{p})$:

$$f(\lambda, \eta, \mathbf{p}) = -\gamma_0 \frac{\hbar j}{e\mu_0 M_s t_{\mathrm{FM}}} \frac{\eta}{1 + \lambda \mathbf{m} \cdot \mathbf{p}} \mathbf{m} \times \mathbf{m} \times \mathbf{p} \quad (2)$$

where $\mathbf{p}$ is the vector of the normalised reference layer, η is the spin polarisation efficiency, t_{FM} as the thickness of the ferromagnetic layer (FM), j is the input current density through the reference layer, and λ is the angular parameter of the STT.

In our experiments, we include the following contributions to the effective field: the demagnetization field, the anisotropy field, and the external magnetic field. Each MTJ is composed of two FM layers, where the bottom layer is set as a reference layer for the top layer, which accounts for the STT modeling.

A. Finding the MTJ parameters

To adequately reproduce the fabrication parameters, we perform Bayesian optimization with respect to the maximum

Parameter	Value	Unit
$M_{s,1}$	0.92	T
$M_{s,2}$	1.21	
$K_{u,1}$	0.31	MJ/m^3
$K_{u,2}$	6.35	

TABLE I: Parameters obtained from running the Bayesian optimisation on the single junction.

resonance lines obtained from the auto-oscillation spectra under DC. In this procedure, we find the optimal parameters for one of the junctions in the pair. We designed a macrospin simulation using the CMTJ package [17] where we sweep with the external magnetic field in the range [0, 160] kA/m, at the polar angle $\theta = 5^\circ$ and the azimuth angle $\phi = 90^\circ$. At each step, we apply a constant current density, equivalent to feeding 1.5mA perpendicularly through the junction. We assumed the perpendicular anisotropy of the top layer and the in-plane anisotropy of the bottom layer. The IEC energy is assumed to be negligible in our experiments. In the next step, we run the Bayesian optimisation algorithm with a mean squared error (MSE) cost function:

$$\text{MSE} = \sum_i (f_i - \bar{f}_i)^2 \quad (3)$$

where the index i iterates over steps of the applied field, f_i is the experimental frequency measured at H_i and $\bar{f}_i$ is the simulated frequency at H_i under the set of parameters currently considered. Due to the multiplicity of proximate solutions [18], it is necessary to limit the design space with a set of the boundaries, thus we seed the optimization process with a boundary condition in the approximate range of reasonable values of M_s and K_u (uniaxial anisotropy constant) for each layer. In our procedures, we used the Python package for Bayesian optimization [19]. Shortly, Bayesian optimisation relies on optimising the acquisition function u over a Gaussian process [20, 21], such that:

$$\hat{\theta} = \underset{\theta}{\text{argmax}}\ u(\theta|\mathscr{D}) \quad (4)$$

where $\mathscr{D}$ is the resonance frequency data, θ are the MTJ parameters to optimise, and $\hat{\theta}$ are the best-fit parameters. The successive suggestions are sourced by evaluating the acquisition function with some added noise. The starting prior is usually chosen as a uniform distribution. We use the upper confidence bound (UCB) algorithm as the acquisition function and run the optimization for 500-1000 steps.

As a result of running the optimization, we obtain an approximate local minimal solution of the saturation magnetization $M_{s,1}$, $M_{s,2}$ and magnetic anisotropy energies $K_{u,1}$, $K_{u,2}$, with final values summarized in Tab.I (the numerical subscript indicates the layer index, 1 denotes free and 2, the reference layer). Fig.5 presents an example auto-oscillation spectrum with the solid line representing the experimentally measured maximum amplitude resonance line.

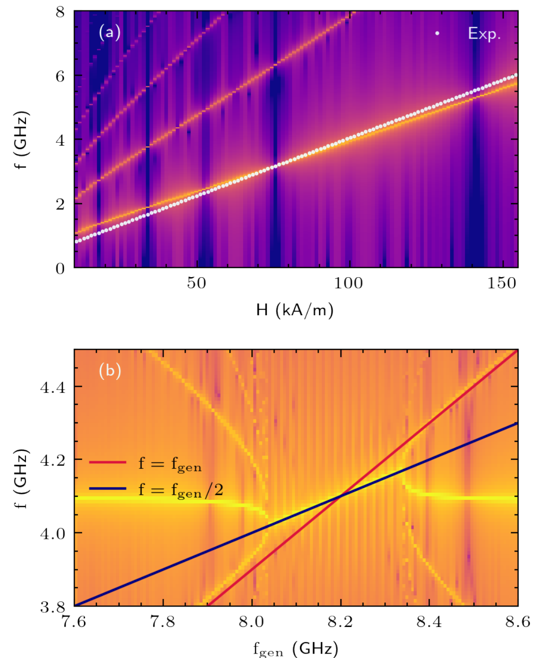

FIG. 5: a) The spectrum computed from the parameters obtained during Bayesian optimisation procedure for a single MTJ. Dotted white line represents the experimental main harmonic resonance line. The precise parameter values have been placed in Tab.I. b) simulated injection locking with $\Delta j_{AC}/j_{DC} \approx 0.2$.

B. Model of synchronization

A theory of synchronization of a single MTJ follows an auto-oscillator theory developed in [22]. First, we attempt to obtain the phenomenon of injection locking at a frequency $2f$, where f is the natural frequency of an MTJ in a given field H_{ext} and j_{dc}. Locking to the $2f$ frequency instead of f has the experimental advantage of removing the crosstalk from the generator. We find a ratio $\Delta j_{ac}/j_{dc}$ between 0.1 and 0.2 sufficient to achieve injection lock. The results of simulated injection locking are depicted in Fig.5b). The MTJ oscillations snap to $f_{gen}/2$ of the locking signal, as illustrated by the change of slope within the synchronization range.

We enforce the synchronization behavior of electrically coupled MTJs after Taniguchi et al. [8]. We assume that two oscillators are sufficiently far apart so that there is no dipole interaction between them. There are two available configurations for connecting two MTJs, serial and parallel, and in this work we only consider the former. In each, the current depends on the free magnetizations **m** and the reference layers **p**

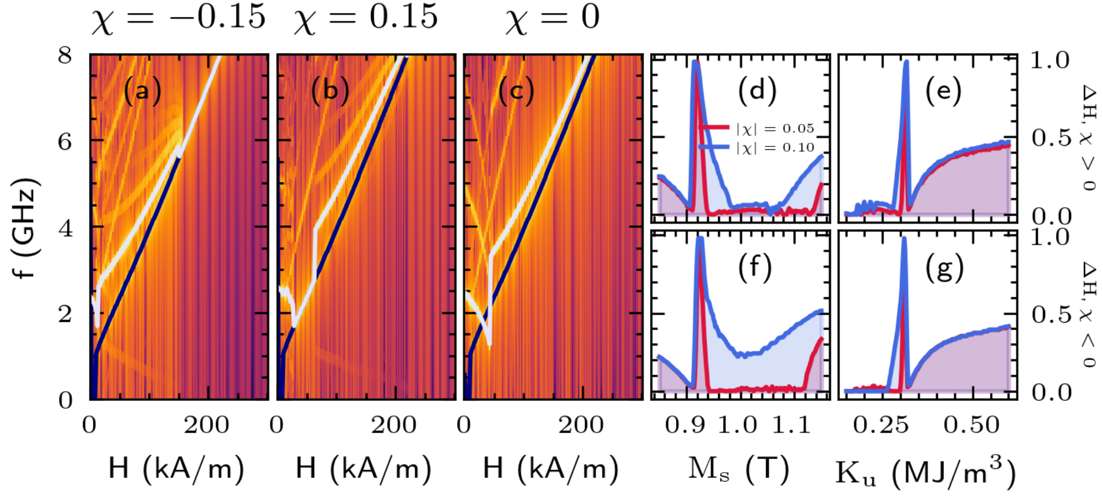

FIG. 6: An example of in-series synchronization and desynchronization of two MTJs. (a-c) negative, positive, and null values of χ, the coupling constant. We can observe that two MTJs begin to synchronize above 125 kA/m in case of negative χ(a) and between 40 and 75 kA/m for a positive χ (B). The dark blue and azure colors in the third panel (c) show the individual resonance modes of MTJs while they are excited with an equal current density before being connected in series. (d-g) Normalized mutual locking ranges ΔH for four values of the coupling constant: d-e) positive and e-g) negative χ, respectively, calculated for a range of $M_{s,2}$ and $K_{u,2}$ values. Red lines denote $|\chi| = 0.05$ and blue lines $|\chi| = 0.1$.

of the junctions i_{th} and $i+1_{th}$:

$$I(t) = I_0(t) + \chi I_0(t)(\mathbf{m_i}\cdot\mathbf{p}_i + \mathbf{m}_{i+1}\cdot\mathbf{p}_{i+1}) \quad \text{(series)} \quad (5)$$

$$I(t) = I_0(t) + \chi I_0(t)(\mathbf{m_i}\cdot\mathbf{p}_i - \mathbf{m}_{i+1}\cdot\mathbf{p}_{i+1}) \quad \text{(parallel)} \quad (6)$$

where $I_0(t)$ is the value of the current fed into the first MTJ in the connection and χ is the unitless coupling strength. We show an example of synchronization in Fig.6. The first of two serially connected MTJs was created with the parameters derived from the Bayesian fitting procedure in the preceding section, while the other had each of its parameters initialized from a normal distribution centered on the original MTJ parameter value, with a standard deviation of δ. The applied external magnetic field is 300 kAm/m, at $(\theta,\phi) = (15,90)$ and the system was excited with a constant current density of 36.7 GA/m^2. In addition, we conducted parametric simulations for the locking ranges ΔH for a range of values of $M_{s,2}$ and $K_{u,2}$ of the second junction of the in-series connection. Upon varying either of the parameters, all remaining values are given as in Tab.I. When the absolute value of χ increases, we observe a widening of the peaks and a clear expansion of the locking range over a larger scale of the parameter variation, most evident in Fig.6f). Interestingly, that increase in χ has a larger impact on the tolerance of the M_s parameter than on the anisotropy energy. The drift towards larger values of the parameter in all figures suggests the secondary harmonic synchronization phenomenon (the natural frequency of the second MTJ naturally increases as either of the parameters increases).

V. DISCUSSION

Achieving electric synchronization with spin-torque oscillators requires a great level of precision and tedious tuning of the junction parameters. Apart from the difficulty in orchestrating the correct setup, specific synchronization ranges depend largely on the relative parameter dispersion. Based on the experimental approach, we were able to present the oscillations in individual STOs and in serially connected pair of MTJs. Finally, we note that the desynchronization, i.e. relative drift of the individual modes from the common mode, can be both measured experimentally and modeled with a relatively simple model. Simulation results suggest that the parallel connection of the STOs may lead to improved synchronization, however without possibility of determining the performance of individual elements. Joint experimental and numerical methodology established in this work allows for inspecting individual MTJs separately and then measuring the resonance spectrum of the same pair in a in-series connection. Such an inductive approach facilitates numerical modelling and as a result may give deeper insight into the operation conditions of the system as a whole. One method to achieve reliable locking of two MTJs in the same mode may be to connect more devices together, creating less selective circuits with broader bandwidths. Developing such a method can lead to promising opportunities for creating arrays of tunable oscillators capable of performing simple computing tasks.

7

[1] K. Roy, A. Jaiswal, and P. Panda, Towards spike-based machine intelligence with neuromorphic computing, Nature **575**, 607 (2019).

[2] M. Romera, P. Talatchian, S. Tsunegi, F. Abreu Araujo, V. Cros, P. Bortolotti, J. Trastoy, K. Yakushiji, A. Fukushima, H. Kubota, S. Yuasa, M. Ernoult, D. Vodenicarevic, T. Hirtzlin, N. Locatelli, D. Querlioz, and J. Grollier, Vowel recognition with four coupled spin-torque nano-oscillators, Nature **563**, 230 (2018).

[3] M. Romera, P. Talatchian, S. Tsunegi, K. Yakushiji, A. Fukushima, H. Kubota, S. Yuasa, V. Cros, P. Bortolotti, M. Ernoult, D. Querlioz, and J. Grollier, Binding events through the mutual synchronization of spintronic nano-neurons, Nat. Commun. **13**, 883 (2022).

[4] J. Torrejon, M. Riou, F. A. Araujo, S. Tsunegi, G. Khalsa, D. Querlioz, P. Bortolotti, V. Cros, K. Yakushiji, A. Fukushima, H. Kubota, S. Yuasa, M. D. Stiles, and J. Grollier, Neuromorphic computing with nanoscale spintronic oscillators, Nature **547**, 428 (2017).

[5] S. Tsunegi, T. Taniguchi, R. Lebrun, K. Yakushiji, V. Cros, J. Grollier, A. Fukushima, S. Yuasa, and H. Kubota, Scaling up electrically synchronized spin torque oscillator networks, Sci. Rep. **8**, 13475 (2018).

[6] M. Zahedinejad, A. A. Awad, S. Muralidhar, R. Khymyn, H. Fulara, H. Mazraati, M. Dvornik, and J. Åkerman, Two-dimensional mutually synchronized spin Hall nano-oscillator arrays for neuromorphic computing, Nature Nanotechnology **15**, 47 (2020).

[7] A. Houshang, M. Zahedinejad, S. Muralidhar, J. Chęciński, R. Khymyn, M. Rajabali, H. Fulara, A. A. Awad, M. Dvornik, and J. Åkerman, Phase-Binarized Spin Hall Nano-Oscillator Arrays: Towards Spin Hall Ising Machines, Phys. Rev. Appl. **17**, 014003 (2022).

[8] T. Taniguchi, Synchronization and chaos in spin torque oscillator with two free layers, AIP Adv. **10**, 015112 (2020).

[9] R. Sharma, R. Mishra, T. Ngo, Y.-X. Guo, S. Fukami, H. Sato, H. Ohno, and H. Yang, Electrically connected spin-torque oscillators array for 2.4 GHz WiFi band transmission and energy harvesting, Nat. Commun. **12**, 2924 (2021).

[10] W. Skowroński, J. Chęciński, S. Ziętek, K. Yakushiji, and S. Yuasa, Microwave magnetic field modulation of spin torque oscillator based on perpendicular magnetic tunnel junctions, Sci. Rep. **9**, 19091 (2019).

[11] W. Skowroński, K. Grochot, P. Rzeszut, S. Łazarski, G. Gajoch, C. Worek, J. Kanak, T. Stobiecki, J. Langer, B. Ocker, and M. Vafaee, Angular Harmonic Hall Voltage and Magnetoresistance Measurements of Pt/FeCoB and Pt-Ti/FeCoB Bilayers for Spin Hall Conductivity Determination, IEEE Transactions on Electron Devices **68**, 6379 (2021).

[12] M. Quinsat, J. F. Sierra, I. Firastrau, V. Tiberkevich, A. Slavin, D. Gusakova, L. D. Buda-Prejbeanu, M. Zarudniev, J.-P. Michel, U. Ebels, B. Dieny, M.-C. Cyrille, J. A. Katine, D. Mauri, and A. Zeltser, Injection locking of tunnel junction oscillators to a microwave current, Applied Physics Letters **98**, 182503 (2011).

[13] T. Gilbert, Classics in Magnetics A Phenomenological Theory of Damping in Ferromagnetic Materials, IEEE Transactions on Magnetics **40**, 3443 (2004).

[14] D. Ralph and M. Stiles, Spin transfer torques, J. Magn. Magn. Mater. **320**, 1190 (2008).

[15] J. Slonczewski, Current-driven excitation of magnetic multilayers, Journal of Magnetism and Magnetic Materials **159**, L1 (1996).

[16] J. Slonczewski, Currents and torques in metallic magnetic multilayers, J. Magn. Magn. Mater. **247**, 324 (2002).

[17] J. Mojsiejuk, S. Ziętek, K. Grochot, W. Skowroński, and T. Stobiecki, cmtj: Simulation package for analysis of multilayer spintronic devices, npj Computational Materials **9**, 54 (2023).

[18] S. Ziętek, J. Mojsiejuk, K. Grochot, S. Łazarski, W. Skowroński, and T. Stobiecki, Numerical model of harmonic Hall voltage detection for spintronic devices, Physical Review B **106**, 024403 (2022).

[19] fernando, Bayesian Optimization (2022), original-date: 2014-06-06T08:18:56Z.

[20] E. Brochu, V. M. Cora, and N. de Freitas, *A Tutorial on Bayesian Optimization of Expensive Cost Functions, with Application to Active User Modeling and Hierarchical Reinforcement Learning*, Tech. Rep. arXiv:1012.2599 (arXiv, 2010) arXiv:1012.2599 [cs] version: 1 type: article.

[21] J. Snoek, H. Larochelle, and R. P. Adams, Practical Bayesian Optimization of Machine Learning Algorithms, in *Advances in Neural Information Processing Systems*, Vol. 25 (Curran Associates, Inc., 2012).

[22] A. Slavin and V. Tiberkevich, Nonlinear Auto-Oscillator Theory of Microwave Generation by Spin-Polarized Current, IEEE Transactions on Magnetics **45**, 1875 (2009).

7. Measurement and fabrication techniques

During work on this thesis mainly experimental work was done, what included fabrication of samples as well as taking measurements and afterwards analyzing the results. In this chapter manufacturing process of the spntronic nanodevices is described, the measurement setups used for characterization of such devices are presented and finally software used for automatization of such measurements as well as data analysis.

7.1. Fabrication

Multilayer structures were prepared externally by Singulus AG (Germany) and in AIST (Japan) on an oxidised silicon substrate (Figs. 7.1-7.3). Nanofabrication was carried out in the Academic Center of Materials and Nanotechnology (ACMiN AGH) and the process and its description was adapted from [30] with some changes introducing mixed-match litography using both UV and e-beam processes. Earlier the whole process was done using e-beam litography, but this approach tended to be very time-consuming, as exposure of large areas of top and bottom electrode were slow. This was eliminated with usage of MicroWriter ML3 Pro by Durham Magneto Optics direct-write UV-litography system, which allows for quick exposures of large areas with an effective process resolution of around $1\,\mu\mathrm{m}$, which is enough for electrodes/contacts while reducing time needed for this exposure from around $6\,\mathrm{h}$ to $4\,\mathrm{min}$.

To produce a spintronic nanodevice following steps are taken:

- the bottom electrode is being formed (Figs. 7.4-7.7)
- the insulation is applied, to prevent forming unwanted connections during further processing (Figs. 7.8-7.9)
- pillars and vias are formed and the insulation oxide is applied (Figs. 7.10-7.14)
- top electrode is formed, including measurement contacts and other connections (Figs. 7.15-7.20)

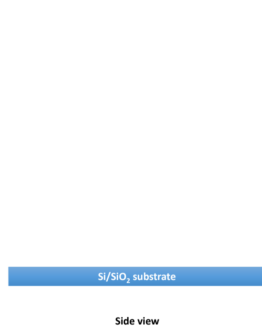

Figure 7.1: A polished and (if required) oxidised silicon wafer is prepared for processing. Size/thickness in this and the following figures are not to scale.

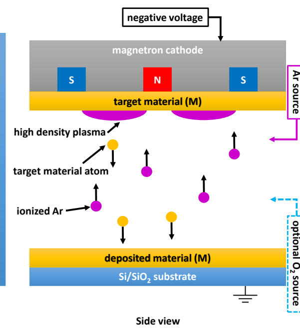

Figure 7.2: A thin film of target material is deposited by means of magnetron sputtering. Optionally, an oxygen flow may be provided in order to deposit target material oxide (e.g. MgO, Al_2O_3).

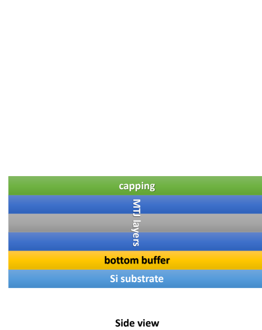

Figure 7.3: Requested layer stack with metallic bottom buffer and capping layer is deposited by means of magnetron sputtering. The sample might be annealed to recrystallize all layers.

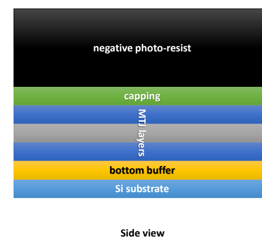

Figure 7.4: A negative UV photo-resist (AR-N 4340) is applied in spin-coater at 6000 rpm, resulting in thickness of approx. 1.25 µm. Then the sample is baked for 60 s at 90 °C.

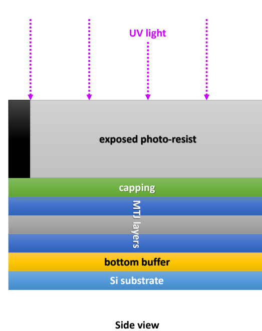

Figure 7.5: The UV photo-resist is exposed using UV direct-write process to transfer bottom electrode shape. After the exposure the sample is baked for 120 s at 95 °C

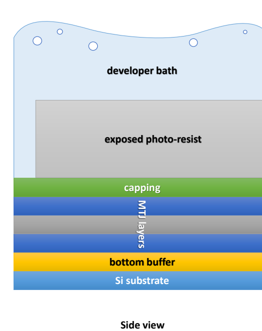

Figure 7.6: The UV photo-resist is developed using AR 300-475 developer bath for 20 s and then rinsed in deionized water (DI-H_2O) for 30 s.

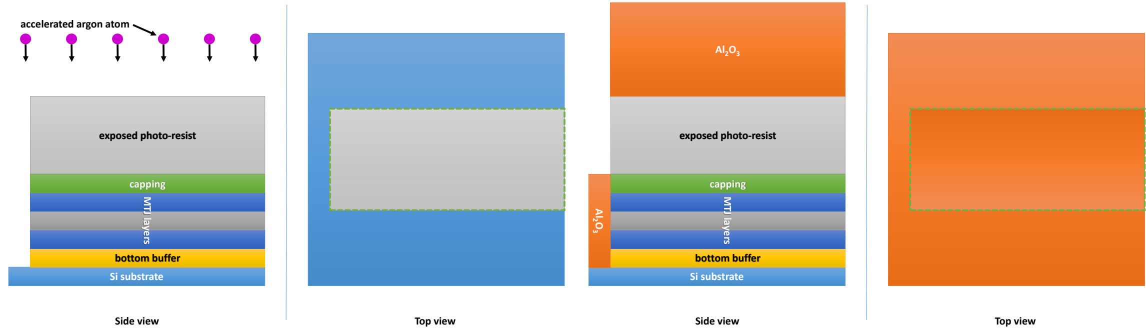

Figure 7.7: The sample is etched using ion etching to form a bottom electrode shape by reaching Si substrate. Mass spectrometer is used to determine layers that are being etched.

Figure 7.8: Al_2O_3 is deposited to match the etched height, using magnetron sputtering with Al target and O_2 injection near the sample.

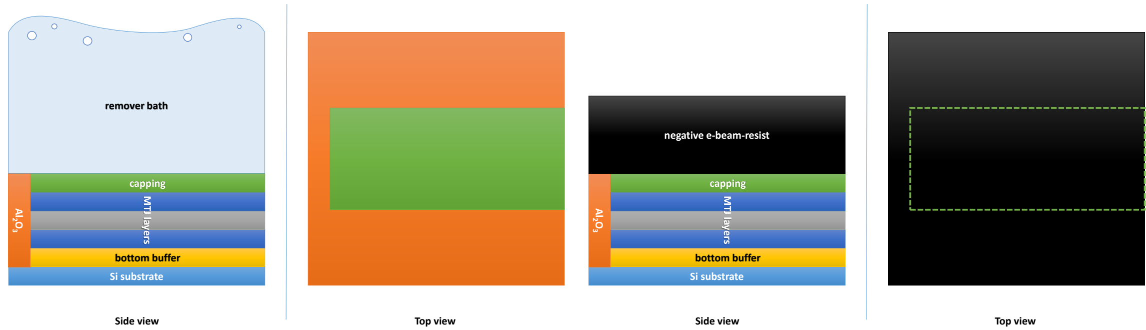

Figure 7.9: The UV photo-resist is removed with excess Al_2O_3 (the lift-off process) using 1-Methyl-2-pyrrolidinone by Sigma-Aldrich in ultrasonic washer for 15 min at 72 °C.

Figure 7.10: A negative e-beam-resist (AR-N 7520.17) is applied in spin-coater at 6000 rpm, resulting in thickness of approx. 0.3 µm . Then the sample is baked for 60 s at 85 °C.

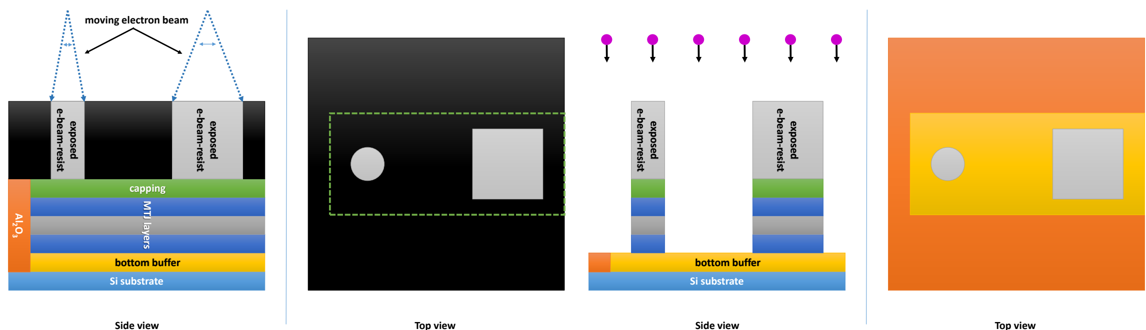

Figure 7.11: The e-beam-resist is exposed using electron beam to transfer pillar (circle) and via (square) shapes. (Dimensions in the figure are not to scale).

Figure 7.12: After developing the e-ebam-resist (AR 300-46 for 90 s, DI-H_2O for 30 s) etching is performed to reach bottom buffer. Etching time is strictly controlled based on the mass spectrometer signal, referenced to the data obtained during the first etching process (Fig. 7.7). The pillar and the via are formed.

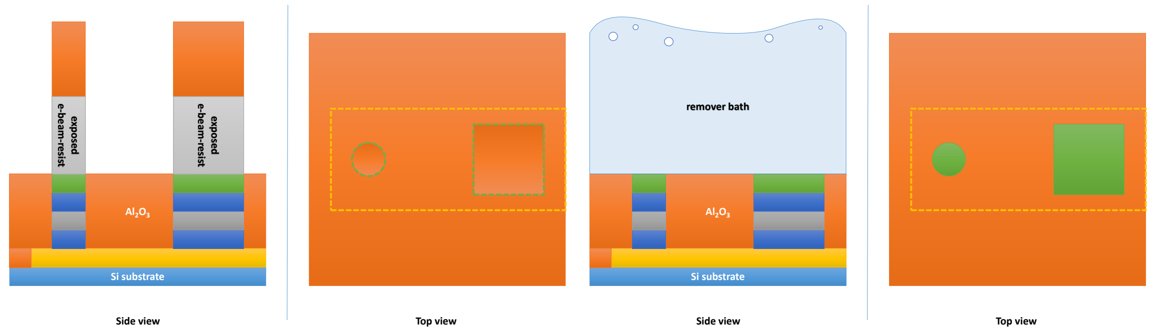

Figure 7.13: Al_2O_3 is deposited to match the etched height, using magnetron sputtering.

Figure 7.14: The e-beam-resist is removed with excess Al_2O_3 (the lift-off process) using 1-Methyl-2-pyrrolidinone by Sigma-Aldrich in ultrasonic washer for 15 min at 72 °C.

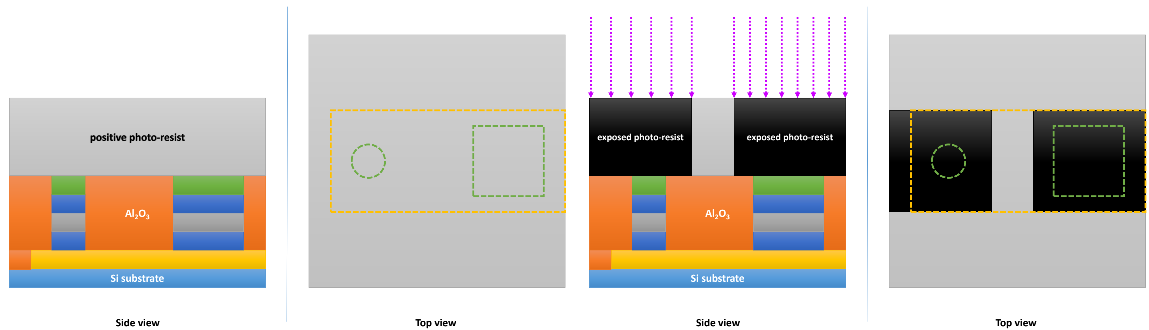

Figure 7.15: A positive UV photo-resist (AR-P 3740) is applied in spin-coater at 6000 rpm, resulting in thickness of approx. 1.7 µm . Then the sample is baked for 60 s at 1000 °C.

Figure 7.16: The UV photo-resist is exposed using UV direct-write process to transfer top electrode shape.

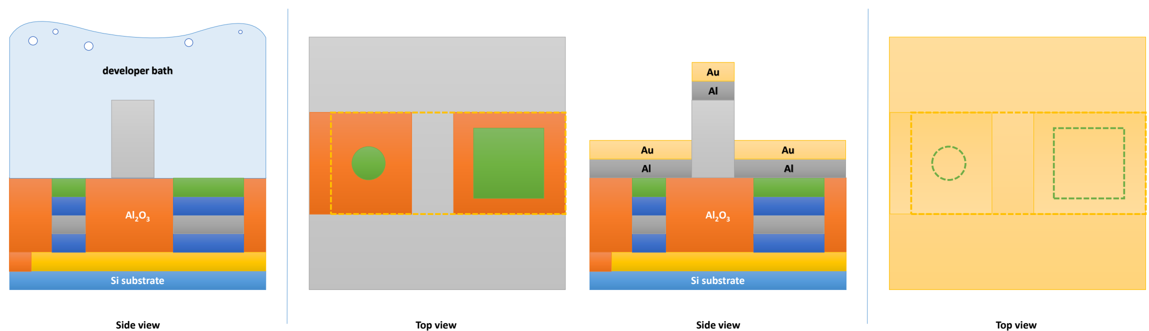

Figure 7.17: The UV photo-resist is developed using AR 300-47 developer bath for 10 s and then rinsed in $DI\text{-}H_2O$ for 30 s.

Figure 7.18: Al (as buffer) and then Au (as top electrode) are deposited using magnetron sputtering.

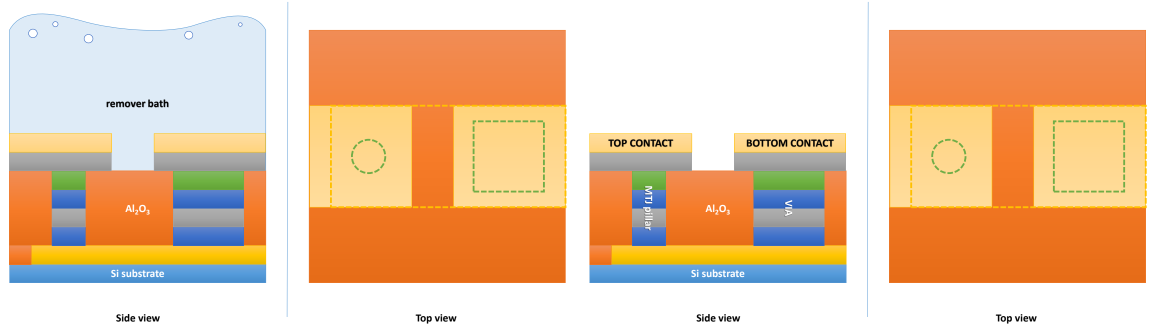

Figure 7.19: The UV photo-resist is removed with excess Al and Au (the lift-off process) using 1-Methyl-2-pyrrolidinone by Sigma-Aldrich in ultrasonic washer for 15 min at 72 °C.

Figure 7.20: The process is completed. Contacts to access top and bottom side of the MTJ pillar are available.

7.2. Measurement setups

To perform measurements that lead to preparation of this thesis generally two types of measurement setups were used - one for DC measurements and other for measurements in RF regime. Both of the setups allowed for external magnetic field application, measurement of DC resistance and application of constant voltage across units under measurement. The measurements for bot types of measurement were automated or semi automated by means of usage of computer software, what allowed to take large number of measurements in a repeatable conditions.

7.2.1. DC measurement setup

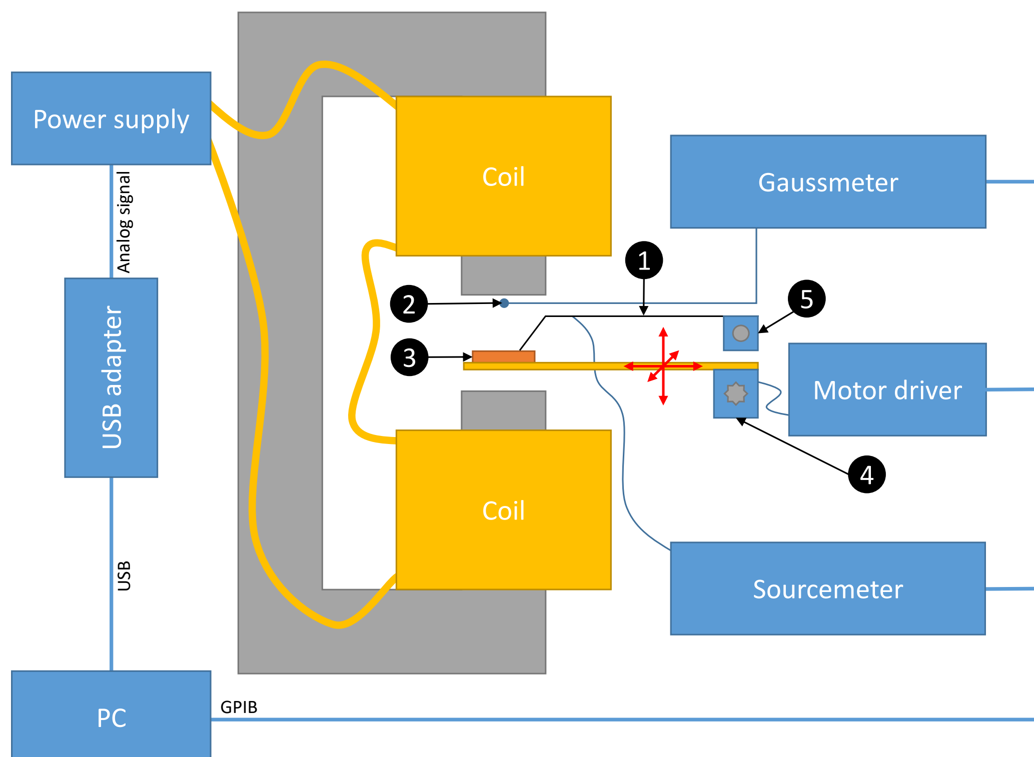

Figure 7.21: Schematic drawing of the DC measurement station. 1 - contact needle (up to 4 were used), 2 - gaussmeter probe, 3 - sample mounted on non-magnetic arm (both in-plane and out-of-plane orientations relative to magnetic field are possible to achieve), 4 - motorized XYZ stage, 5 - fixed micro-positioner to provide contact needle alignment. Red arrows indicating possible movement directions. Drawing adapted from [30].

The DC measurement setup (Figs. 7.21,7.22) is mechanically build based on a stationary linear electromagnet (GMW-3480). Inside we have a sample holder operated by a tri-axial linear motion system (Newport M-460P, Newport M360-90) motorized with electrical multimeter screws with position sensors (Newport LTA-HS for X and Y axes and Newport TRA25PPD for Z axis)

controlled with programmable motion controller (ESP-300). The mechanical side of the setup is finished with up to 4-point electrical contacts (using gold or tungsten needles) operated by manual micropositioners. This allows for placement of the sample parallel or perpendicular to the external magnetic field and provide up to 4 electrical contacts. The motorized motion system allows to automatically change measured element[88] (by changing sample position under electrical contacts), what results in ability to automatically gather data for large number of elements.

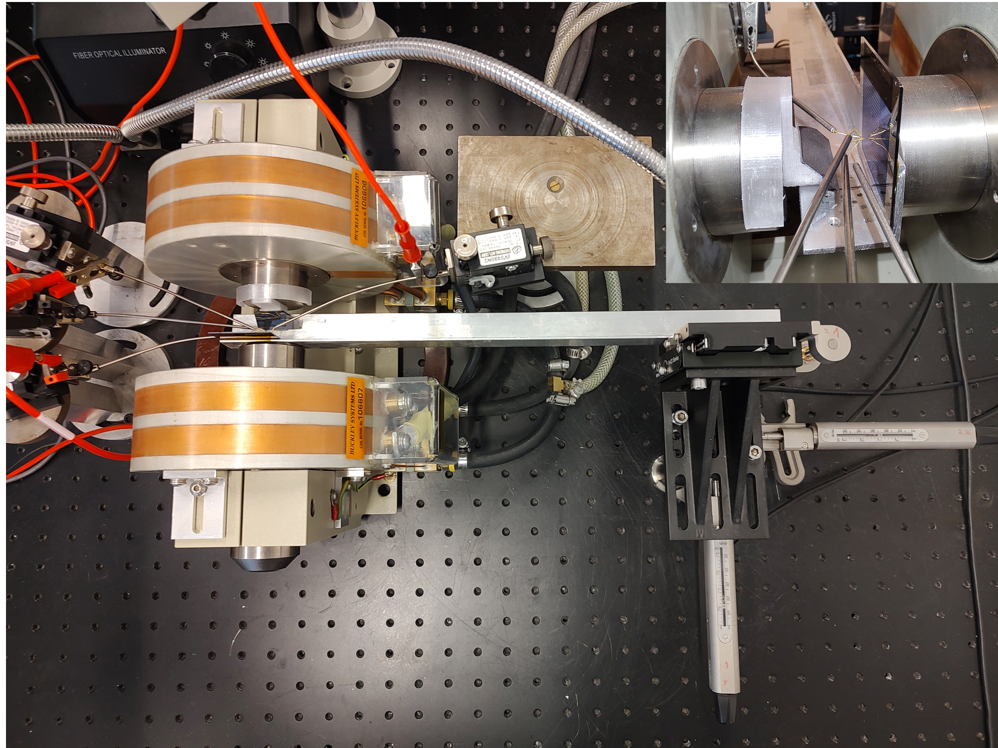

Figure 7.22: DC measurement station photo, presenting stationary linear electromagnet, four DC-probes with micropositioners and a 3D motorized stage. Inset in right corner: detail of the sample placement with probing needles ready to be connected.

The electrical part of the DC measurement system is primarily based on a sourcemeter (Agilent B2912A) that is used to perform 2- and 4-point measurements of resistance of the sample. The setup is completed with means of controlling and measuring the magnetic field consisting of gaussmeter (Lakeshore DSP-475) with a probe placed as near to the sample as possible, a programmable voltage source (NI USB-6009) controlling voltage controlled current source (BOP 36-12M) which powers the electromagnet coils. Additionally coils might be cooled by a forced water flow if it is necessary. The setup is capable of producing magnetic field up to $400\,\mathrm{kA/m}$.

7.2.2. RF measurement setup

The RF measurement setup (Figs. 7.23,7.24) is constructed based on a stationary linear electromagnet (GMW model 3472-70), with attached custom-made dual-axis rotation station. In the station sample might be connected with up to 5-point contact probe, with 4 of its

connections capable of forming 2 RF channels. The rotation station is driven with a custom made linear stepper motor driver to reduce electromagnetic noise, which was previously produced by pulse-width-modulation drivers [89]. The setup allows for applying any arbitrary magnetic field, as the sample might be fully rotated inside the electromagnet.

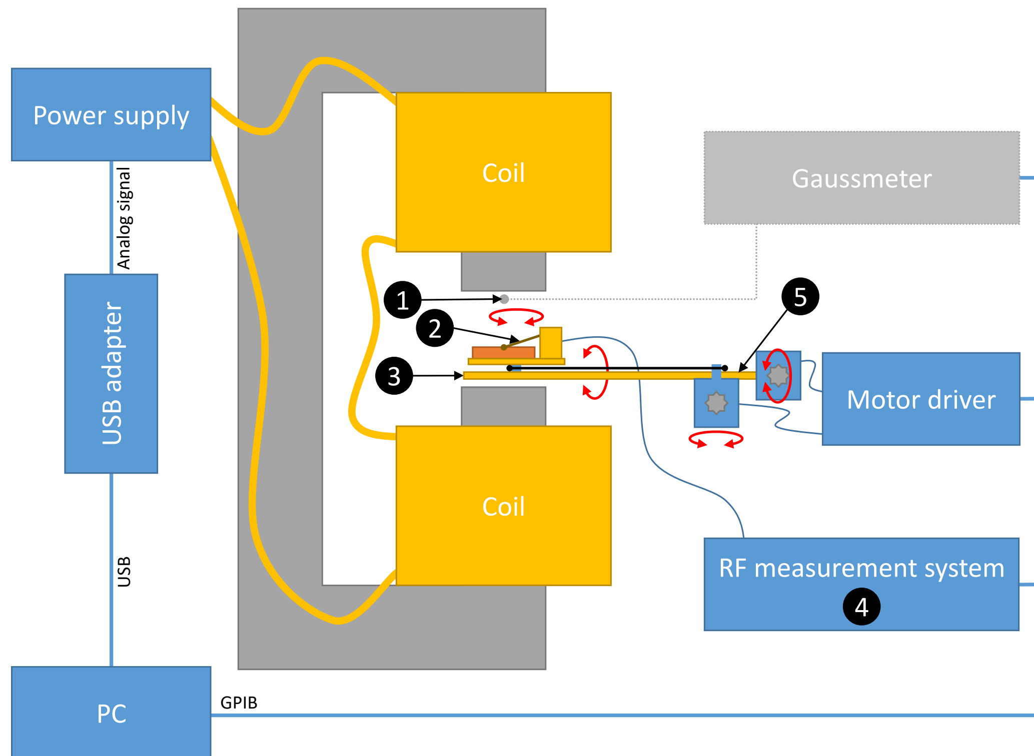

Figure 7.23: Schematic drawing of the RF measurement station. 1 - gaussmeter probe (used for calibration and removed during actual measurement), 2 - 5-point RF probe connected to RF measurement setup, 3 - sample mounted on dual-axis rotating arm, 4 - RF measurement system, see Fig. 7.25, 5 - dual-axis motorized rotating arm with two motors to allow rotation of ϕ and θ. Red arrows indicating possible movement directions. Drawing adapted from [30].

The electrical setup (Fig. 7.25) connects to the sample using 5-point 2-RF channel probe. Then there is a bias-T (Mini-Circuits ZX86-12G-S+) connected which allows for separation of DC signal from RF signal. On a DC port of the bias-T a sourcemeter is connected (Keysight B2912A) allowing for DC resistance measurement as well as providing DC voltage bias to power the device under measurement while observing generation of RF signals. The RF port of the bias-T is connected to a power splitter (Mini-Circuits ZN2PD2-14W-S+). Its first symmetrical ports connects to RF signal generator (Agilent E8257D). The second port of the splitter connects to RF spectrum analyser (Agilent N9030A) with RF power amplifier (Mini-Circuits ZVA-213-S+). The amplifier is powered with DC power supply. The setup is completed with means of controlling and measuring the magnetic field consisting of gaussmeter (Lakeshore DSP-475) with a probe used before a measurement to calibrate conversion between control voltage and generated magnetic

field. The reason for no continous magnetic field measurement is the fact, that sample rotates in the setup thus it is not possible to easily place a magnetic field sensor nearby. Similarly to a DC setup, a programmable voltage source (NI USB-6009) is controlling voltage controlled current source (BOP 50-20MG) which powers the electromagnet coils. Additionally coils might be cooled by a forced water flow if it is necessary. The setup is capable of producing magnetic field up to $640\,\mathrm{kA/m}$.

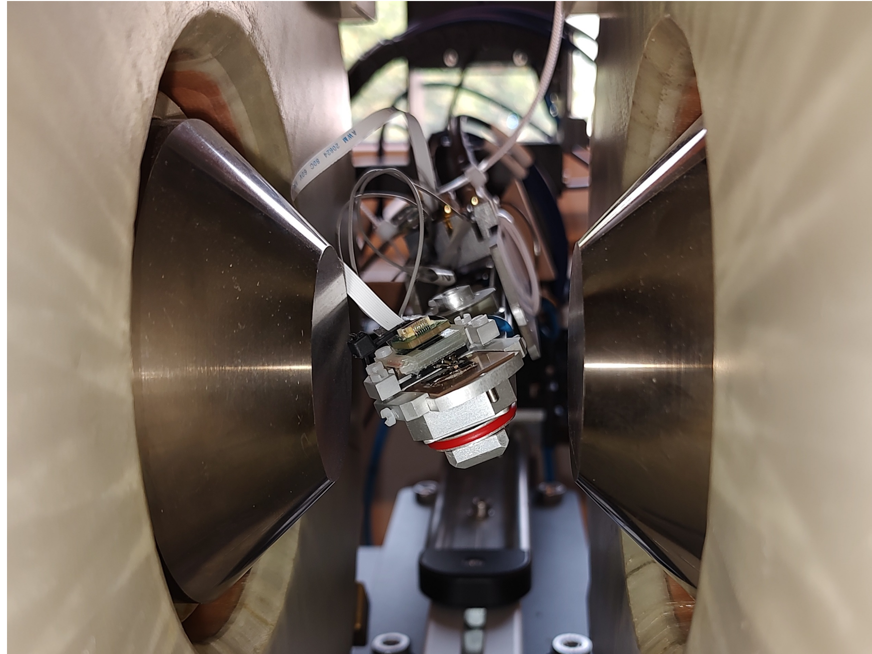

Figure 7.24: RF measurement station photo, presenting fragment of stationary linear electromagnet, RF probe with sample connected placed on a dual axis rotational stage. The stage is fully inserted into the electromagnet.

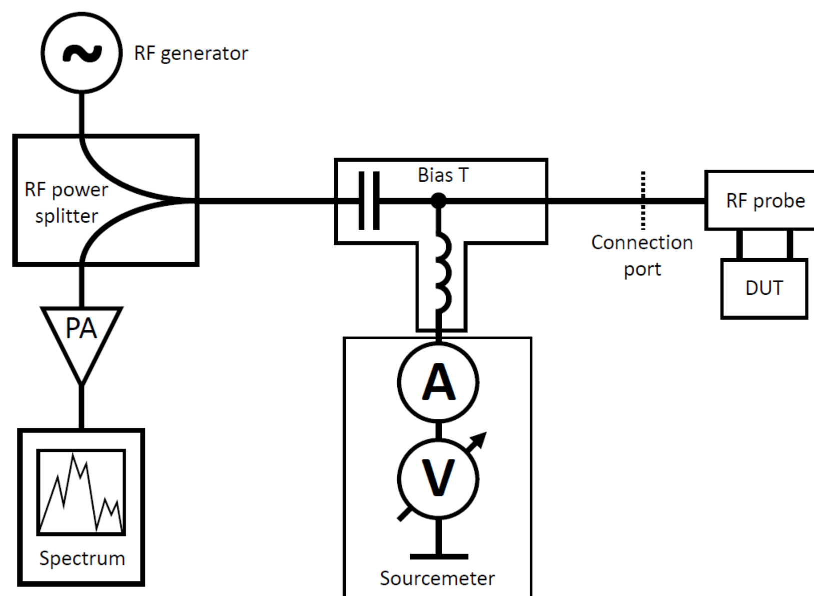

Figure 7.25: RF measurement system block diagram. PA stands for RF power amplifier, DUT - spintronic device under test. As presented in [3]

7.3. Software

The most important part of the measurement system, regardless of the fact how complex measurement equipment is being used, is software that performs various types of measurements on each of the hardware setups. This was crucial during all the experiments conducted, as allowed to collect wide range of data for different samples and conditions (like external magnetic field vector, applied voltage and any possible combination of them all) without manual intervention.

Also the software was used for automated data analysis to extract data of interest and then prepare logical and nearly ready-to-present views of such analysis results. What is more an automated analysis process allowed to provide some feedback "on-the-fly", so further measurement parameters adjustments could be done quickly. This not only improves overall throughput, but also reduces interruptions in measurement process, so the long term ambient condition changes (like temperature variations) are greatly reduced during the whole process.

7.3.1. LabVIEW software

In the beginning of preparation of this thesis mainly software designed in LabVIEW (by the supervisor of the thesis and then developed by various members of the research team, including the author of the thesis) was used (Fig. 7.26). The software provided an advanced graphical user interface with capability of displaying multiple measurement series as well as executing single or series of measurement with different parameters swept. The tool allowed for performing very wide range of measurement types, however it is worth noting that adding a new custom measurement was not so straightforward due to usage of LabVIEW. The software also allowed for data export using various formats and both single measurements and selected subsets of them. The measurement export data included whole numerical data that was logged as well as some basic information about the measurement - this means sometimes not enough data was stored to fully reproduce measurement conditions as seen from software point of view. The software was handy and was a great step towards measurement automation, but after a years of usage and lots of modifications by various users it started to be impossible to maintain (including version control) as well as LabVIEW itself caused a lot of stability- and resource-related issues, especially when collecting large sets of data (fortunately the software included some measures that provided some data backup in case of failure).

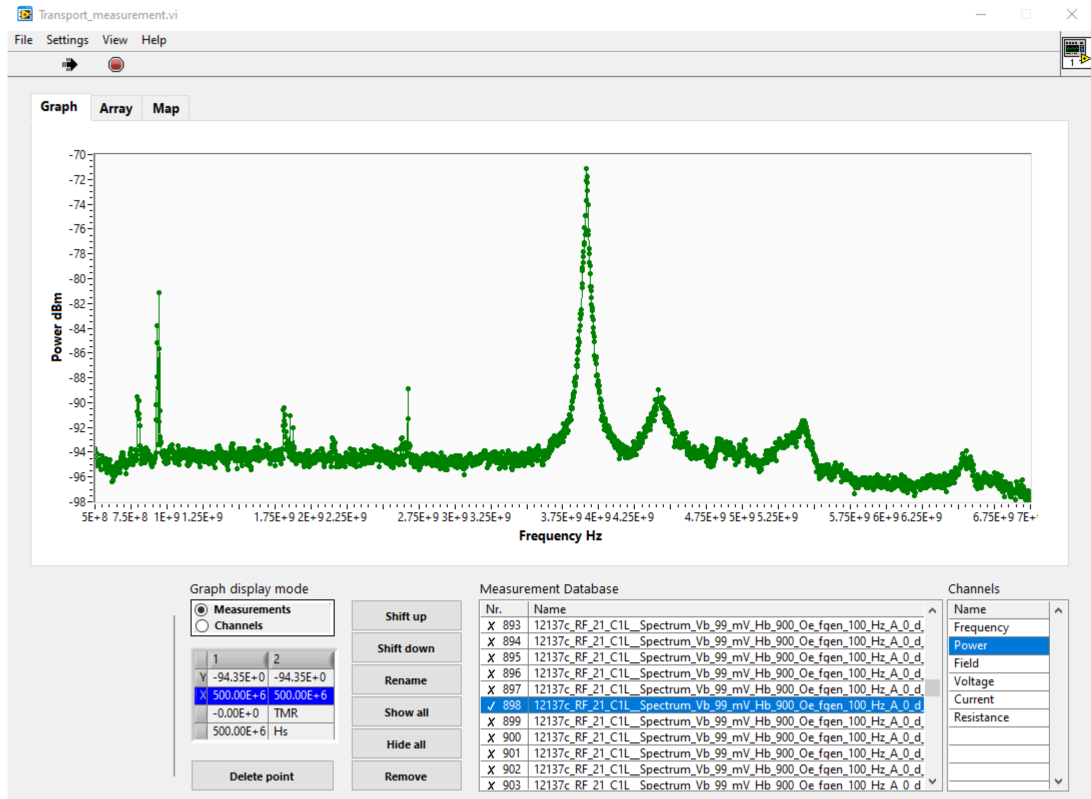

Figure 7.26: Screenshot of LabVIEW software (Transport Measurement) used for multitude spintronics measurements.

7.3.2. Python software

The author of the thesis, facing issues with previously described LabVIEW software decided to prepare a lightweight and independent tool to perform automated measurements as well as a tool-set to automatically analyse measurement results. The programming language of choice was Python as it combines flexibility, relatively low resource utilization, wide range of available libraries and other utilities (like easy access to physical IO including GPIB or RS232 as well as wide range of libraries for data storage, analysis and display).

The decision was made to opt-out from having a graphical user interface, as it was the main limiting factor in terms of measurement flexibility. Instead of that the software might be considered as a set of functions that provide easy access to all measurement steps needed as well as data storage and simple display (Fig. 7.27). Such approach enables for very easy development for even complex measurement procedures, with multiple nested measurement loops, each changing other set of parameters. Also changing order as well as removal or addition of measurement steps might be easily achieved as each experiment control procedure might be considered as a separate Python script. What is more, Python as a text-based language, in contrary to LabVIEW graphical software design, can be easily version-controlled and maintained by allowing for easy change comparison between subsequent alterations by the users. Last but not least, the data storage was much improved in various ways. First of all an important feature was included, that stores the

whole measurement script alongside with the data collected, allowing for easy reproduction of the exact measurement, even if some data was not included in comments. Also the data is transferred to the non-volatile storage from RAM of the computer every time such operation is requested, what allows to easily manage RAM utilization during the measurement process. Finally the data is stored by default in a human-readable format (JSON) and divided across multiple files. In order to reduce the size of the file as well as provide a single file containing all the data of interest a whole set is compressed into a *.zip archive that simultaneously allows for very easy data access. A final touch is semi-automated file naming, that includes both user-provided file name core as well as automatically added date and time of the measurement. Overall the stability of measurement process was greatly improved and the measurement time was significantly reduced as compared to LabVIEW-based solution - for a representative measurement of synchronization to $2f$ signal, as presented in Ch. 6, time was reduced from around $12\,\mathrm{h}$ to $8\,\mathrm{h}$.

```
for H in np.linspace(Hcent - Hrange / 2, Hcent + Hrange / 2, Hpoints):
    msmnum += 1
    time_start = time.time()
    field.setFieldSlow(H)
    msmData.setParam('H', H, 'Oe')
    sm.setOutput(True)
    plotSleep(0.7)

    msmData.setParam('V', sm.measureVoltage()*1000.0, 'mV')
    msmData.setParam('I', sm.measureCurrent()*1000.0, 'mA')
    msmData.setParam('R', sm.measureResistance(), 'Ohm')

    freq, power = sa.getMeasurement(120.0)
    msmData.addMeasurement(np.array(freq)/1e9, power, True)
    sm.setOutput(False)
    msmData.completeSeries()
    tim = time.time() - time_start
    times.append(tim)

    avg = sum(times) / len(times)
    left = avg * (msmtot - msmnum)

    print("--- {:.6f} s ---".format(tim))
    print("--- {:.0f} % ---".format(msmnum / msmtot * 100))
    print("--- {:s} LEFT".format(str(dt.timedelta(seconds=round(left)))))
    print()

sm.setOutput(False)
fgen.setOutput(False)
field.setFieldSlow(0)
print("Finished!!!")
msmData.finish()
```

Figure 7.27: Screenshot of fragment of Python-based measurement script including main measurement loop as well as measurement time prediction.

8. Summary

The thesis presented two novel and promising applications of magnetic tunnel junctions as well as research leading towards even more. Also an comprehensive description of research methods, fabrication processes and tools used was included to allow for reproducing of the results.

The first novel concept presented was multi-state MRAM cell, obtained by serially (head-to-tail) connecting multiple magnetic tunnel junctions. Such a connection allows for gradual and quantized resistance increase of the system, instant decrease of the resistance level to minimum value and a wide range of positive and negative voltages not resulting in any change of the system state. Systems of up to seven serially connected MTJs were experimentally tested and exhibited up to eight stable states, what allows for storage of three bits of data in a single device. Considering the fact, that usually cell-driving transistor size is greater than size of actual MRAM cell and is related to switching current needed, such a solution provides a way to increase data density in future MRAM devices.

Basing on the previous research, and considering challenges in producing multi-state MRAM cells with small parameter variance, another application of such cells was emerging: artificial neural networks. First an behavioral model of single MTJ was prepared, that allowed to perform simulations of serially connected elements, so a model of $R(V)$ curve for a multi-bit cell was possible to be computed. Next an architecture of voltage feed-forward artificial neural network involving such elements was presented, and reflected in standard CMOS technology of UMC $180\,\mathrm{nm}$. Combining all the data a full simulation of such neural network was performed, proving that results of such computing idea are promising and might replace other solutions in the field, as they prove to be energy efficient.

The success in designing the artificial neural network lead to further interest in the area. As other researchers examined artificial neural networks working in pulse or frequency domains it is assumed that some interconnections of spin torque oscillators may lead to an interesting solution too. On the path towards such solutions experiments were made to check on how spin torque oscillators might synchronize their signal to an external signal and signal generated by other elements of the same type. Such experiments lead to a very clear and strong synchronization to external signal of $2f$, therefore use of such components as frequency dividers is possible. Also a mutual effects between two serially (head-to-tail) connected elements were observed, including

synchronization of their oscillation. Such results are promising and serve as a good starting point for further research in the field of using spin torque oscillators in artificial neural networks.

Overall a few practical applications of magnetic tunnel junctions were proposed and proven to work. Also a research towards new circuits involving spintronic devices were done. The whole research process was very complicated, as fabrication of MTJs as nanodevices was challenging and very time-consuming. Also sometimes the fabrication process was not successful, even due to slightest variation of fabrication parameters. What is more the measurement process posed other types of challenges, such as practical inability to reproduce exact connection characteristics between experiments separated in time as well as often loosing unprotected and sensitive bare MTJs to various kind of electrical spikes in the measurement system, that occurred despite proper shielding and grounding of all the equipment. Taking all of this into account, as well as good and promising results of the experiments taken, the whole work might be declared as successful. It is hoped that outcome of the research will lead to significant applications of magnetic tunnel junctions in industry as well as will extend overall knowledge in this area by being a starting point for future studies in the matter.

Bibliography

[1] P. Rzeszut, W. Skowroński, S. Ziętek, J. Wrona, and T. Stobiecki, "Multi-bit MRAM storage cells utilizing serially connected perpendicular magnetic tunnel junctions," *Journal of Applied Physics*, vol. 125, no. 22, p. 223907, 2019.

[2] P. Rzeszut, J. Chęciński, I. Brzozowski, S. Ziętek, W. Skowroński, and T. Stobiecki, "Multi-state MRAM cells for hardware neuromorphic computing," *Scientific Reports*, vol. 12, no. 1, pp. 1–11, 2022.

[3] P. Rzeszut, J. Mojsiejuk, W. Skowroński, S. Tsunegi, H. Kubota, and S. Yuasa, "Towards mutual synchronization of serially connected Spin Torque Oscillators based on magnetic tunnel junctions," *arXiv preprint arXiv:2306.11608*, 2023.

[4] N. Jones *et al.*, "How to stop data centres from gobbling up the world's electricity," *Nature*, vol. 561, no. 7722, pp. 163–166, 2018.

[5] J. Puebla, J. Kim, K. Kondou, and Y. Otani, "Spintronic devices for energy-efficient data storage and energy harvesting," *Communications Materials*, vol. 1, no. 1, p. 24, 2020.

[6] P. Barla, V. K. Joshi, and S. Bhat, "Spintronic devices: a promising alternative to CMOS devices," *Journal of Computational Electronics*, vol. 20, no. 2, pp. 805–837, 2021.

[7] M. N. Baibich, J. M. Broto, A. Fert, F. N. Van Dau, F. Petroff, P. Etienne, G. Creuzet, A. Friederich, and J. Chazelas, "Giant magnetoresistance of (001) Fe/(001) Cr magnetic superlattices," *Physical review letters*, vol. 61, no. 21, p. 2472, 1988.

[8] G. Binasch, P. Grünberg, F. Saurenbach, and W. Zinn, "Enhanced magnetoresistance in layered magnetic structures with antiferromagnetic interlayer exchange," *Physical review B*, vol. 39, no. 7, p. 4828, 1989.

[9] S. Kumar, R. S. Williams, and Z. Wang, "Third-order nanocircuit elements for neuromorphic engineering," *Nature*, vol. 585, no. 7826, pp. 518–523, 2020.

[10] F. A. Khanday, N. A. Kant, M. R. Dar, T. Z. A. Zulkifli, and C. Psychalinos, "Low-voltage low-power integrable CMOS circuit implementation of integer-and fractional–order

FitzHugh–Nagumo neuron model," *IEEE Transactions on Neural Networks and Learning Systems*, vol. 30, no. 7, pp. 2108–2122, 2018.

[11] A. Tavanaei, M. Ghodrati, S. R. Kheradpisheh, T. Masquelier, and A. Maida, "Deep learning in spiking neural networks," *Neural networks*, vol. 111, pp. 47–63, 2019.

[12] W. A. Borders, A. Z. Pervaiz, S. Fukami, K. Y. Camsari, H. Ohno, and S. Datta, "Integer factorization using stochastic magnetic tunnel junctions," *Nature*, vol. 573, no. 7774, pp. 390–393, 2019.

[13] S. Ikegawa, F. B. Mancoff, J. Janesky, and S. Aggarwal, "Magnetoresistive random access memory: Present and future," *IEEE Transactions on Electron Devices*, vol. 67, no. 4, pp. 1407–1419, 2020.

[14] C.-H. Chen, C.-Y. Chang, C.-H. Weng, T.-H. Kuo, C.-Y. Wang, M.-C. Shih, T.-W. Chiang, Y.-J. Lee, R. Wang, K.-H. Shen *et al.*, "Reliability and magnetic immunity of reflow-capable embedded STT-MRAM in 16nm FinFET CMOS process," in *2021 Symposium on VLSI Technology*. IEEE, 2021, pp. 1–2.

[15] W. Thomson, "XIX. On the electro-dynamic qualities of metals:—Effects of magnetization on the electric conductivity of nickel and of iron," *Proceedings of the Royal Society of London*, no. 8, pp. 546–550, 1857.

[16] T. McGuire and R. Potter, "Anisotropic magnetoresistance in ferromagnetic 3d alloys," *IEEE Transactions on Magnetics*, vol. 11, no. 4, pp. 1018–1038, 1975.

[17] S. Tumanski and S. Baranowski, "Magnetic sensor array for investigations of magnetic field distribution," *J. Electr. Engin*, vol. 57, no. 8, pp. 185–188, 2006.

[18] M. Julliere, "Tunneling between ferromagnetic films," *Physics letters A*, vol. 54, no. 3, pp. 225–226, 1975.

[19] T. Miyazaki and N. Tezuka, "Giant magnetic tunneling effect in Fe/Al2O3/Fe junction," *Journal of magnetism and magnetic materials*, vol. 139, no. 3, pp. L231–L234, 1995.

[20] T. Scheike, Z. Wen, H. Sukegawa, and S. Mitani, "631% room temperature tunnel magnetoresistance with large oscillation effect in CoFe/MgO/CoFe (001) junctions," *Applied Physics Letters*, vol. 122, no. 11, 2023.

[21] S. Peng, Y. Zhang, M. Wang, Y. Zhang, and W. Zhao, "Magnetic tunnel junctions for spintronics: principles and applications," *Wiley Encyclopedia of Electrical and Electronics Engineering*, pp. 1–16, 1999.

[22] J.-G. J. Zhu and C. Park, “Magnetic tunnel junctions,” *Materials today*, vol. 9, no. 11, pp. 36–45, 2006.

[23] M. W. Keller, A. B. Kos, T. J. Silva, W. H. Rippard, and M. R. Pufall, “Time domain measurement of phase noise in a spin torque oscillator,” *Applied Physics Letters*, vol. 94, no. 19, p. 193105, 2009.

[24] X. Chao, M. Jamali, and J.-P. Wang, “Shape anisotropy effects on spin-torque oscillators,” *AIP Advances*, vol. 10, no. 4, p. 045101, 2020.

[25] K.-Z. Gao, X. Yin, Y. Yang, D. Ewing, P. J. De Rego, and S.-H. Liou, “MTJ based magnetic sensor for current measurement in grid,” *AIP Advances*, vol. 10, no. 1, p. 015301, 2020.

[26] H. Farkhani, M. Tohidi, S. Farkhani, J. K. Madsen, and F. Moradi, “An energy efficient neuromorphic computing system using real time sensing method,” in *2017 IEEE Biomedical Circuits and Systems Conference (BioCAS)*. IEEE, 2017, pp. 1–4.

[27] J. Hong, X. Li, N. Xu, H. Chen, S. Cabrini, S. Khizroev, J. Bokor, and L. You, “A Dual Magnetic Tunnel Junction-Based Neuromorphic Device,” *Advanced Intelligent Systems*, vol. 2, no. 12, p. 2000143, 2020.

[28] V. K. Joshi, P. Barla, S. Bhat, and B. K. Kaushik, “From MTJ device to hybrid CMOS/MTJ circuits: A review,” *IEEE Access*, vol. 8, pp. 194 105–194 146, 2020.

[29] S. Yuasa and D. Djayaprawira, “Giant tunnel magnetoresistance in magnetic tunnel junctions with a crystalline MgO (0 0 1) barrier,” *Journal of Physics D: Applied Physics*, vol. 40, no. 21, p. R337, 2007.

[30] P. Rzeszut, “Magnetic tunnel junctions with perpendicular anisotropy for use in serial and parallel connections of elementary STT-MRAM cells,” Master’s thesis, AGH University of Science and Technology, 2018.

[31] R. Meservey and P. Tedrow, “Spin-polarized electron tunneling,” *Physics reports*, vol. 238, no. 4, pp. 173–243, 1994.

[32] S. Ikeda, K. Miura, H. Yamamoto, K. Mizunuma, H. Gan, M. Endo, S. Kanai, J. Hayakawa, F. Matsukura, and H. Ohno, “A perpendicular-anisotropy CoFeB–MgO magnetic tunnel junction,” *Nature Materials*, vol. 9, no. 9, p. 721, 2010.

[33] Y. J. Kim, S. H. Kim, K. H. Kim, D. K. Kim, J. U. Cho, K.-H. Kim, and Y. K. Kim, “CoFeSiB–Pd multilayers and co-deposited alloy films exhibiting perpendicular magnetic anisotropies after heat treatment up to $500\,^{\circ}\mathrm{C}$,” *Acta Materialia*, vol. 125, pp. 196–201, 2017.

[34] J.-H. Park, C. Park, T. Jeong, M. T. Moneck, N. T. Nufer, and J.-G. Zhu, “Co/ Pt multilayer based magnetic tunnel junctions using perpendicular magnetic anisotropy,” *Journal of Applied Physics*, vol. 103, no. 7, p. 07A917, 2008.

[35] K. Watanabe, B. Jinnai, S. Fukami, H. Sato, and H. Ohno, “Shape anisotropy revisited in single-digit nanometer magnetic tunnel junctions,” *Nature communications*, vol. 9, no. 1, p. 663, 2018.

[36] S. Mangin, D. Ravelosona, J. Katine, M. Carey, B. Terris, and E. E. Fullerton, “Current-induced magnetization reversal in nanopillars with perpendicular anisotropy,” *Nature Materials*, vol. 5, no. 3, p. 210, 2006.

[37] K. Kobayashi, K. Hayakawa, J. Igarashi, W. A. Borders, S. Kanai, H. Ohno, and S. Fukami, “External-Field-Robust Stochastic Magnetic Tunnel Junctions Using a Free Layer with Synthetic Antiferromagnetic Coupling,” *Physical Review Applied*, vol. 18, no. 5, p. 054085, 2022.

[38] J. C. Slonczewski, “Current-driven excitation of magnetic multilayers,” *Journal of Magnetism and Magnetic Materials*, vol. 159, no. 1-2, pp. L1–L7, 1996.

[39] W. Skowroński, S. Łazarski, P. Rzeszut, S. Ziętek, J. Chęciński, and J. Wrona, “Influence of a composite free layer structure on thermal stability of perpendicular magnetic tunnel junction,” *Journal of Applied Physics*, vol. 124, no. 6, p. 063903, 2018.

[40] G. Prenat, K. Jabeur, G. Di Pendina, O. Boulle, and G. Gaudin, “Beyond STT-MRAM, spin orbit torque RAM SOT-MRAM for high speed and high reliability applications,” *Spintronics-based Computing*, pp. 145–157, 2015.

[41] F. Zahoor, T. Z. Azni Zulkifli, and F. A. Khanday, “Resistive random access memory (RRAM): an overview of materials, switching mechanism, performance, multilevel cell (MLC) storage, modeling, and applications,” *Nanoscale research letters*, vol. 15, no. 1, pp. 1–26, 2020.

[42] T. Eshita, T. Tamura, and Y. Arimoto, “Ferroelectric random access memory (FRAM) devices,” in *Advances in non-volatile memory and storage technology*. Elsevier, 2014, pp. 434–454.

[43] R. Zhao, L. Shi, W. Wang, H. Yang, H. Lee, K. Lim, E. Yeo, E. Chua, and T. Chong, “Study of phase change random access memory (PCRAM) at the nano-scale,” in *2007 Non-Volatile Memory Technology Symposium*. IEEE, 2007, pp. 36–39.

[44] M.-H. Nguyen and C.-F. Pai, “Spin–orbit torque characterization in a nutshell,” *APL Materials*, vol. 9, no. 3, p. 030902, 2021.

[45] D. C. Ralph and M. D. Stiles, "Spin transfer torques," *Journal of Magnetism and Magnetic Materials*, vol. 320, no. 7, pp. 1190–1216, 2008.

[46] T. L. Gilbert, "A phenomenological theory of damping in ferromagnetic materials," *IEEE transactions on magnetics*, vol. 40, no. 6, pp. 3443–3449, 2004.

[47] S. Ament, N. Rangarajan, A. Parthasarathy, and S. Rakheja, "Solving the stochastic Landau-Lifshitz-Gilbert-Slonczewski equation for monodomain nanomagnets: A survey and analysis of numerical techniques," *arXiv preprint arXiv:1607.04596*, 2016.

[48] J. Mojsiejuk, S. Ziętek, K. Grochot, W. Skowroński, and T. Stobiecki, "A comprehensive simulation package for analysis of multilayer spintronic devices," *arXiv preprint arXiv:2207.11606*, 2022.

[49] A. Slavin and V. Tiberkevich, "Nonlinear auto-oscillator theory of microwave generation by spin-polarized current," *IEEE Transactions on Magnetics*, vol. 45, no. 4, pp. 1875–1918, 2009.

[50] M. Tsoi, A. Jansen, J. Bass, W.-C. Chiang, M. Seck, V. Tsoi, and P. Wyder, "Excitation of a magnetic multilayer by an electric current," *Physical Review Letters*, vol. 80, no. 19, p. 4281, 1998.

[51] J. Chęciński, M. Frankowski, and T. Stobiecki, "Spin-torque oscillator read head in inhomogeneous magnetic fields," *IEEE Transactions on Magnetics*, vol. 53, no. 4, pp. 1–6, 2016.

[52] J. Torrejon, M. Riou, F. A. Araujo, S. Tsunegi, G. Khalsa, D. Querlioz, P. Bortolotti, V. Cros, K. Yakushiji, A. Fukushima *et al.*, "Neuromorphic computing with nanoscale spintronic oscillators," *Nature*, vol. 547, no. 7664, pp. 428–431, 2017.

[53] A. Tulapurkar, Y. Suzuki, A. Fukushima, H. Kubota, H. Maehara, K. Tsunekawa, D. Djayaprawira, N. Watanabe, and S. Yuasa, "Spin-torque diode effect in magnetic tunnel junctions," *Nature*, vol. 438, no. 7066, pp. 339–342, 2005.

[54] H. Kubota, A. Fukushima, K. Yakushiji, T. Nagahama, S. Yuasa, K. Ando, H. Maehara, Y. Nagamine, K. Tsunekawa, D. D. Djayaprawira *et al.*, "Quantitative measurement of voltage dependence of spin-transfer torque in MgO-based magnetic tunnel junctions," *Nature Physics*, vol. 4, no. 1, pp. 37–41, 2008.

[55] J. C. Sankey, Y.-T. Cui, J. Z. Sun, J. C. Slonczewski, R. A. Buhrman, and D. C. Ralph, "Measurement of the spin-transfer-torque vector in magnetic tunnel junctions," *Nature Physics*, vol. 4, no. 1, pp. 67–71, 2008.

[56] R. Sharma, R. Mishra, T. Ngo, Y.-X. Guo, S. Fukami, H. Sato, H. Ohno, and H. Yang, "Electrically connected spin-torque oscillators array for 2.4 GHz WiFi band transmission and energy harvesting," *Nature communications*, vol. 12, no. 1, p. 2924, 2021.

[57] N. Leroux, A. De Riz, D. Sanz-Hernández, D. Marković, A. Mizrahi, and J. Grollier, "Convolutional neural networks with radio-frequency spintronic nano-devices," *Neuromorphic Computing and Engineering*, vol. 2, no. 3, p. 034002, 2022.

[58] S. Bhatti, R. Sbiaa, A. Hirohata, H. Ohno, S. Fukami, and S. Piramanayagam, "Spintronics based random access memory: a review," *Materials Today*, vol. 20, no. 9, pp. 530–548, 2017.

[59] M. Mouchel, A. Bocheux, C. Ducruet, P. Sabon, I.-L. Prejbeanu, Y. Conraux, J. Alvarez-Hérault, K. Mackay, and C. Baraduc, "Noise study of magnetic field sensors based on magnetic tunnel junctions," in *Journal of Physics: Conference Series*, vol. 903, no. 1. IOP Publishing, 2017, p. 012008.

[60] Z. Jin, Y. Wang, K. Fujiwara, M. Oogane, and Y. Ando, "Detection of small magnetic fields using serial magnetic tunnel junctions with various geometrical characteristics," *Sensors*, vol. 20, no. 19, p. 5704, 2020.

[61] Z. Jin, T. M. Koo, M. S. Kim, M. Al-Mahdawi, M. Oogane, Y. Ando, and Y. K. Kim, "Highly-sensitive magnetic sensor for detecting magnetic nanoparticles based on magnetic tunnel junctions at a low static field," *AIP Advances*, vol. 11, no. 1, p. 015046, 2021.

[62] Z. Jin, M. A. I. Mohd Noor Sam, M. Oogane, and Y. Ando, "Serial MTJ-based TMR sensors in bridge configuration for detection of fractured steel bar in magnetic flux leakage testing," *Sensors*, vol. 21, no. 2, p. 668, 2021.

[63] Y.-c. Wu and J.-w. Feng, "Development and application of artificial neural network," *Wireless Personal Communications*, vol. 102, no. 2, pp. 1645–1656, 2018.

[64] M. Mishra and M. Srivastava, "A view of artificial neural network," in *2014 international conference on advances in engineering & technology research (ICAETR-2014)*. IEEE, 2014, pp. 1–3.

[65] B. Widrow, D. E. Rumelhart, and M. A. Lehr, "Neural networks: applications in industry, business and science," *Communications of the ACM*, vol. 37, no. 3, pp. 93–106, 1994.

[66] Y. T. Chae, R. Horesh, Y. Hwang, and Y. M. Lee, "Artificial neural network model for forecasting sub-hourly electricity usage in commercial buildings," *Energy and Buildings*, vol. 111, pp. 184–194, 2016.

[67] T. Emoto, U. R. Abeyratne, K. Kawano, T. Okada, O. Jinnouchi, and I. Kawata, "Detection of sleep breathing sound based on artificial neural network analysis," *Biomedical Signal Processing and Control*, vol. 41, pp. 81–89, 2018.

[68] O. I. Abiodun, A. Jantan, A. E. Omolara, K. V. Dada, A. M. Umar, O. U. Linus, H. Arshad, A. A. Kazaure, U. Gana, and M. U. Kiru, "Comprehensive review of artificial neural network applications to pattern recognition," *IEEE Access*, vol. 7, pp. 158 820–158 846, 2019.

[69] M. Chen, U. Challita, W. Saad, C. Yin, and M. Debbah, "Artificial neural networks-based machine learning for wireless networks: A tutorial," *IEEE Communications Surveys & Tutorials*, vol. 21, no. 4, pp. 3039–3071, 2019.

[70] S. Davidson and S. B. Furber, "Comparison of artificial and spiking neural networks on digital hardware," *Frontiers in Neuroscience*, vol. 15, p. 651141, 2021.

[71] J. Liu and D. Liang, "A survey of FPGA-based hardware implementation of ANNs," in *2005 International conference on neural networks and brain*, vol. 2. IEEE, 2005, pp. 915–918.

[72] M. Alçın, İ. Pehlivan, and İ. Koyuncu, "Hardware design and implementation of a novel ANN-based chaotic generator in FPGA," *Optik*, vol. 127, no. 13, pp. 5500–5505, 2016.

[73] M. M. Saady and M. H. Essai, "Hardware implementation of neural network-based engine model using FPGA," *Alexandria Engineering Journal*, vol. 61, no. 12, pp. 12 039–12 050, 2022.

[74] S. Li, K. Choi, and Y. Lee, "Artificial neural network implementation in FPGA: A case study," in *2016 International SoC Design Conference (ISOCC)*. IEEE, 2016, pp. 297–298.

[75] C. Yuan and S. S. Agaian, "A comprehensive review of Binary Neural Network," *arXiv preprint arXiv:2110.06804*, 2021.

[76] S. Ghosh-Dastidar and H. Adeli, "Spiking neural networks," *International journal of neural systems*, vol. 19, no. 04, pp. 295–308, 2009.

[77] R. Batllori, C. B. Laramee, W. Land, and J. D. Schaffer, "Evolving spiking neural networks for robot control," *Procedia Computer Science*, vol. 6, pp. 329–334, 2011.

[78] Z. Yan, J. Zhou, and W.-F. Wong, "Energy efficient ECG classification with spiking neural network," *Biomedical Signal Processing and Control*, vol. 63, p. 102170, 2021.

[79] H. Farkhani, T. Böhnert, M. Tarequzzaman, J. D. Costa, A. Jenkins, R. Ferreira, J. K. Madsen, and F. Moradi, "LAO-NCS: Laser assisted spin torque nano oscillator-based neuromorphic computing system," *Frontiers in neuroscience*, vol. 13, p. 1429, 2020.

[80] M. Romera, P. Talatchian, S. Tsunegi, K. Yakushiji, A. Fukushima, H. Kubota, S. Yuasa, V. Cros, P. Bortolotti, M. Ernoult *et al.*, "Binding events through the mutual synchronization of spintronic nano-neurons," *Nature Communications*, vol. 13, no. 1, p. 883, 2022.

[81] M. Zahedinejad, H. Fulara, R. Khymyn, A. Houshang, M. Dvornik, S. Fukami, S. Kanai, H. Ohno, and J. Åkerman, "Memristive control of mutual spin Hall nano-oscillator synchronization for neuromorphic computing," *Nature materials*, vol. 21, no. 1, pp. 81–87, 2022.

[82] D. J. Gauthier, E. Bollt, A. Griffith, and W. A. Barbosa, "Next generation reservoir computing," *Nature communications*, vol. 12, no. 1, p. 5564, 2021.

[83] S. Tsunegi, T. Taniguchi, K. Nakajima, S. Miwa, K. Yakushiji, A. Fukushima, S. Yuasa, and H. Kubota, "Physical reservoir computing based on spin torque oscillator with forced synchronization," *Applied Physics Letters*, vol. 114, no. 16, p. 164101, 2019.

[84] W. Skowroński, J. Chęciński, S. Ziętek, K. Yakushiji, and S. Yuasa, "Microwave magnetic field modulation of spin torque oscillator based on perpendicular magnetic tunnel junctions," *Scientific Reports*, vol. 9, no. 1, p. 19091, 2019.

[85] S. Tamaru, H. Kubota, K. Yakushiji, S. Yuasa, and A. Fukushima, "Extremely coherent microwave emission from spin torque oscillator stabilized by phase locked loop," *Scientific reports*, vol. 5, no. 1, pp. 1–6, 2015.

[86] M. Romera, P. Talatchian, S. Tsunegi, F. Abreu Araujo, V. Cros, P. Bortolotti, J. Trastoy, K. Yakushiji, A. Fukushima, H. Kubota *et al.*, "Vowel recognition with four coupled spin-torque nano-oscillators," *Nature*, vol. 563, no. 7730, pp. 230–234, 2018.

[87] M. Zahedinejad, A. A. Awad, S. Muralidhar, R. Khymyn, H. Fulara, H. Mazraati, M. Dvornik, and J. Åkerman, "Two-dimensional mutually synchronized spin Hall nano-oscillator arrays for neuromorphic computing," *Nature nanotechnology*, vol. 15, no. 1, pp. 47–52, 2020.

[88] M. Ociepka, "Oprogramowanie automatycznej trójosiowej stacji probierczej elementów spintronicznych," Engineer's thesis, AGH University of Science and Technology, 2018.

[89] W. Skowroński, K. Grochot, P. Rzeszut, S. Łazarski, G. Gajoch, C. Worek, J. Kanak, T. Stobiecki, J. Langer, B. Ocker *et al.*, "Angular harmonic Hall voltage and magnetoresistance measurements of Pt/FeCoB and Pt-Ti/FeCoB bilayers for spin Hall conductivity determination," *IEEE Transactions on Electron Devices*, vol. 68, no. 12, pp. 6379–6385, 2021.

[90] P. Rzeszut, W. Skowroński, S. Ziętek, P. Ogrodnik, and T. Stobiecki, “Biaxial Magnetic-Field Setup for Angular-Dependent Measurements of Magnetic Thin Films and Spintronic Nanodevices,” *IEEE Transactions on Magnetics*, vol. 54, no. 8, pp. 1–7, 2018.

[91] W. Skowroński, M. Czapkiewicz, S. Ziętek, J. Chęciński, M. Frankowski, P. Rzeszut, and J. Wrona, “Understanding stability diagram of perpendicular magnetic tunnel junctions,” *Scientific reports*, vol. 7, no. 1, p. 10172, 2017.

[92] A. Kozioł-Rachwał, W. Skowroński, M. Frankowski, J. Chęciński, S. Ziętek, P. Rzeszut, M. Ślęzak, K. Matlak, T. Ślęzak, T. Stobiecki *et al.*, “Interlayer exchange coupling, dipolar coupling and magnetoresistance in Fe/MgO/Fe trilayers with a subnanometer MgO barrier,” *Journal of Magnetism and Magnetic Materials*, vol. 424, pp. 189–193, 2017.

[93] P. Rzeszut, E. Jamro, and K. Wiatr, “Oscilloscope based on small-size FPGA with VGA display,” *Measurement Automation Monitoring*, vol. 64, 2018.

[94] P. Rzeszut, W. Skowroński, S. Ziętek, and T. Stobiecki, “Method of producing active multi-level memory structure and the multi-level memory structure,” *Pat.235585*, 2020.

[95] S. Ziętek, P. Rzeszut, W. Skowroński, S. Ziętek, T. Stobiecki, and J. Budzioch, “Electromagnet unit for generation of magnetic field,” *Pat.229635*, 2018.

[96] P. Rzeszut, W. Skowroński, S. Ziętek, J. Chęciński, J. Wrona, and T. Stobiecki, “Serially connected perpendicular magnetic tunnel junctions for multi-bit STT-MRAM storage cells and neuromorphic computing,” *QUTECNOMM 2019: The Fifth Poznań Synposium on Quantum Technologies, Nonlinear Optics, Magnonics and Metamaterials; Poznań, Poland*, 2019.

[97] P. Rzeszut, W. Skowroński, S. Ziętek, J. Chęciński, J. Wrona, and T. Stobiecki, “Simulation of multi-bit MRAM storage cells utilizing serially connected perpendicular magnetic tunnel junctions,” *SPICE: Antiferromagnetic Spintronics: from topology to neuromorphic computing; Mainz, Germany*, 2019.

[98] P. Rzeszut, W. Skowroński, S. Ziętek, J. Wrona, and T. Stobiecki, “Simulation of multi-bit MRAM storage cells utilizing serially connected perpendicular magnetic tunnel junctions,” *64th International Electron Devices Meeting; San Francisco, USA*, 2018.

[99] P. Rzeszut, W. Skowroński, S. Ziętek, and T. Stobiecki, “Simulation of multi-bit MRAM storage cells utilizing serially connected perpendicular magnetic tunnel junctions,” *8th National Conference on Nanotechnology; Łódź, Poland*, 2017.

[100] P. Rzeszut, E. Jamro, and K. Wiatr, "Oscilloscope based on small-size FPGA with VGA display," *The 21st Conference on Reconfigurable Ubiquitous Computing, Szczecin, Poland*, 2018.

Author's Achievements

Journal papers focused directly on the dissertation's subject:

– P. Rzeszut, W. Skowroński, S. Ziętek, J. Wrona, and T. Stobiecki, "Multi-bit MRAM storage cells utilizing serially connected perpendicular magnetic tunnel junctions," *Journal of Applied Physics*, vol. 125, no. 22, p. 223907, 2019
– P. Rzeszut, J. Chęciński, I. Brzozowski, S. Ziętek, W. Skowroński, and T. Stobiecki, "Multi-state MRAM cells for hardware neuromorphic computing," *Scientific Reports*, vol. 12, no. 1, pp. 1–11, 2022
– P. Rzeszut, J. Mojsiejuk, W. Skowroński, S. Tsunegi, H. Kubota, and S. Yuasa, "Towards mutual synchronization of serially connected Spin Torque Oscillators based on magnetic tunnel junctions," *arXiv preprint arXiv:2306.11608*, 2023
– W. Skowroński, K. Grochot, P. Rzeszut, S. Łazarski, G. Gajoch, C. Worek, J. Kanak, T. Stobiecki, J. Langer, B. Ocker *et al.*, "Angular harmonic Hall voltage and magnetoresistance measurements of Pt/FeCoB and Pt-Ti/FeCoB bilayers for spin Hall conductivity determination," *IEEE Transactions on Electron Devices*, vol. 68, no. 12, pp. 6379–6385, 2021
– P. Rzeszut, W. Skowroński, S. Ziętek, P. Ogrodnik, and T. Stobiecki, "Biaxial Magnetic-Field Setup for Angular-Dependent Measurements of Magnetic Thin Films and Spintronic Nanodevices," *IEEE Transactions on Magnetics*, vol. 54, no. 8, pp. 1–7, 2018
– W. Skowroński, S. Łazarski, P. Rzeszut, S. Ziętek, J. Chęciński, and J. Wrona, "Influence of a composite free layer structure on thermal stability of perpendicular magnetic tunnel junction," *Journal of Applied Physics*, vol. 124, no. 6, p. 063903, 2018
– W. Skowroński, M. Czapkiewicz, S. Ziętek, J. Chęciński, M. Frankowski, P. Rzeszut, and J. Wrona, "Understanding stability diagram of perpendicular magnetic tunnel junctions," *Scientific reports*, vol. 7, no. 1, p. 10172, 2017
– A. Kozioł-Rachwał, W. Skowroński, M. Frankowski, J. Chęciński, S. Ziętek, P. Rzeszut, M. Ślęzak, K. Matlak, T. Ślęzak, T. Stobiecki *et al.*, "Interlayer exchange coupling, dipolar coupling and magnetoresistance in Fe/MgO/Fe trilayers with a subnanometer MgO barrier," *Journal of Magnetism and Magnetic Materials*, vol. 424, pp. 189–193, 2017

Journal papers not related to the dissertation's subject:

- P. Rzeszut, E. Jamro, and K. Wiatr, "Oscilloscope based on small-size FPGA with VGA display," *Measurement Automation Monitoring*, vol. 64, 2018

Patents:

- P. Rzeszut, W. Skowroński, S. Ziętek, and T. Stobiecki, "Method of producing active multi-level memory structure and the multi-level memory structure," *Pat.235585*, 2020
- S. Ziętek, P. Rzeszut, W. Skowroński, S. Ziętek, T. Stobiecki, and J. Budzioch, "Electromagnet unit for generation of magnetic field," *Pat.229635*, 2018

Conference communicates focused directly on the dissertation's subject:

- P. Rzeszut, W. Skowroński, S. Ziętek, J. Chęciński, J. Wrona, and T. Stobiecki, "Serially connected perpendicular magnetic tunnel junctions for multi-bit STT-MRAM storage cells and neuromorphic computing," *QUTECNOMM 2019: The Fifth Poznań Synposium on Quantum Technologies, Nonlinear Optics, Magnonics and Metamaterials; Poznań, Poland*, 2019
- P. Rzeszut, W. Skowroński, S. Ziętek, J. Chęciński, J. Wrona, and T. Stobiecki, "Simulation of multi-bit MRAM storage cells utilizing serially connected perpendicular magnetic tunnel junctions," *SPICE: Antiferromagnetic Spintronics: from topology to neuromorphic computing; Mainz, Germany*, 2019
- P. Rzeszut, W. Skowroński, S. Ziętek, J. Wrona, and T. Stobiecki, "Simulation of multi-bit MRAM storage cells utilizing serially connected perpendicular magnetic tunnel junctions," *64th International Electron Devices Meeting; San Francisco, USA*, 2018
- P. Rzeszut, W. Skowroński, S. Ziętek, and T. Stobiecki, "Simulation of multi-bit MRAM storage cells utilizing serially connected perpendicular magnetic tunnel junctions," *8th National Conference on Nanotechnology; Łódź, Poland*, 2017

Conference communicates not related to the dissertation's subject:

- P. Rzeszut, E. Jamro, and K. Wiatr, "Oscilloscope based on small-size FPGA with VGA display," *The 21st Conference on Reconfigurable Ubiquitous Computing, Szczecin, Poland*, 2018

Leadership of research projects:

- Magnetic tunnel junctions with perpendicular anisotropy for use in serial/paralel connections of elementary STT-MRAM cells (Diamond Grant 0048/DIA/2017/46)

Participation in research projects:

- Nanoscale spin torque devices for spin electronics NANOSPIN (PSPB-045/2010)
- Microwave spin electronics nano devices MICROSPIN (LIDER/467/L-6/14/NCBR/2015)

Research visits, internships, training courses:

- 4th - 28th September 2022, National Institute of Advanced Industrial Science and Technology (AIST), Tsukuba, JAPAN - technological training and measurements of interconnected magnetic tunnel junctions
- 17th - 28th September 2018, AGH, Kraków, POLAND - The European School on Magnetism ESM-2018
- 30th June - 5th July 2015, SPINTEC, Grenoble, FRANCE - InMRAM 2015 school on magnetic random access memories and spintronic devices

Prizes and Awards:

- Featured paper: Multi-bit MRAM storage cells utilizing serially connected perpendicular magnetic tunnel junctions [1] in 2019
- Top 100 in Engineering - 2022: Multi-state MRAM cells for hardware neuromorphic computing [2] in 2022
- Scholarship of Polish Ministry of Science and Higher Education in 2016 and 2017
- The best student of AGH University of Science and Technology ("AS AGH") in 2018
- 1st place - the best application master thesis ("Diamenty AGH") in 2019
- 1st place - the best engineering thesis ("Inżynier roku 2017") in 2017